Experimental studies of a low emittance electron beam in the KEK-ATF damping ring with a laserwire beam profile monitor

by

Yosuke HONDA

A Dissertation
Department of Physics, Faculty of Science,
Kyoto University

July 28, 2004

Abstract

Production of a low-emittance beam is one of the key technologies in realizing the future linear colliders. The Accelerator Test Facility at KEK has been built to establish technologies to generate the required low-emittance beam, and to experimentally study the effects which might limit emittance reduction.

A beam monitor called the laserwire beam profile monitor was developed to measure the emittance of a stored beam in the ATF damping ring. This monitor has been upgraded to enable faster measurements of both transverse beam sizes with a better spatial resolution. The signal detection scheme was also modified to separately measure the beam profiles of each bunch in a multi-bunch beam.

Continuous efforts have been made to reduce emittances further, and intensive studies have been done with the upgraded laserwire monitor. Four-dimensional beam sizes and their intensity dependence were measured in various bunch volume conditions. In particular, it was found that the vertical emittance of a single-bunch mode was reduced to 4 pm·rad in the zero current limit, the smallest emittance ever achieved in the world, and it grow by about factor of 1.5 at the intensity of 10^{10} electrons per bunch. The overall nature of two transverse emittances, bunch length, and momentum spread seemed to have no serious disagreement with the expectation of the model calculation involving the intra-beam scattering.

The emittance was also measured in the multi-bunch operational mode. It was found that the generation of a similar small emittance was possible to those realized in a single-bunch mode. No large bunch-to-bunch difference was seen in the beam intensity studied so far. All the results above, obtained with the laserwire monitor, have proved to be an important milestone for realizing future linear colliders.

Acknowledgments

This thesis could not have been written without the help and support of many people. Firstly, I would like to express my gratitude to my supervisor Prof. N. Sasao of Kyoto University and Prof. J. Urakawa of High Energy Accelerator Research Organization (KEK).

I am particularly grateful to the members of the laserwire development group: Prof. Y. Higashi, T. Taniguchi, T. Okugi, S. Araki, M. Takano, M. Nomura, K. Hirano, Y. Yamazaki, H. Sakai and K. Takezawa, for their generous help and suggestions through all the work.

I would like to express my gratitude to all the members of KEK-ATF: Prof. H. Hayano, K. Kubo, N. Terunuma, S. Kuroda, M. Kuriki, T. Naito, Prof. N. Toge, Prof. S. Kamada, Prof. Higo, Prof. T. Suzuki, Prof. K. Nakajima, Prof. T. Tauchi, T. Omori, Y. Kurihara, N. Kudo, T. Saeki, V. Vogel, N. Delerue, H. Sasaki, people from E-cube co. and Kanto-Joho co.. Witout their hard work to develop and operate the ATF, this study never be accomplished.

I would like to acknowledge to all the students worked together at ATF: K. Dobashi, T. Imai, I. Sakai, T. Muto, M. Fukuda, R. Kuroda, P. Karataev, A. Higurashi, K. Hasegawa, A. Aoki, T. Oshima, T. Iimura, K. Iida, T. Hirose, Y. Inoue, A. Ohashi, I. Yamazaki, M. Matsuda, K. Watanabe, T. Suehara, H. Fujimoto and others.

I am grateful to collabolators from other facilities: M. Ross, J. Frisch, D. McCormick, M. Woodley, J. Nelson, J. Turner, T. Raubenheimer, A. Wolski, F. Zimmermann, G. Blair, T. Kamps and others. Fruitful discussions with them helped us a lot.

Last but not least, I would like thank to the members of High Energy Physics group of Kyoto university: Prof. K. Nishikawa, Prof. H. Sakamoto, Prof. T. Nakaya, R. Kikuchi, T. Nomura, M. Yokoyama, M. Suehiro, Y. Takeuchi, K. Murakami, Y. Ushiroda, T. Inagaki, T. Fujiwara, T. Nakamura, N. Nakamura, T. Shima, S. Nishida, H. Yokoyama, H. Yumura, S. Mukai, I. Kato, A. Shima, E. Shinya, H. Maesaka, K. Mizouchi, K. Uchida, M. Hasegawa, S. Yamamoto, T. Sumida, S. Tsuji, T. Sasaki, H. Morii, S. Ueda, K. Hayashi, T. Morita, J. Kubota, T. Shirai, N. Taniguchi, K. Hiraide, and others. I am thankful to the secretary of our group T. Ishino and A. Nakao and the secretariat members of the physics department, K. Nakagawa, A. Saito and A. Nishino. I have been staying in KEK, but always been supported by all of them.

Kyoto, Japan
August 15, 2004.
Yosuke HONDA

Contents

List of Figures

List of Tables

Chapter 1

Introduction

1.1 Linear Colliders

Quests for the fundamental constituents of matter and the law which governs everything in the universe, have always been a frontier of human activities. In elementary particle physics, accelerators have played an important role in pioneering this profound field of knowledge. Experiments with accelerated particle beams have discovered hundreds of new particles and revealed the underlying principles of the dynamics.

The energy frontier has been explored by two types of high energy colliding beams: hadron (proton and anti-proton) and lepton (electron and positron) beam. The former has an advantage in discovering a signal of new particles and/or new phenomena. This is due to the versatile nature of the beam. On the other hand, thanks to its well-known and clean nature, the latter plays a crucial role in establishing the precision properties. Up to now, colliding beams have always employed a circular acceleration scheme because of its efficiency. Among the electron-positron (e^+e^-) colliders, LEP-II, the largest circular machine, has reached the highest center-of-mass (CM) energy of ∼200 GeV. This energy in generally considered to be the limit of the e^+e^- circular machine due to its huge energy loss by synchrotron radiations.

Future e^+e^- linear colliders are aiming to open up the energy region of TeV scale employing a different scheme of acceleration. A number of linear collider projects have been proposed in the world, such as TESLA [1], NLC [2], GLC [3] and CLIC [4]. Figure 1.1 shows the conceptual design of GLC. Electron and positron beams are accelerated up to ∼500 GeV all the way through long linear accelerators, and then collisions are realized in single crossing of two beams. Some important parameters of GLC are summarized in Table 1.1.

There are two crucial technologies in realizing TeV-scale linear colliders: development of a high-gradient accelerator and production of a low emittance beam. The former is essential to reach a needed energy within a realistic length while the latter is crucial to realize a luminosity required for physics.

As for the gradient issue, an effective acceleration gradient of more than 50 MV/m is required, a challenging value compared to about 25 MV/m in existing linacs. Various technologies and/or components have to be developed; for instance, a high-efficiency RF power source, and an accelerating structure which can produce a high gradient accelerating field and free from non-desired transverse kick.

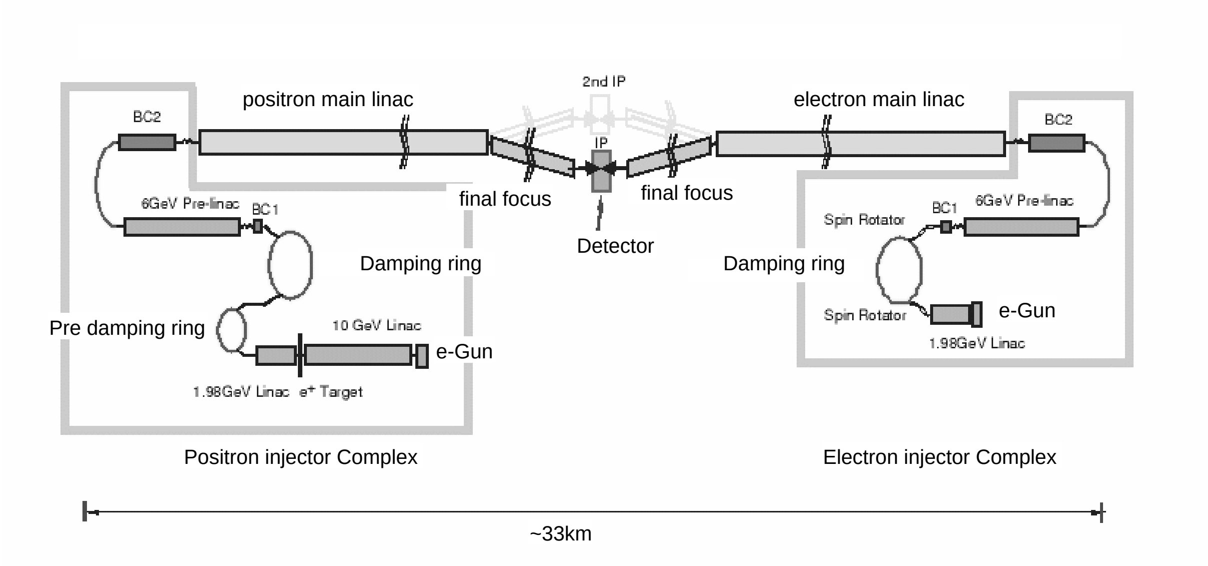

Figure 1.1: Schematic layout of GLC. Other proposed linear colliders employ different technologies for main linacs; their parameters and details are different, but the overall design philosophy are mostly the same.

The luminosity ($\mathcal{L}$) of the collision is also critical. In general, cross sections for interesting physics processes decrease in proportion to the inverse square of the CM energy ($\sigma \sim 1/E_{CM}^2$.) (see Figure 1.2). Hence, the energy frontier machine is necessarily a luminosity frontier machine. For example, $\mathcal{L} \sim 2.5 \times 10^{34}$ cm^{-2}s^{-1} is aimed at $E_{cm} = 1$ TeV in the GLC project.

In this thesis, we will focus on the production of a high intensity, low emittance beam, which is a key technology to the high luminosity linear colliders.

1.2 Low emittance beams and the ATF

The luminosity can be written down as

$$\mathcal{L} = \frac{f_{rep} n_b N_{e^-} N_{e^+}}{4\pi \sigma_x^* \sigma_y^*} \quad , \tag{1.1}$$

where f_{rep} is the repetition rate of a beam-pulse, n_b the number of bunches contained in the pulse, N_{e^-} and N_{e^+} the bunch population, and σ_x^* and σ_y^* the beam sizes at the interaction point. For maximizing the luminosity, Eq. 1.1 tells us to deliver as many particles as possible to the interaction point and to reduce as small as possible the beam spot size.

The beam sizes σ_x^* and σ_y^* are basically given by

$$\sigma_x^* = \sqrt{\beta_x^* \epsilon_x} \quad \text{and} \quad \sigma_y^* = \sqrt{\beta_y^* \epsilon_y} \quad , \tag{1.2}$$

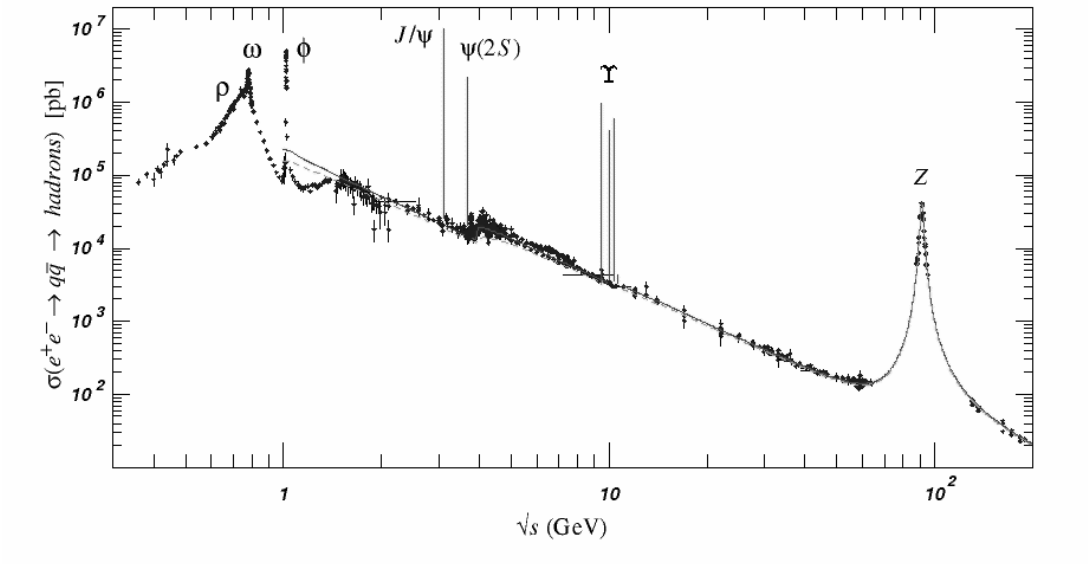

Figure 1.2: Hadronic annihilation cross section in e$^+$e$^-$ collisions. The cross section decreases with the collision energy. High energy machines are required to realize high luminosity.

Table 1.1: Design parameters of GLC.

Item	Symbol	Value		Unit
		Stage I	Stage II	
Center-of-mass energy	E_{CM}	500	1000	GeV
Linac repetition rate	f_{rep}	150	100	Hz
Number of particles / bunch	N	0.75		$\times 10^{10}$
Number of bunches / pulse	n_b	192		
Bunch separation	t_b	1.4		ns
Effective gradient	E_{eff}	44.1		MV/m
Linac length / beam		7.25	14.11	km
Beam delivery length / beam		1.9		km
Total site AC power		233	300	MW
Normalized emittance at DR exit	$\gamma\epsilon_x/\gamma\epsilon_y$	3.0 / 0.02		$\times 10^{-6}$ m·rad
Normalized emittance at IP	$\gamma\epsilon_x^*/\gamma\epsilon_y^*$	3.6 / 0.04		$\times 10^{-6}$ m·rad
Beta function at IP	β_x^*/β_y^*	8 / 0.11	13 / 0.11	mm
Beam size at IP	σ_x^*/σ_y^*	243 / 3.0	219 / 2.1	nm
Full crossing angle	θ_c	7		mrad
Nominal luminosity	$\mathcal{L}_0$	17.7	18.5	$\times 10^{33}$ cm^{-2}s^{-1}
Peak luminosity	$\mathcal{L}$	25.0	25.0	$\times 10^{33}$ cm^{-2}s^{-1}

where $\beta^*_{x(y)}$ is the value of a horizontal (vertical) β function at the interaction point and $\epsilon_{x(y)}$ is the horizontal (vertical) emittance. In general, β function can be controlled by focusing elements. A strong quadrupole doublet will be used in the GLC final focus system to obtain small β. We note that a precise chromaticity compensation scheme has to be included in the final focus system [5]. This is because the spot size may be diluted at the collision point due to the chromaticity arising from the strong focusing. Emittance is a measure which represents the distribution of the particle's transverse motion. Smaller emittance means a more compact distribution in the phase space.

Apparently, production and handling of a low emittance beam is the key technology to achieve the required luminosity. In any linear collider project, production of a low emittance beam is realized in a special ring, called usually a damping ring. In these rings, beam's transverse motions are converted to longitudinal motions by a combination of energy loss via synchrotron radiations and energy gain in an RF acceleration cavity (See Appendix A in detail.). This cooling process in the transverse plane will compete with a heating process due to a combination of quantum fluctuation of particle's energy and a dispersion function. Thus an equilibrium emittance is basically determined by ring's optical functions. Damping rings employ optical functions specially designed to achieve small emittances. We note that since there is no bending magnet in a vertical plane (the dispersion function is zero around the ring), an equilibrium emittance is very small, usually determined by unavoidable x-y coupling due to magnet misalignments and/or field errors. We also note that the discussion above is true only in the zero current limit; if the bunch population is large, then collective effects such as an intra-beam scattering should be taken into account. The collective effects are the topics we like to study in this thesis.

Figure 1.3 shows normalized emittances of two transverse directions for proposed linear colliders (at the exit of the damping ring) and for some existing accelerators and storage rings. Here, the normalized emittance means $\gamma\epsilon$, the product of the emittance and particle's γ-factor, and is a conserved quantity during acceleration. The emittance required in future linear colliders has not yet been realized in any accelerators in the world.

The Accelerator Test Facility (ATF) in KEK is an accelerator complex to study dynamics and techniques in generating a low-emittance beam required for linear colliders. The damping ring is designed to produce a beam with similar qualities as required in GLC/NLC. The items to be studied at the ATF damping ring are listed below:

- Establish techniques for precision magnet alignment and/or beam tuning method to stably produce ultra-low-emittance beams:

  Especially, the vertical emittance requires a severe magnet alignment tolerance and a precise beam tuning. The most unambiguous way to prove this issue is to actually produce and measure the beam with specified qualities.

- Experimental studies of the collective effects (intra-beam scattering, wake field, etc.):

  Due to the small emittance, electrons in a bunch are localized in a small volume. A complex effect of many particles in a bunch, such as intra-beam scattering, may

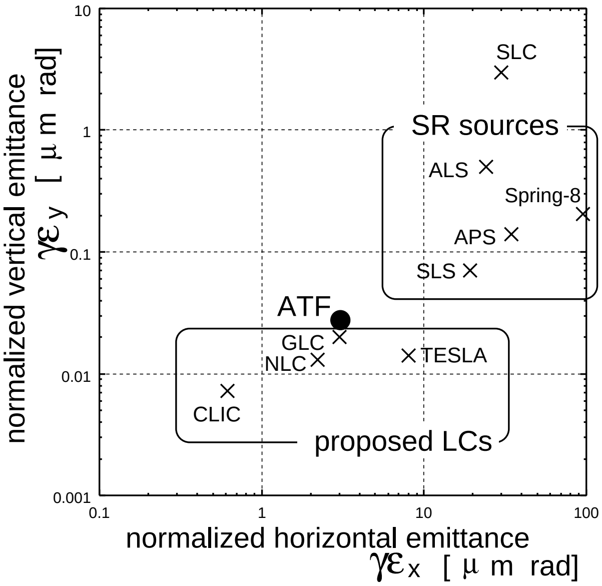

Figure 1.3: Normalized emittance of two transverse directions for various rings [6]. The damping ring of Stanford Linear Collider (SLC) worked well to realize μm spot size. Third-generation synchrotron light sources are now in operation producing small emittance beams to increase the brightness of the synchrotron light. The required values for linear colliders are much smaller than those of SLC and SR facilities. The target values of the ATF damping ring are similar to those of GLC/NLC.

dilute the beam qualities at a high intensity. Because of the multi-body aspect of the phenomena, a theoretical calculation is not reliable enough, and an experimental study is important.

A wake field induced by a beam itself may cause instabilities. Although the geometry of the beam chamber is carefully designed to reduce the effect, its performance can only be confirmed with an experiment with a high intensity beam.

- Experimental studies of the multi-bunch instabilities (coupled-bunch oscillation, ion effects, etc.):

  When the ring is operated with a multi-bunch beam, the existence of the preceding bunches may affect the bunch motion. For example, a wake field or ions may induce the coupling of the motions between bunches. Experimental confirmation of the non-existence of bunch dependence or at least quantitative understanding of the mechanism is important.

- Development of various diagnostic instruments:

  Since linear collider is a new type of machine and the beam properties are different from those of existing machines, a number of new monitors are required. Since ATF is the only place to supply the similar beam as in future linear colliders, many instruments should be developed in ATF.

1.3 Laser-based beam diagnostics

There is an increasing demand for laser-based beam diagnostics. The laser-target does not destruct the beam during the measurement (non-invasive method), and conversely it would not be destroyed by the beam.

The most conventional device to measure the transverse beam profile is a wire scanner. A solid wire of metal (tungsten or carbon) intersects the electron beam and the beam profile is obtained by counting an appropriate background rate as a function of the relative position of the wire and beam. This technique, however, cannot be used at any linear colliders; the electron beam is so intense that solid wires would be quickly damaged. It must be replaced by a laser-based technique.

In the linear colliders (and in their development work), laser-based beam profile monitors will play an important role. These monitors utilize the Compton scattering process of electrons with laser light. Many variations of the laser-based monitors have been developed. We mention two notable examples below.

The first is the so called laser-wire monitor. A focused laser beam is used as a wire to scan the electron beam. The first laser-wire monitor was developed at SLAC to measure the beam size at the interaction point of SLC (it was placed inside the detector) [7]. A high power pulsed UV laser was focused by a refractive optics. It successfully measured 1 μm beam size with a laser beam focused down to $\sim$0.5 μm. A similar laser-wire system, to be placed in the beam delivery system of future linear colliders, is proposed and is being developed ([8]). A laserwire to measure the beam size in the damping ring was developed in KEK-ATF. It played a crucial role in this work, and it will be detailed in Chapter 3.

The other example is the one which utilizes an interference pattern produced by two laser beams. It was first successfully tested at SLAC in order to estimate a nano-meter beam size at the FFTB [9]; the beam was scanned by the fine interference pattern.

In this thesis, studies of an ultra-low emittance electron beam in the damping ring of KEK-ATF are presented. The beam emittances were measured by using the laserwire beam profile monitor. An overview of the Accelerator Test Facility (ATF) is given in Chapter 2. In Chapter 3, we describe the laserwire beam profile monitor, the most important instrument for this work. Chapter 4 and 5 are the results of the experiment done with a single-bunch and a multi-bunch beam, respectively. Chapter 6 is devoted to the conclusion of this work.

A brief description of the beam dynamics in a storage ring is given in Appendix A. In Appendix B, a new laserwire measurement method which enables to measure electron beams smaller than laser width is described. We append the latest result of high intensity multi-bunch measurement in Appendix C.

Chapter 2

The KEK Accelerator Test Facility

The KEK Accelerator Test Facility (ATF) [10] has been built as one of the steps toward realization of future linear colliders; its main purpose is to establish production and manipulation techniques of a low emittance beam. In this chapter, we give a brief review of the ATF itself, various monitors used for beam diagnostics, and beam tuning methods to produce an extremely small emittance beam.

2.1 Overview of the accelerator complex

The layout of the facility is shown in Figure 2.1. It consists of three major parts: an injector linac, a damping ring, and an extraction line. Below, we give a brief overview of the beam line from upstream to downstream.

2.1.1 Electron-gun system

A photo-cathode RF-gun system has been used as a source of a low-emittance electron beam [1]. A schematic figure of the RF-gun is shown in Figure 2.2. A 1.6-cell S-band RF cavity is excited in the π-mode resonance. A photo-cathode is made of a thin film of Cs-Te alloy formed on the surface of a molybdenum plug. It is attached to the end plate of the half-cell, where an electric field of about 100 MV/m is generated. A pulse of ultra-violet laser light is injected on the photo-cathode to generate a bunch of electrons via photo-electric emissions. A typical quantum efficiency of the cathode is 1%, and it lasts more than one month in operation. An electron bunch is immediately accelerated by the electric field in the cavity, and is further accelerated up to 80 MeV in a pre-injector.

The layout of the laser system is displayed in Figure 2.3. An infra red (λ=1064 nm) mode-locked laser of 357 MHz (2.8 nsec spacing) is used as a seed laser beam. The required laser pulse is structured (single-bunch or 20-bunch) in the first stage, and amplified in a four-stage Nd:YAG amplifier pumped by flush-lamps. Then it is converted into ultra violet (λ=266 nm) light and is transported to the RF-gun.

---

[1] Until 2001, the ATF had operated with a thermionic gun, a conventional electron-gun which utilized the thermionic emission of electrons. It was replaced by the RF-gun to improve the beam qualities at the injector.

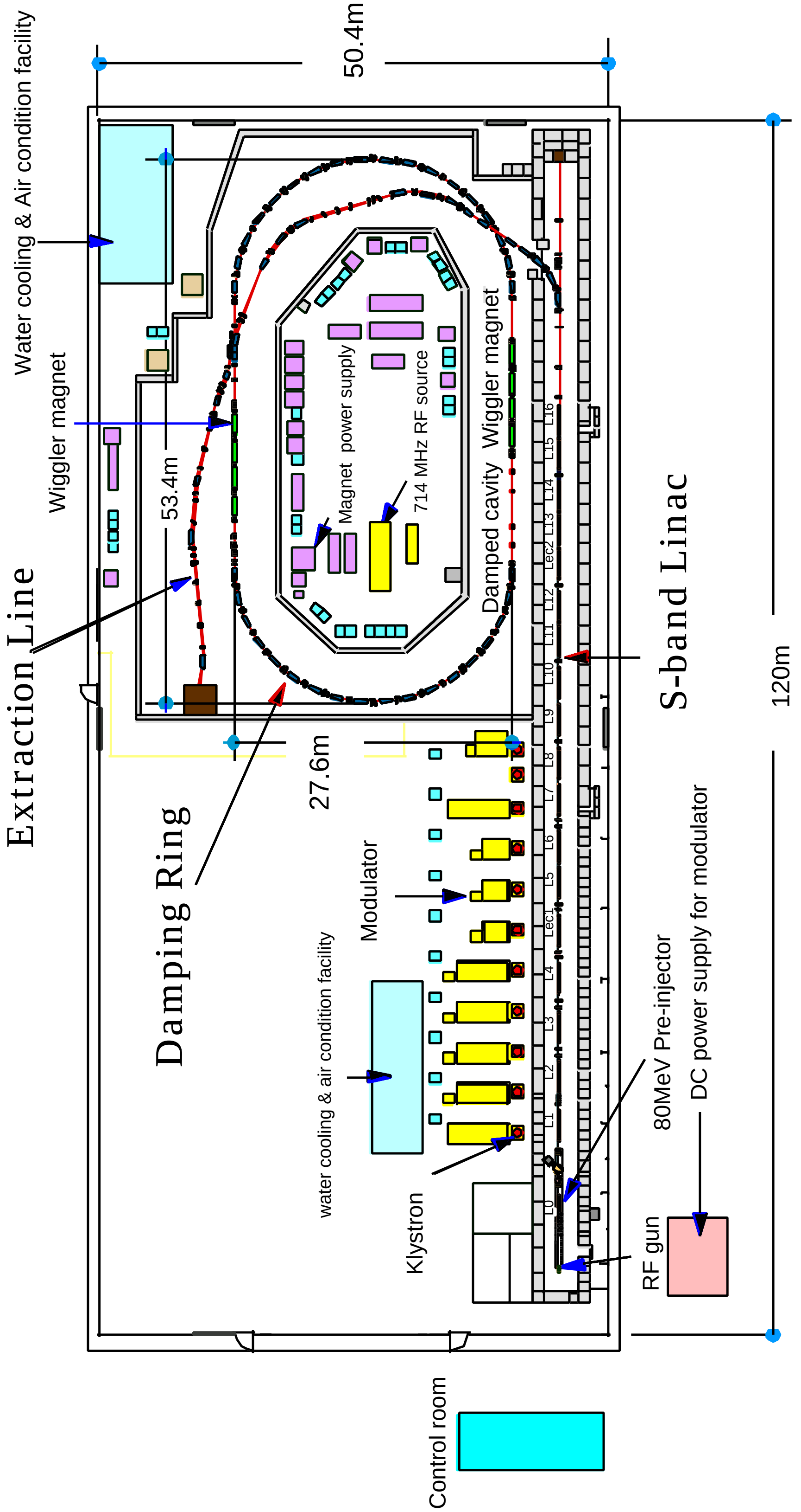

Figure 2.1: Layout of the Accelerator Test Facility.

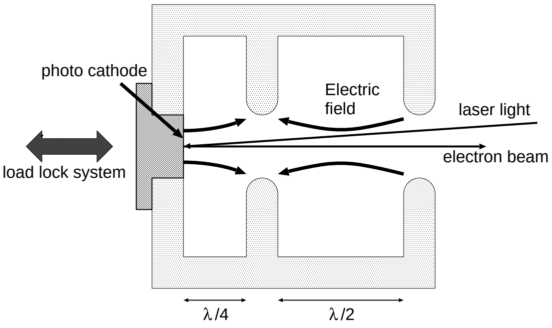

Figure 2.2: Schematic figure of a photo-cathode RF-gun. It consists of a 1.6 cell S-band RF-cavity and a Cs-Te photo-cathode. A laser pulse is injected on the cathode to emit electrons. The electron bunch is immediately accelerated by the electric field in the cavity.

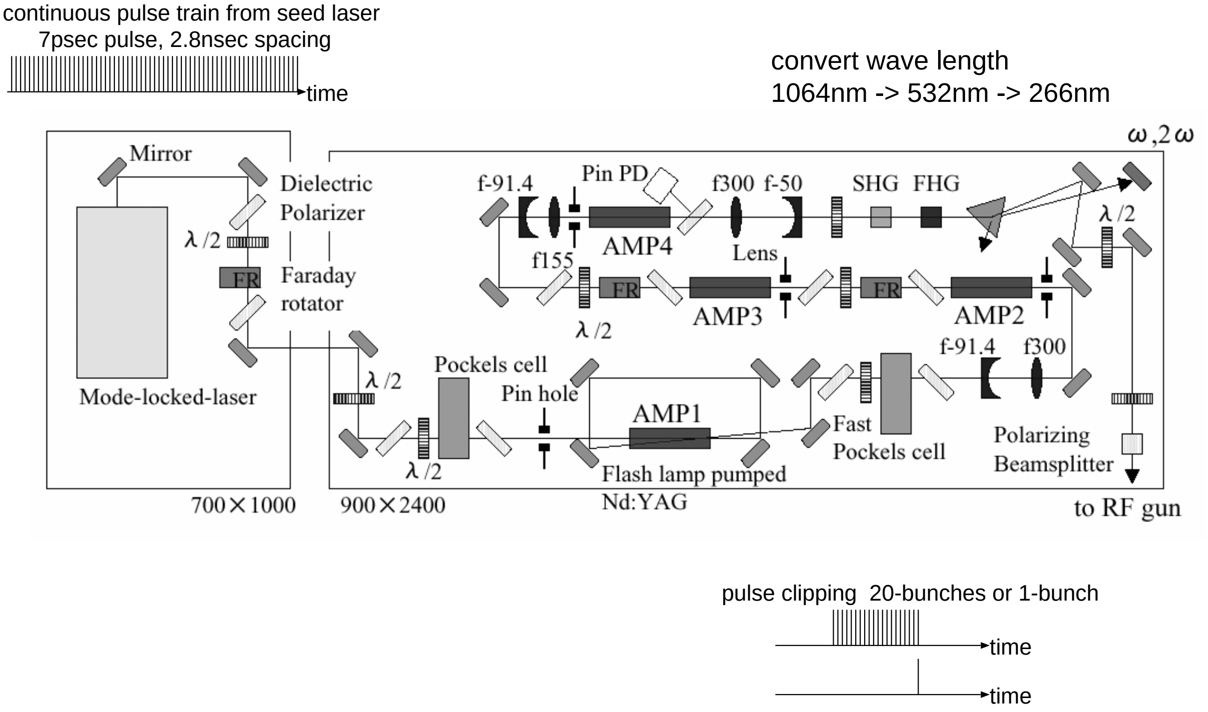

Figure 2.3: Laser system for the RF-gun. A continuous pulse train of laser beam is generated from a mode-lock laser (A passive mode-lock method utilizing SESAM [11] is employed to realize a short pulse width (7psec)). The pulse structure (20-bunch / 1-bunch) is clipped by a pockels-cell system. After amplified, the infra red light is converted to an ultra violet light; the wave length enough to exceed the work function of the photo-emission.

2.1.2 Linac

The electron beam is accelerated to 1.28 GeV by an S-band (2856 MHz) linac, and is injected into the damping ring. There are 8 units of RF system for regular acceleration, and two special units for energy compensation.

The regular RF unit is illustrated in Figure 2.4. Klystrons are used to produce an RF pulse of 80MW peak power. First, it is compressed by a SLED system to obtain higher peak power, and then it is divided into two. Finally, each pulse drives 3-m accelerator tubes. An accelerating field of 30 MV/m is obtained in each accelerator tube.

When a multi-bunch beam is accelerated, an energy gain of a bunch may be reduced due to an existence of the preceding bunch in the same train. This effect, called the beam loading effect, is especially pronounced when the intensity is high. To reduce overall energy spread, a system called the energy compensation system is being introduced. It is an accelerator structure with slightly shifted frequency (±5MHz) from the regular structures. Figure 2.5 explains the scheme of the energy compensation system. When a multi-bunch beam train goes through this compensation system, each bunch rides on a different phase of the accelerating field. It corrects the energy gain of each bunch, and compresses the overall energy spread within an energy aperture of the damping ring.

The electron beam, accelerated to 1.28 GeV, is transported through the beam transport line, and is injected to the damping ring by a pulsed kicker magnet.

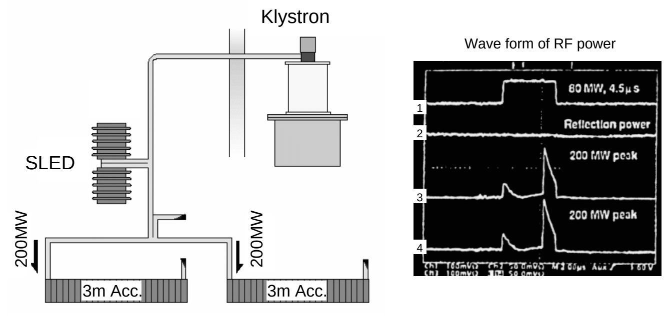

Figure 2.4: Regular RF unit. It consists of a klystron, SLED and two accelerator tubes. The klystron produces a 4.5 μs wide RF pulse of 80 MW peak power (ch1 in the right picture). The SLED cavity enhances the peak power by compressing in time, and drives two accelerator tubes (ch3,4 in the right picture).

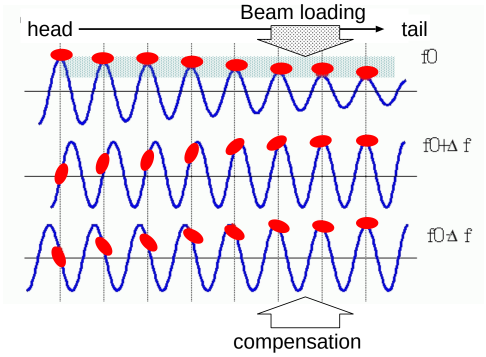

Figure 2.5: Principle of the energy compensation system. Successive bunches on a train ride on different phases of the $f_0 \pm \Delta f$ accelerating cavity. It corrects the energy gain of each bunch, and alleviates the beam loading effect.

2.1.3 Damping ring

The damping ring is a storage ring with a race-track shape; it has two arc sections and two straight sections. Each arc is 41.7 m in circumference and each straight section is 27.6 m in length; the total circumference is 138.6 m. The beam injection/extraction system, an RF cavity and wiggler magnets are installed in the straight sections (the wigglers were being turned off in this experiment). There are 96 beam position monitors (BPM) to measure the beam orbit, and 48 horizontal and 50 vertical steering magnets for orbit correction. The optical functions, β and η, of the entire damping ring are plotted in Figure 2.6. The vertical dispersion function η_y is zero around the entire ring, as stated in Sec. 1.2.

The role of the damping ring is to reduce emittance and momentum spread of the beam through radiation damping process. The characteristic time of this damping process, the damping time, is calculated to be about 20 msec without wiggler. Thus, the beam reaches its equilibrium after injection in less than 200 msec. The horizontal emittance in equilibrium condition is basically determined by the balance of radiation process (cooling) and excitation process (heating), which in turn is determined by the lattice functions.

The best way to reduce the horizontal equilibrium emittance is to minimize the horizontal dispersion at the bending part. A unique low-emittance lattice, called FOBO (a periodic optics of a focusing quadrupole and a (combined-function) bending magnet), is employed for this purpose. The lattice function of a FOBO cell is plotted in Figure 2.7. A defocussing component of magnetic field is combined in the bending magnet. As a result, the horizontal dispersion function is made small at the center of the bending magnet. Each arc section is formed by 17 FOBO cells.

As for the vertical emittance, it is mostly originated from the imperfectness of the machine. It can be reduced by precise alignment of the magnets and beam tuning. The target value of the vertical emittance is less than 1% of the horizontal emittance.

The main parameters of the damping ring is summarized in Table 2.1.

Table 2.1: Parameters of the ATF damping ring. (without wigglers)

Parameter	Symbol	Value
Beam Energy	E_0	1.28 GeV
Ring Circumference	C	138.6 m
RF Frequency	f_{RF}	714 MHz
RF Voltage	V_c	286 kV
Momentum Compaction	α_M	0.00214
Natural Emittance	ϵ_0	1.07 nm
Natural Momentum Spread	$\Delta p/p$	5.43×10^{-4}
Nominal Horizontal Tune	ν_x	15.17
Nominal Vertical Tune	ν_y	8.56
Damping Time	τ_x	17.0 ms
	τ_y	27.3 ms
	τ_s	19.5 ms

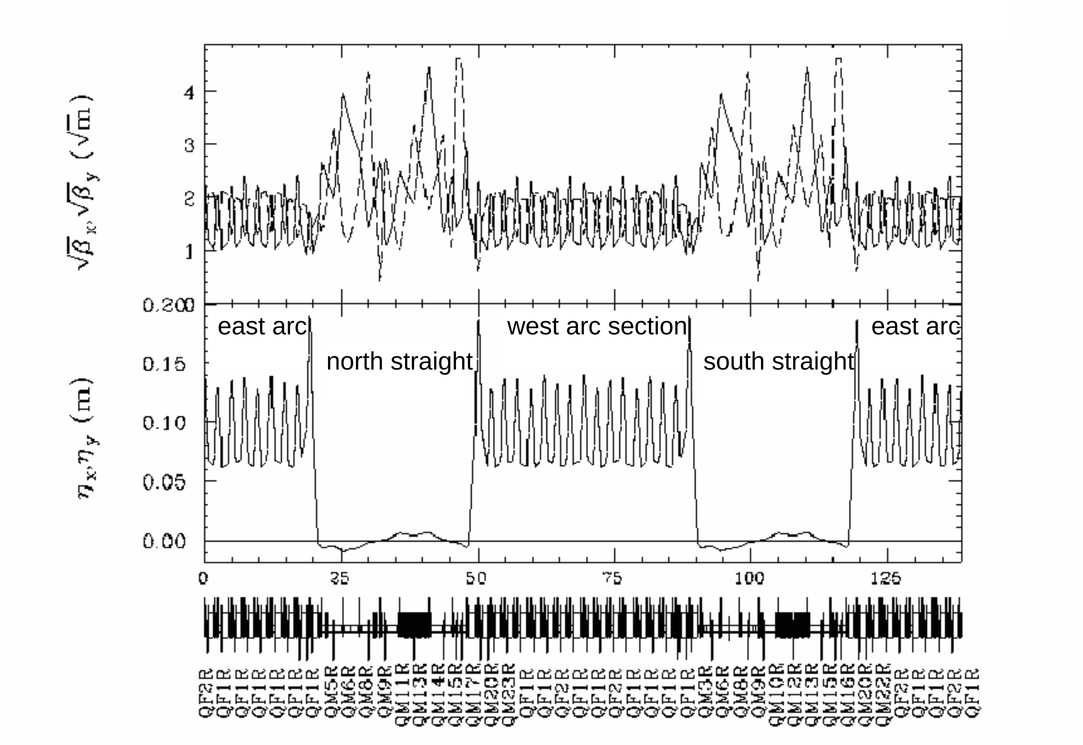

Figure 2.6: Optical functions of the entire damping ring. The square root of the beta function ($\sqrt{\beta}$), which is proportional to the beam size, and the dispersion function (η) of the horizontal and vertical planes are plotted.

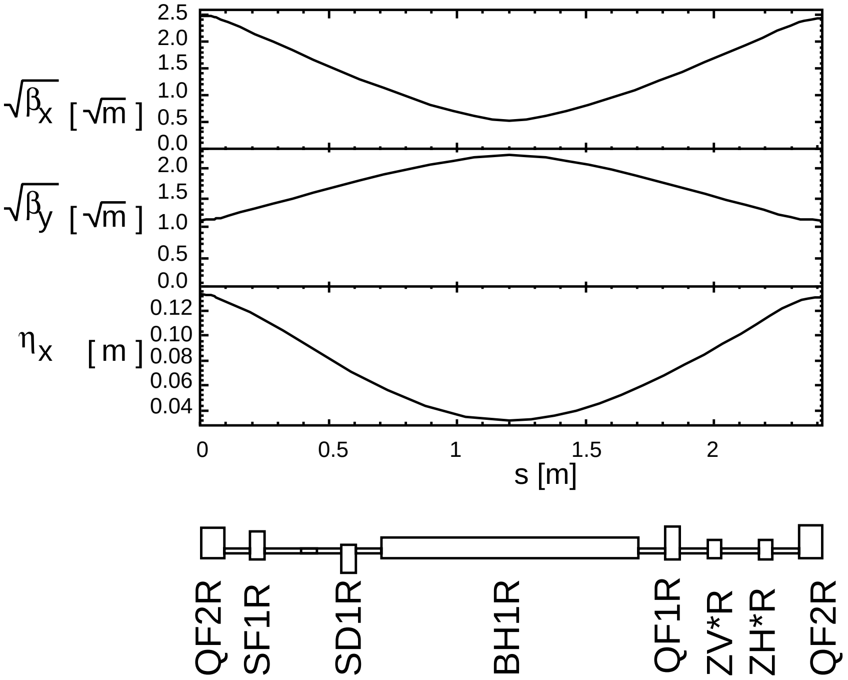

Figure 2.7: Lattice functions of the normal cell. It consists of a combined-function bending magnet (BH1R), two focusing quadrupole magnets (QF1R and QF2R) a pair of focusing and defocussing sextupole magnets (SF1R and SD1R), and a pair of horizontal and vertical steering magnets (ZV*R and ZH*R).

2.1.4 Extraction line

After the stored beam reaches the equilibrium, an extraction kicker system kicks it out to the extraction line. The layout of the extraction line is shown in Figure 2.8. Monitors installed in the extraction line examine various beam properties, such as the momentum spread and the emittance. Development of various instrumentations and experiments of beam handling are also carried out in this line. The beam is stopped at the beam dump placed at the end of the extraction line.

2.2 Instrumentation

Various monitors are necessary to operate the accelerator. We give a brief explanation for each monitor used in the studies described in this thesis.

2.2.1 Measurement of beam intensity

Two types of beam intensity monitors are used in the damping ring, namely DC Current Transformer and Wall Current monitor. The former is used to accurately measure the total beam current stored in the ring, while the latter to measure the beam intensity of each bunch in a multi-bunch mode.

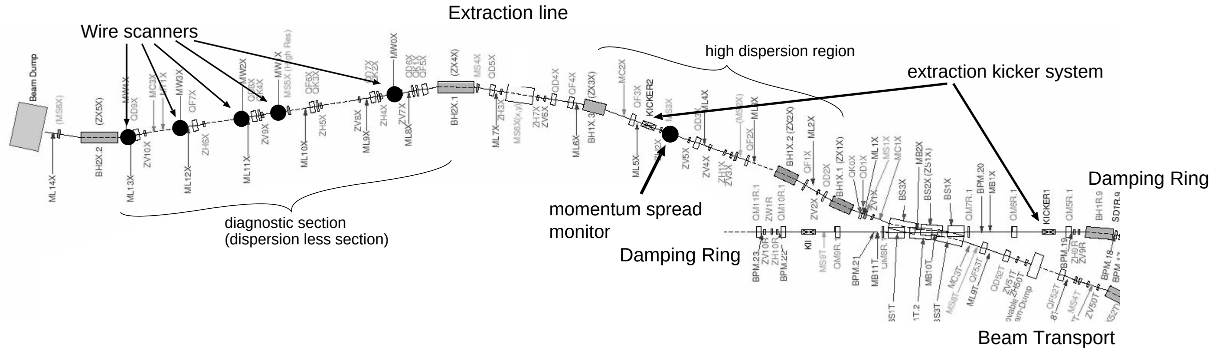

Figure 2.8: Layout of the extraction line. The beam in the damping ring is kicked out to this line by a kicker system. The momentum spread is measured by a screen monitor placed in the high dispersion region. The transverse emittances are measured by the wire scanner system.

DC Current Transformer (DCCT)

A DCCT measures a total beam current stored in the ring. The principle of this monitor is illustrated in Figure 2.9. A toroidal core, made of ferromagnetic material, surrounds the beam, and the beam current induces a magnetic field in the core. The toroidal core is periodically driven to its positive and negative saturation by the modulation winding, which induces a current in the pick-up winding. The beam's dc current generates magnetic field, which in turn shift the saturation point of the toroidal core. It is detected as a second harmonic component in the picked-up signal. To achieve a good accuracy, it is operated in a closed loop system (null measurement). An additional winding (feedback winding) is driven so as to cancel out the effect of beam current. The current supplied to the feedback winding is monitored as the beam current.

Wall Current Monitor (WCM)

When an electron beam passes through a metal beam pipe, an image current is induced on the inner surface of the pipe and moves with the beam. It is called a wall current, and used to measure the beam intensity. The principle of this monitor is illustrated in Figure 2.10. An insulating material is inserted into the beam pipe in this monitor, and the wall current is measured as a voltage appeared on the insulator. The time response of this monitor is determined by the impedance of the insulator and the capacitance of the beam pipe gap, and it is better than the bunch spacing (2.8 nsec). The relative intensity distribution of a multi-bunch beam can be monitored by this monitor. This monitor is useful when tuning the beam injection into the damping ring, especially in the multi-bunch mode.

2.2.2 Beam position monitor

In order to measure the beam orbit, 96 beam position monitors (BPMs) are installed in the damping ring. Figure 2.11 shows a structure of the BPM. Four button-type electrodes

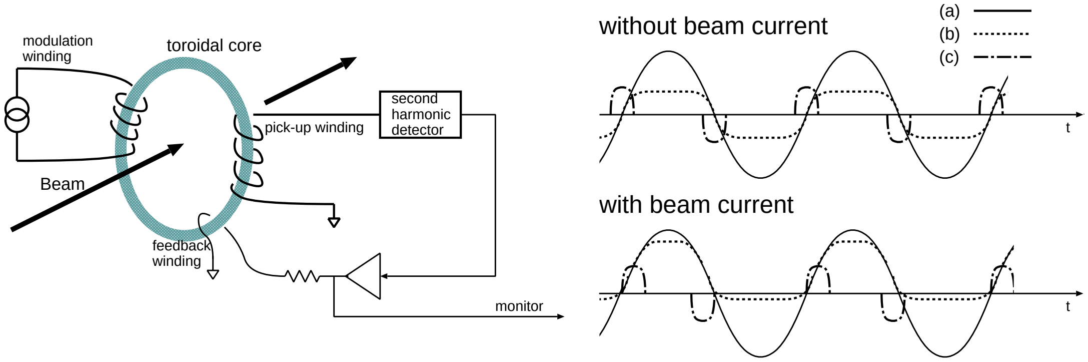

Figure 2.9: Principle of the DCCT monitor. The beam induced magnetic field is measured by a toroidal core. To measure the dc current, the toroidal core is driven to its saturation points by a modulation winding. The solid line (a) shows the current applied to the modulation winding, the dotted line (b) the magnetic field in the toroidal core, and the dash-dotted line (c) the induced current in the pick-up winding due to the magnetic field of the core. Presence of the beam current shifts the saturation point of the toroidal core, resulting in distortion of the pick-up signal.

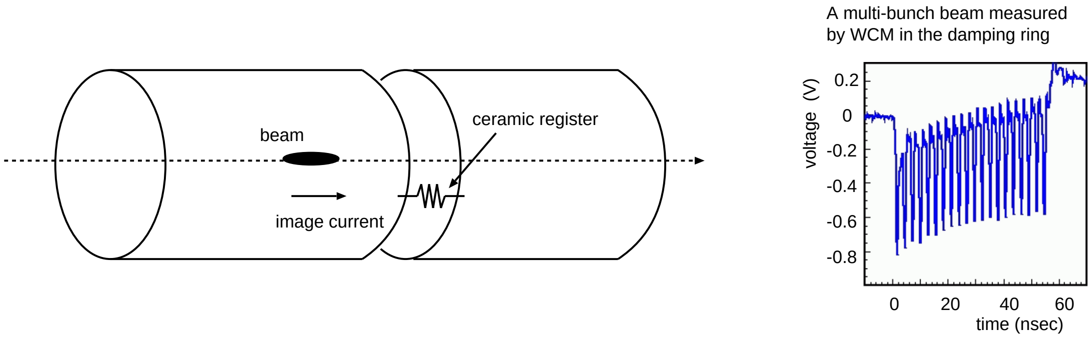

Figure 2.10: Principle of the wall current monitor. The wall current is measured by a voltage appeared in the cylindrical insulator (ceramic register). An example of the wave form measured in a multi-bunch mode is shown in right. The relative intensity distribution in a train can be measured.

are mounted with a roll angle of 45 degree to avoid direct synchrotron radiation. Passage of a charged particle beam induces an image charge on the electrodes. It is detected as a bi-polar signal pulse.

The signal amplitude depends on the beam intensity and the distance between the beam and the electrodes. The beam position is thus proportional to the signal asymmetry of two electrodes facing each other;

$$u = S_u \frac{V_1 - V_3}{V_1 + V_3} \tag{2.1}$$

$$\text{and} \quad v = S_v \frac{V_2 - V_4}{V_2 + V_4} \quad , \tag{2.2}$$

where u and v are the transverse coordinates associated with the electrodes. S_u and S_v are some sensitivity coefficient determined by the geometrical structure. They are estimated to be about 6388 when the beam passes through near the axis.

Since the electrodes have the roll angle of 45 degree with respect to the beam plane, the actual horizontal and vertical positions are given by

$$\begin{pmatrix} x \\ y \end{pmatrix} = \frac{1}{\sqrt{2}} \begin{pmatrix} 1 & -1 \\ 1 & 1 \end{pmatrix} \begin{pmatrix} u \\ v \end{pmatrix} \quad . \tag{2.3}$$

To process the signals from the BPMs, an electronics module called a clipping circuit is used. This module converts the bi-polar signal from each electrode of BPM into uni-polar by a Schottky diode. Then, it is detected by 14-bit charge sensitive ADCs. A typical position resolution of the BPMs is about 2 μm at the beam intensity of 10^{10} electrons/bunch ([12]). By changing the timing of the gate signal of ADCs, beam orbit of any revolution can be measured.

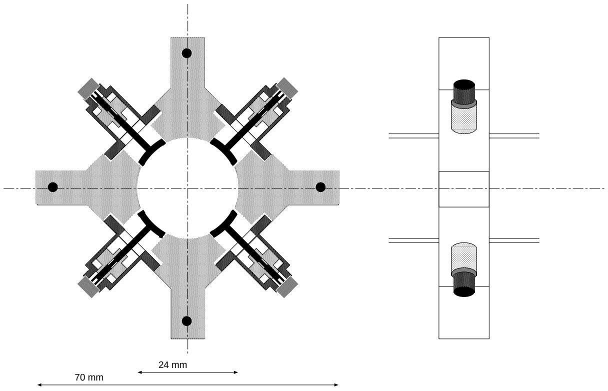

Figure 2.11: Schematics of the button type beam position monitor. The cross sectional view (left) and the side view (right) are shown. Four electrodes are placed in 45 degree with respect to the beam plane.

2.2.3 Beam exciter and the measurement of the betatron tune

The betatron tune is an important parameter which represents the beam condition. It is the period number of betatron oscillation in one revolution around the ring. The design value of the horizontal (vertical) tune is 15.17 (8.56).

A strip-line kicker (called a beam exciter) is installed for tune measurement. A schematic illustration showing its principle is displayed in Figure 2.12. A high voltage pulse induces a transverse kick to a beam, which in turn excites a coherent betatron oscillation around the closed orbit. The signal from a BPM is recorded in every beam revolution.

A Fourier analysis of the signal gives the oscillation frequency of the beam position. The decimal part of the betatron tunes (ν_x and ν_y) can be extracted from the frequencies determined in this way.

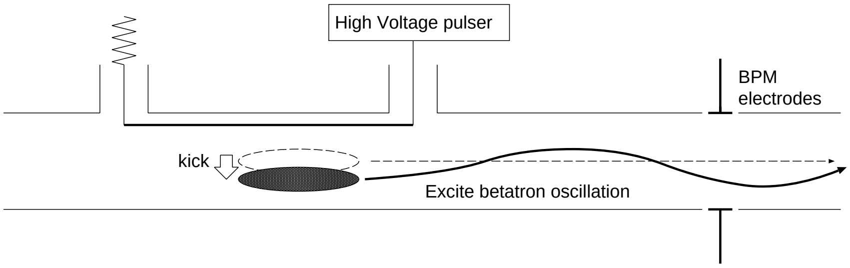

Figure 2.12: Principle of the beam exciter. A coherent betatron oscillation is excited by a strip-line kicker. The vibration of the beam position is measured by a BPM.

2.2.4 Momentum spread monitor

The beam momentum spread is measured in the extraction line. A screen monitor placed in a high dispersion region is used for this purpose. A phosphor screen of 130 μm thick is inserted in the beam line with an angle of 45 degree, as shown in Figure 2.13. It is viewed by a CCD camera through a telescope lens.

The horizontal beam size σ_x at this screen is known to be dominated by the dispersion term (η_x), and is given by

$$\sigma_x = \eta_x \frac{\Delta p}{p} \quad . \tag{2.4}$$

The dispersion function at the screen monitor was estimated by measuring the change in the position caused by the change in damping ring's RF frequency (beam energy). It was found to be η_x=1.79 m. The beam size on the screen (σ_x) was estimated by fitting the profile image data with a Gaussian function, and then the momentum spread $\frac{\Delta p}{p}$ was determined by Eq.2.4.

2.2.5 Streak camera

The bunch length (σ_z) of the beam was obtained by measuring the time structure of the synchrotron-radiation (SR) light. The SR light from one of the bending magnets in the arc section was transported to a streak camera ([13]).

The principle of the streak camera is illustrated in Figure 2.14. The SR light is focused on a photo-cathode inside the camera, and converted to photo-electrons. They

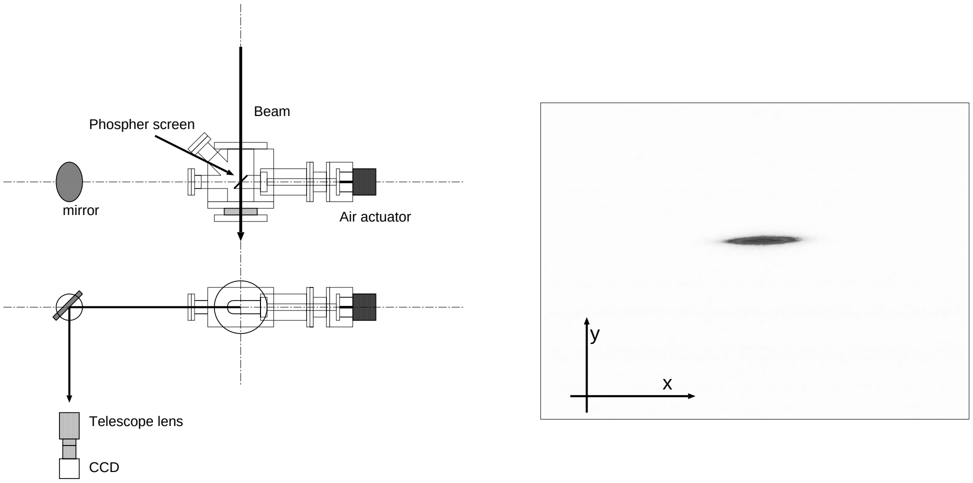

Figure 2.13: Momentum spread monitor (screen monitor). A screen is inserted in the extraction line, and is monitored by a CCD camera with a telescope lens (left) . An example of the beam image is shown (right). The horizontal size of the image is dominated by the momentum spread.

fly toward the micro-channel plate (MCP) along the field lines of an applied high-voltage. A pair of electrodes sandwiches the photo-electron orbit, and sweeps it vertically upon the application of a ramping voltage. It thus converts the photo-electron longitudinal structure into the vertical profile, which is imaged on a screen downstream of the MCP. The image on the screen is measured by a CCD camera. The time axis was calibrated by changing the optical path length of the input.

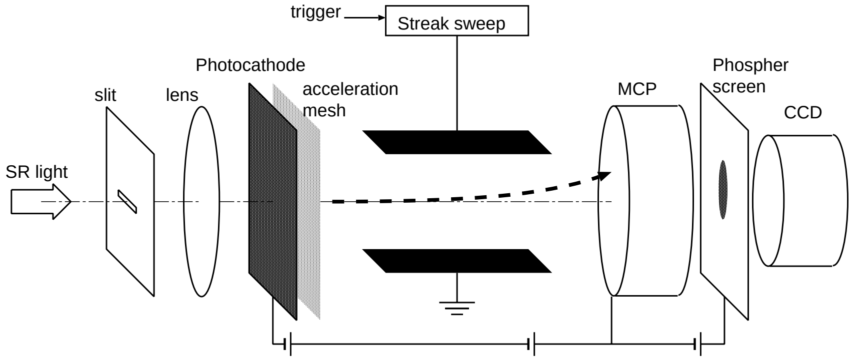

Figure 2.14: Schematics of the streak camera. The orbit of the photo-electron is swept by a pair of electrodes. The vertical axis of the obtained image corresponds to the time axis of the bunch.

2.2.6 Beam profile monitors

Laserwire beam profile monitor

This monitor is based on the Compton scattering of electrons with a laser light target. A thin and intense laser beam (laserwire) is produced by exciting a Fabry-Perot optical cavity, and it is scanned across the electron beam. From the flux of the Compton scattered photons as a function of the wire-position, the transverse profile of the electron beam is obtained. Thus, the beam profile in the damping ring can be measured in a direct way (a kind of scanning device). We utilized this monitor in this work. Its detail will be explained in Chapter 3.

Other beam profile monitors

Solid-wire scanners The emittances of the extracted beam are measured by a wire-scanner system ([14]). Tungsten wires of 10 μm diameter are installed in horizontal, vertical, 45 degree and 10 degree direction in a system. The horizontal (vertical) wire is used to measure the vertical (horizontal) beam size, and the angled wires to estimate the beam tilt. An Cherenkov detector placed downstream of the beam line measures the flux of the γ ray produced in the collision of the wire and beam.

There are 5 sets of the wire scanner system in the dispersion-less section of the extraction line, and they measure beam size development along the phase advance of the beam optics. From the beam sizes measured at 5 wire-scanner positions, the emittances are extracted from a fitting analysis with the Twiss parameters of the incoming beam and the emittance left as free parameters.

SR interferometer Spatial coherence of synchrotron radiation is utilized to monitor the beam size in the damping ring ([15]). Synchrotron radiation of visible light region from a bending magnet is transported to a double-slit interferometer. The interference pattern is measured by a triggerable CCD camera. From the visibility of the interference pattern, the beam sizes at the source can be estimated. The smaller is the beam size, the larger is the visibility. This monitor can measure the beam size of 5$\sim$50 μm. However, the visibility can be worsened by various reasons besides the beam size, for example, the intensity imbalance of two slits and the mechanical vibration of the light-transport system. Those difficulties limit the practical resolution/reliability around 10 μm. This monitor can measure the beam size on the shot-by-shot basis. This property makes the monitor extremely useful during beam tuning procedures.

FZP monitor A kind of microscope in X-ray region is being developed ([16]). This monitor also uses synchrotron radiation from a bending magnet in the damping ring. A monochromator made of silicon crystal selects 3.24 keV X-ray in SR. It is transmitted through a lens system formed by a couple of Fresnel Zone Plates (FZP), and is imaged on an X-ray CCD camera. The magnification of the system is designed to be 20. Since the pixel size of the CCD camera is 24 μm $\times$ 24 μm, it is expected to have a beam size resolution better than 2 μm. The advantage of this monitor is the possibility of the real time measurement of two-dimensional beam profiles. It requires only 20 msec of exposure time to obtain enough signals. Not only the beam sizes but also the tilt of the profile can be measured. The system is still under development. The systematic effects caused by misalignments of the FZP lenses are being studied.

ODR monitor A beam size monitor based on the optical diffraction radiation (ODR) is being developed in the extraction line ([17]) . ODR is a kind of wake-fields generated by a passage of an electron beam near a conductive object. Actually, a metal slit with an aperture of 260 μm is placed in the beam line. When an electron beam passes through the slit, radiations of visible light are emitted from both edges of the slit. They generate an interference pattern, which contains information of the beam size. Its sensitivity to the beam size depends upon the slit width. An image-intensifier tube (IIT) and a CCD camera placed 3 m from the slit detect the profile of the radiations. In principle, this monitor can measure the beam size in a single passage of a beam, making of an extremely fast monitor free from the jitter of beam orbit. The difficulty is the fabrication of the metal slit. Flatness over a large area and sharpness of the slit edges are crucial. The SR light from a bending magnet can be backgrounds to the detected light. Further development works are required to make a reliable beam size monitor.

2.3 Production of a low emittance beam

As explained in Sec. 1.2 and Sec. 2.1.3, the horizontal emittance is basically determined by the ring's optics functions. This ideal emittance is sometime called a natural emittance, and is expected to be realized actually when the current intensity is low (no collective effects). As for the vertical emittance, its ideal value is extremely small, and the actual emittance is determined by various errors (imperfection) of the ring's optics functions caused by misalignments and field errors of the magnets.

In this section, we describe various efforts needed to minimize the errors in the optics function, and explain how to achieve a ultra-low vertical emittance.

2.3.1 Sources of the vertical emittance growth

There are two dominant sources of the vertical emittance: the residual vertical dispersion and the x-y coupling of the betatron motion. Both of them are generated by the imperfection of magnet alignment and/or magnetic field. Figure 2.15 illustrates three major configurations of magnet misalignments (or magnetic field error) which strongly affect the vertical emittance. A vertical position offset of quadrupole magnets kicks the beam in the vertical direction, which in turn generates a dispersion in the vertical plane. A rotation of quadrupole magnets generates a skew-component of field, which transforms the horizontal betatron motion into the vertical direction (x-y coupling). A vertical offset of sextupole magnets also generates a skew-quadrupole component, producing a x-y coupling.

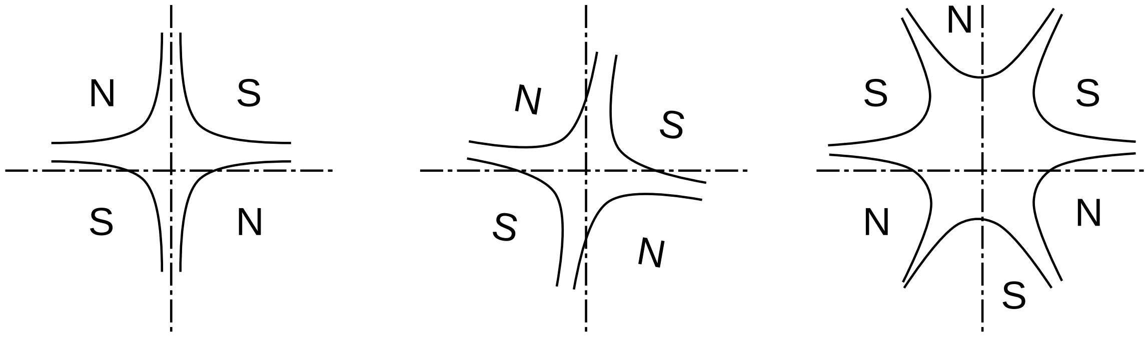

(a) Quadrupole offset (b) Quadrupole rotation (c) Sextupole offset

Figure 2.15: Various misalignments of the magnets. The cross point of the dot-dashed lines indicates the central beam orbit.

2.3.2 Precise alignment of the accelerator components

Mechanical alignment

To minimize errors in the ring optics function, alignment of the components should be done in good precision. A 3D mobile tracking system ([18]) is used for the alignment work. This device measures the distance and angles with respect to a reference target by laser interferometry. The resolution of the measurement is 1.3 μm (distance) and 3.4 μrad (angle) . Each magnet has a reference plane defined on its upper plate, where the reference target is attached. Figure 2.16 and 2.17 are the results of the measurement carried out in July 2003. The tolerances in the position offset are determined from simulation studies; they are ± 90 μm (horizontal) and ± 60 μm (vertical), respectively. Most of the components are aligned within these tolerances. Those measured positions are included in the database for the simulation and correction code for machine tuning.

Beam based alignment

Fabrication errors of the magnets might shift the field-center from its mechanical-center. For the beam, the field-center is more important. In order to correct the beam orbit to the field center, the difference of the field center and its mechanical center has to be measured. To this end, a method called beam based alignment (BBA) is employed. The actual effect of the magnetic field on the beam can only be known from the response to the beam motion ([19]). If a beam orbit goes through the true field center of focusing magnets, then change in the field strength would not affect the orbit, as shown in Figure 2.18(a). On the other hand, if a beam orbit is off the field center, it would receive a transverse kick, as shown in Figure 2.18(b). Therefore, we searched for the orbit that was insensitive to the change in the field strength, and recorded the measured offset (distance between the actual field and mechanical center) for every magnet. The offsets of the BPM reading with respect to the center of the nearest magnet were also obtained at the same time. The measured offsets (both the magnet center and the BPM offset) were included in the beam tuning codes.

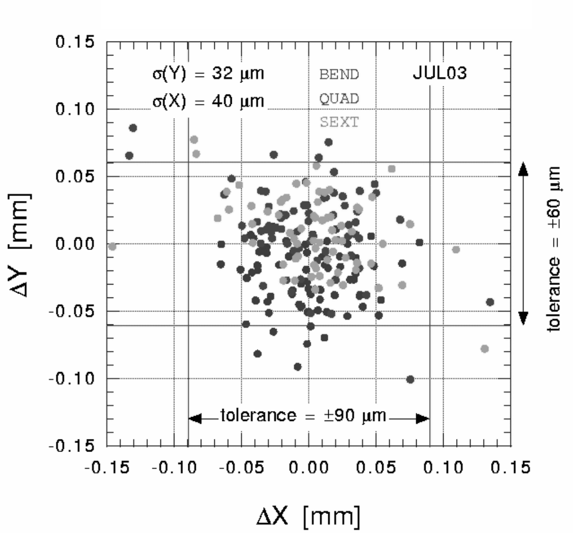

Figure 2.16: Transverse positioning of the magnets. The horizontal (ΔX) and vertical (ΔY) displacement from the ideal position for each magnet is shown by the dot.

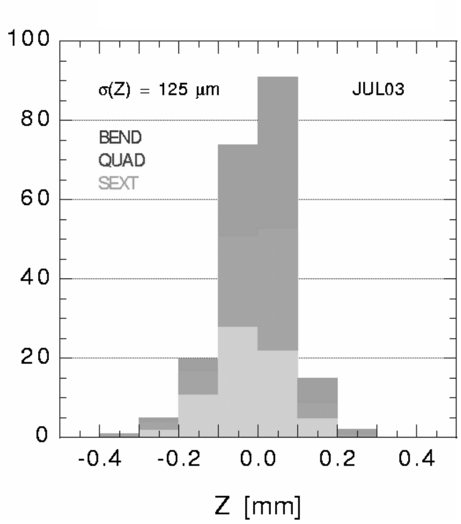

Figure 2.17: Longitudinal positioning of the magnets. The distribution of the measured errors in the longitudinal position is shown in the histogram.

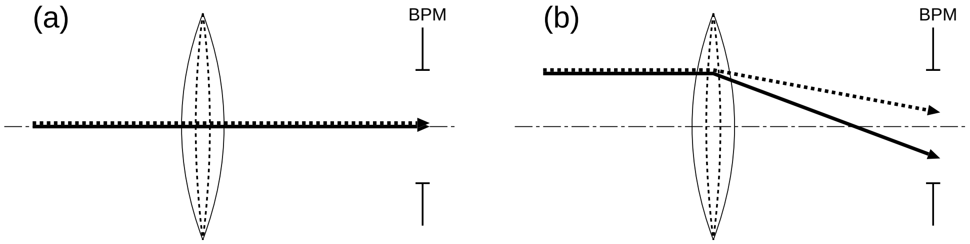

Figure 2.18: Principle of the beam based alignment. (a) Null offset case: The beam orbit remains same even when the strength of the field is changed. (b) Finite offset case: The beam orbit changes with the strength of the field. The orbit realizing the null offset case (a) is searched in the beam-based alignment method.

2.3.3 Beam tuning

The final tuning to minimize the vertical emittance is done by a combined correction of COD-dispersion using the steering magnets, and by x-y coupling correction using the skew magnets. All those methods are based only on the measurement of beam orbit ([20]) and trial and error procedures with beam size monitoring is not necessary.

Dispersion measurement

By definition, a change in the beam energy introduces a change in the orbit as

$$\Delta x(y) = \eta_{x(y)} \frac{\Delta p}{p} \quad , \tag{2.5}$$

where $\eta_{x(y)}$ is the dispersion in the $x(y)$ plane, p the nominal momentum, and Δp the particle's actual momentum with respect to p.

The dispersion function of entire ring is obtained by measuring the change in the orbit induced by a slight energy change. To change the energy, an RF cavity frequency is changed. In fact, the beam energy in the damping ring is proportional to the frequency of the RF cavity, expressed by

$$\frac{\Delta p}{p} = \frac{1}{\alpha_M} \frac{\Delta f}{f_{RF}} \quad , \tag{2.6}$$

where α_M ($= 0.00214$) is the momentum compaction factor and f_{RF} ($= 714$ MHz) the nominal frequency of the RF cavity. Usually, the RF frequency is changed by 10 kHz, and the change in the orbit is measured by BPMs . Figure 2.19 shows an example of such a measurement.

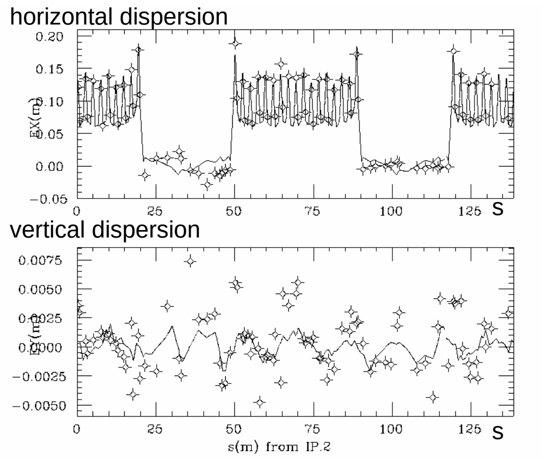

Figure 2.19: Example of the dispersion measurement. From the orbit displacement induced by the 10 kHz shift of the RF frequency, the dispersion functions in the ring are measured. Each data point, indicated by the circle, corresponds to the position of the BPMs. The solid line is the fitting result based on the optics model. (up: horizontal, down: vertical direction)

Coupling measurement

The strength of the x-y coupling is estimated from the measurement of the "leakage" from horizontal motion into vertical motion. To this end, a horizontal steering magnet is excited to generate a large horizontal orbit distortion, and the corresponding effect in the vertical plane is measured. The strength of the x-y coupling is defined as the ratio of the vertical displacement to the horizontal displacement, and it is calculated along the ring. Figure 2.20 shows an example of such measurement results.

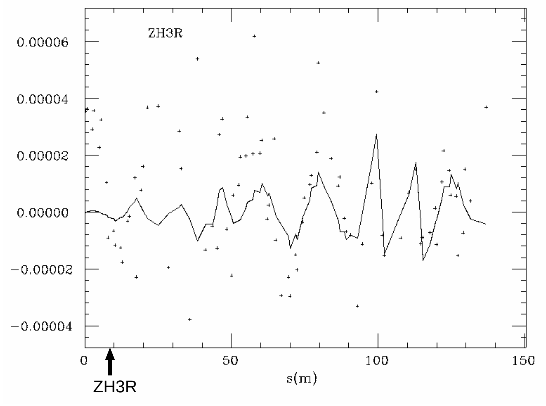

Figure 2.20: Example of the coupling measurement. A horizontal steering magnet (ZH3R) is excited to make a horizontal oscillation, and the induced orbit distortion in the vertical plane is measured. The ratio of the vertical displacement to the horizontal displacement, the x-y coupling coefficient, is plotted along the ring. The data point represents the measured value at each BPM. The solid-line is the fitting result, in which the strength of the skew correctors is made free.

Closed Orbit Distortion (COD) correction

The first correction to be applied is the closed orbit distortion (COD) correction. Ideally, the orbit should go through the field center of all focusing magnets. Actually, we employed the following measure for this process:

$$\langle x^2_{meas} \rangle = \frac{1}{N_{BPM}} \sum_i x^2_{i,meas} \tag{2.7}$$

$$\text{and} \qquad \langle y^2_{meas} \rangle = \frac{1}{N_{BPM}} \sum_i y^2_{i,meas} \quad , \tag{2.8}$$

where $x_{i,meas}$ and $y_{i,meas}$ are the measured horizontal and vertical beam positions at the i-th BPM and N_{BPM} is the number of BPM. The COD correction is done by adjusting steering magnets. Since the orbit response functions to each steering magnet are known, a unique combination of magnet settings which minimizes the above measures can be calculated.

Vertical COD-dispersion correction

As we stated, the vertical dispersion function is ideally zero. The residual vertical dispersion is corrected as follows. Since COD have to be kept small during this correction, the information of COD is included in the measure of this correction. The measure is:

$$\langle y^2_{meas} \rangle + r^2 \langle \eta^2_{y,meas} \rangle \tag{2.9}$$

$$\text{where} \qquad \langle \eta^2_{y,meas} \rangle = \frac{1}{N_{BPM}} \sum_i \eta^2_{y,i,meas} \quad , \tag{2.10}$$

$\eta_{y,i,meas}(\theta)$ is the measured vertical dispersion at the i-th BPM. The factor r is the relative weight of the dispersion and COD, and it is chosen to be 0.05 based on a simulation study.

Since the response functions of dispersion to each steering magnet are known, a unique combination of magnet settings can be calculated.

Coupling correction

The measure for the x-y coupling correction is

$$C_{xy,meas} \;=\; \sqrt{\frac{1}{N_{steer}} \sum_{i}^{\text{all h-steer}} \frac{\sum_{BPM} {\Delta y^{(i)}_{meas}}^2}{\sum_{BPM} {\Delta x^{(i)}_{meas}}^2}}\quad , \tag{2.11}$$

where N_{steer} is the number of the used steering magnets, $\Delta x^{(i)}_{meas}$ and $\Delta y^{(i)}_{meas}$ are the measured horizontal and vertical orbit change due to the change of i-th horizontal-steering magnet. ${\Delta y^{(i)}_{meas}}^2/{\Delta x^{(i)}_{meas}}^2$ is the response ratio, means the "leakage" from the horizontal motion to vertical. We note that ${\Delta y^{(i)}_{meas}}^2/{\Delta x^{(i)}_{meas}}^2$ is the "local" x-y coupling strength caused by the i-th steering magnet.

In order to measure $C_{xy,meas}$ in good precision, a large horizontal orbit distortion is induced by a horizontal steering magnet to measure the vertical leakage. Since there are some node points in the betatron oscillation amplitude induced by the horizontal kick, we choose two steerings which are apart by approximately $3/2\pi$ in horizontal and $1/2\pi$ in vertical phase advances. It makes possible to measure all the local couplings.

The x-y coupling, which is originated from a skew component of the field, can be compensated by a skew field of opposite polarity. Trim coils of all 68 sextupole magnets are wired so as to produce skew quadrupole fields. The winding scheme of the trim coils is illustrated in Figure 2.21. We call this winding a skew collector.

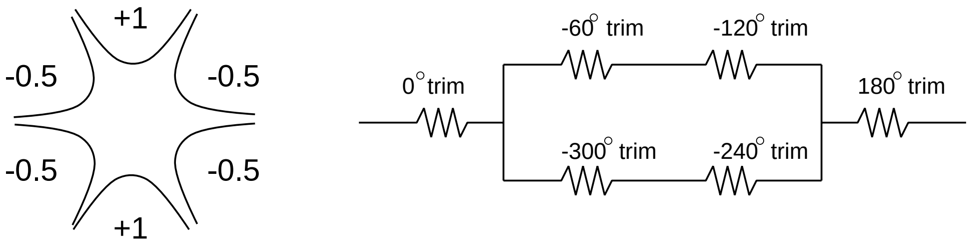

Figure 2.21: Skew winding of the sextupole magnets. All sextupole magnets have additional trim windings. The right figure shows the connection of the trim windings. When the trim winding is excited, a magnetic field depicted in left figure is produced (+ or - means the polarity, N or S). This field contains a skew quadrupole component, and is used to compensate the x-y coupling.

The response functions of the vertical leakage from horizontal motion by each skew corrector are known. The setting values of all the skew correctors to minimize the measure can be calculated.

Expected vertical emittance

The usefulness of the beam tuning procedure described above was confirmed by a computer simulation code called SAD. In the simulation, the mechanical misalignment of the magnets and the offset of the BPM are taken into account as actually measured. In addition, to allow residual magnet errors, alignment offset and rotation errors are randomly added. These errors are generated according to a Gaussian distribution with their rms width given in Table 2.2. Then the SAD simulation program calculates the vertical emittance for a given magnet setting. A series of correction procedures (COD ⇒ COD-dispersion ⇒ coupling correction) is made in the same manner as the actual beam tuning. The final value for the vertical emittance after the entire process depends upon the initial magnet setting given in the simulation. To understand and estimate the impact of initial conditions, the simulation is repeated 500 times with different initial conditions chosen randomly. The distribution of the resultant vertical emittance are plotted in Figure 2.22 at the each stage of the correction processes. We can conclude from the figure that each correction procedure is effective in reducing the vertical emittance, and that the target value (1×10^{-11} rad·m) can be achieved with a strong possibility. At the same time, the alignment tolerance for magnets and the requirement of the BPM resolution are determined. The experimental confirmation of the low emittance achievement will be explained in Chapter 4.

Table 2.2: Random errors applied to the magnets in the simulation.

components	applied random errors (rms)
Offset of magnets	30 μm
Rotation of magnets	300 μrad
Offset of BPM	300 μm
Rotation of BPM	20 mrad

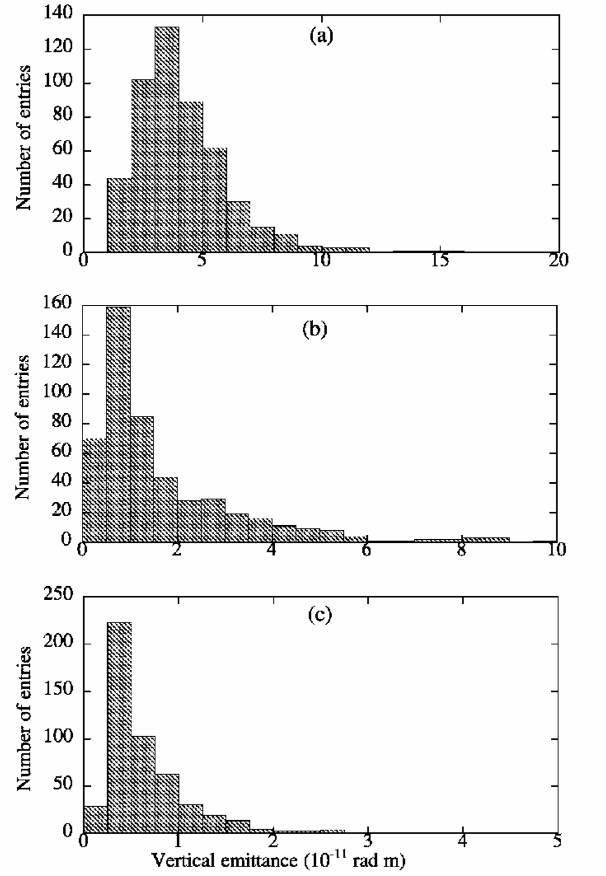

Figure 2.22: Simulation results for the vertical emittance. The expected vertical emittance is simulated by the SAD code for the different initial conditions assigned to the magnets. A series of correction procedures is made in the same manner as in the actual procedures. The distribution of the resultant vertical emittance are shown at each stage of the procedure. (a) After COD correction. (b) After the COD-dispersion correction to (a). (c) After the coupling correction to (b). Each entry in the distribution correspond to an initial conditions of magnets, which is chosen randomly 500 times. In most case, the vertical emittance is expected to be reduced less than 10 pm, the target value.

Chapter 3

Laserwire Beam Profile Monitor

In this chapter, we describe the laserwire beam profile monitor, the most important instrument for this work. This monitor directly measures the transverse profiles (in both vertical and horizontal directions) of the electron beam in the damping ring. All emittance measurements described in this thesis were done with this monitor. The development works of this monitor have been detailed in [22], [23] and [24].

3.1 Principle of the laserwire monitor

3.1.1 Principle of the measurement

The principle of the beam profile measurement using this monitor is as follows. Install a very thin laser beam (laserwire) in an electron beam orbit perpendicularly to the beam line as shown in Figure 3.1. When an electron beam crosses the laserwire, some of the electrons interact with the laser lights, and emit energetic photons in the forward direction via the Compton scattering process. A detector placed downstream of the collision point measures the flux of the scattered photons. By scanning a position of the laserwire across the electron beam while measuring the signal count rate; a transverse profile of the electron beam is obtained. Suppose both electron and laser beams have a Gaussian intensity distribution (with rms width σ_e and σ_{lw}, respectively), the measured profile is also a Gaussian shape with rms width σ_{meas} (expressed by $\sigma_{meas}^2 = \sigma_e^2 + \sigma_{lw}^2$). The actual size of the electron beam can be calculated by subtracting the width of the laserwire from the measured profile.

The important requirements for this monitor are as follows: make a laser beam thin enough to measure the width of a small electron beam, and to realize a laser intensity as high as possible to identify a signal among backgrounds of the beam line.

3.1.2 Compton scattering

First of all, we consider the differential cross section of the Compton scattering process and estimate the counting rate of the signal photon. In our case, a high energy electron hits a photon of visible wavelength and emits a high energy photon. (This process is sometimes called the inverse-Compton scattering.) We first calculate this process in the

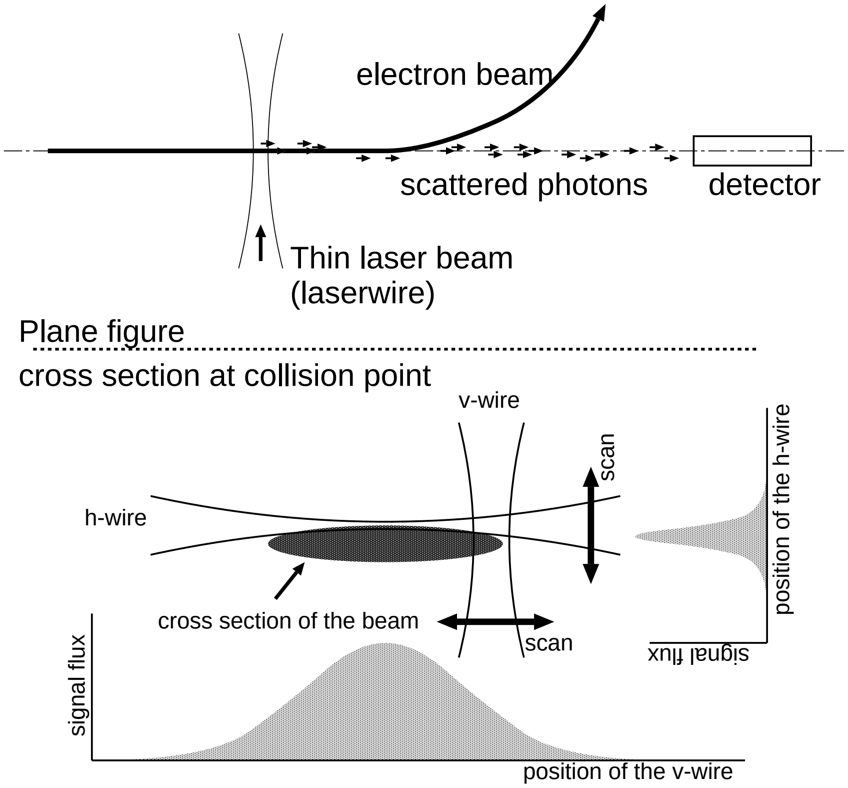

Figure 3.1: Principle of the beam size measurement by the laserwire. (top): A schematic layout of the setup. A laser beam is placed in the beam orbit perpendicularly, and the scattered photons are detected in the downstream. (bottom): The cross sectional view along the electron beam at the laser-beam interaction point. The waist size of the laser beam is focused smaller than the transverse size of the electron beam. Two laserwires, horizontal-wire (for the vertical measurement) and vertical-wire (for the horizontal) scan the electron beam in two directions.

rest frame of the electron, and then boost the final state to the laboratory frame. In this subsection, quantities with asterisk (*) are defined in the electron rest frame, and quantities with prime ($'$) are those in final state (after scattering).

The differential cross section of the Compton scattering in the rest flame of the electron (Figure 3.2) is given by the *Klein-Nishina* formula

$$\frac{d\sigma}{d\Omega^*} = \frac{r_0^2}{2}\left(\frac{\omega'^*}{\omega^*}\right)^2\left[\frac{\omega^*}{\omega'^*} + \frac{\omega'^*}{\omega^*} - 1 + \cos^2\theta'^*\right] \quad , \tag{3.1}$$

where r_0 is the classical electron radius, ω^* and ω'^* are the energy of the photon in the initial state and the final state, respectively, and θ'^* is the scattering angle of the photon. The relativistic kinematics defines a relation between ω'^* and θ'^* :

$$\omega'^* = \frac{m\omega^*}{m + \omega^*(1 - \cos\theta'^*)} \quad , \tag{3.2}$$

where m is the electron rest mass.

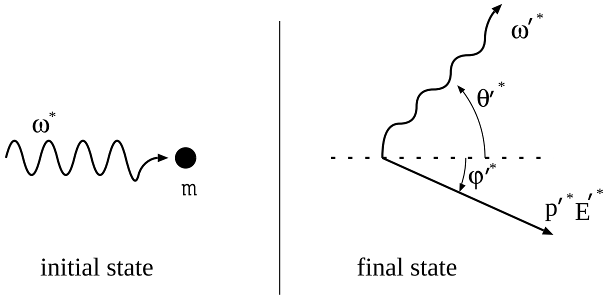

Figure 3.2: Compton scattering in the electron rest frame.

We now consider the Lorentz transformation between the laboratory frame and the electron rest frame. This is characterized by two parameters

$$\gamma = \frac{E}{m} \quad \text{and} \quad \beta = \frac{-p}{m} \quad . \tag{3.3}$$

When a photon collides with the electron in the right angle, as shown in Figure 3.3, then the energy and scattering angle (θ_0^*) in the electron rest frame are given by

$$\omega^* = \gamma\omega \tag{3.4}$$

$$\theta_0^* = \arctan(\frac{1}{\gamma\beta}) \quad , \tag{3.5}$$

where ω is the initial photon energy in the laboratory. In our case, θ_0^* is negligible because the energy of the electron beam is much higher than that of the photon. Similar relations in the final state read:

$$\omega'^* = \omega'\gamma(1 - \beta\cos\theta') \tag{3.6}$$

$$\cos\theta'^* = \frac{-\beta + \cos\theta'}{1 - \beta\cos\theta'} \quad , \tag{3.7}$$

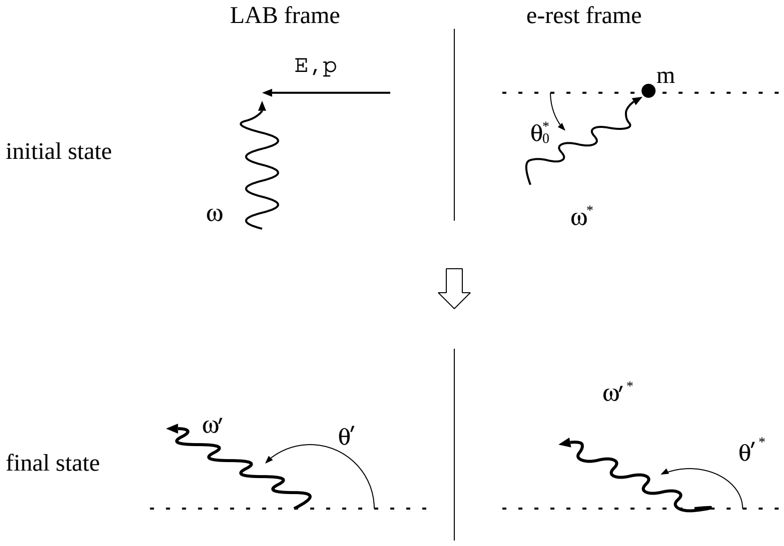

Figure 3.3: Lorentz transformation from the electron rest frame to the laboratory frame. In the initial state, a photon collides an electron beam in a right angle in the laboratory frame. This phenomenon is a head-on condition in the electron rest frame (θ_0^* is negligible in our case). After the scattering, an energetic photon is emitted in the forward direction of the electron orbit in the laboratory frame.

where ω' is the scattered photon energy in the laboratory frame, θ' and θ'^* are the scattering angle of the photon in the laboratory frame and electron rest frame, respectively.

Using these relations above, the differential cross section in the laboratory frame is

$$\begin{aligned} \frac{d\sigma}{d\Omega} &= \frac{d\sigma}{d\Omega^*}\frac{d\Omega^*}{d\Omega} && (3.8) \\ &= \frac{1}{2}r_0^2\left(\frac{\omega'^*}{\omega^*}\right)^2\left[\frac{\omega^*}{\omega'^*}+\frac{\omega'^*}{\omega^*}-1+\cos^2\theta^*\right]\frac{1}{\gamma^2(1-\beta\cos\theta)^2} \quad . && (3.9) \end{aligned}$$

Some of the important relations of our case (beam energy = 1.28 GeV, wave length of laser = 532 nm and crossing angle = 90 degree) are plotted in Figure 3.4∼3.7. Figure 3.4 shows the energy spectrum of the Compton scattered photon. The scattered photon energy is correlated with the scattering angle; several values of interest indicated by vertical lines. Note that the aperture of the detector, which is defined by the collimator, corresponds to 0.2 mrad of the scattering angle. The energy-angle relation is shown in Figure 3.5. The signal yield is plotted as a function of the scattering angle in Figure 3.6; it can be seen that most of the signal are scattered in the forward direction. Figure 3.7 shows the total signal yield within a given angular aperture.

3.1.3 Estimation of the count rate

Next, we consider the collision luminosity as a function of the relative position of the laserwire and the electron beam. Let's suppose an electron beam of I [A] current crosses the laser target of P [W] with relative position offset of μ. Let's also suppose both electron and laser beam have a Gaussian distribution represented by

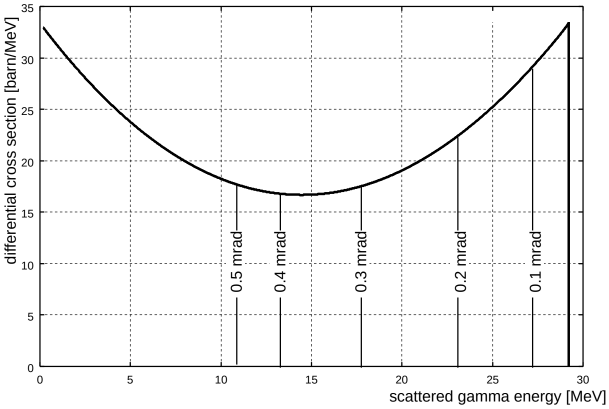

Figure 3.4: Energy spectrum of the Compton scattered photon. The differential cross section is plotted as a function of the energy of the scattered photon. Corresponding scattering angles are shown by vertical lines. The aperture of the detector is set 0.2 mrad.

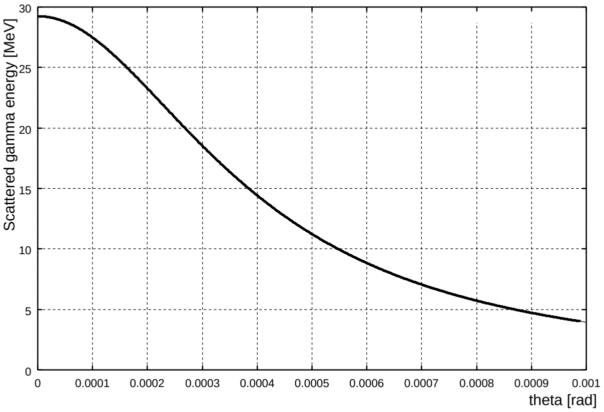

Figure 3.5: The energy of the scattered photon vs the scattering angle. The highest energy is 28.6 MeV, corresponding to the forward scattering (θ=0)

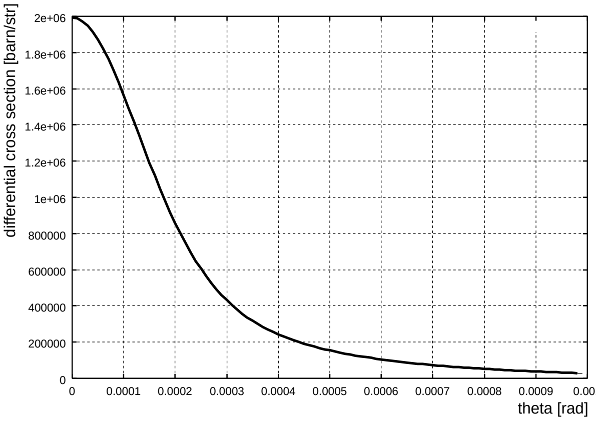

Figure 3.6: Differential cross section vs the scattering angle. Because of the Lorentz boost, most of the signals are scattered in the forward direction.

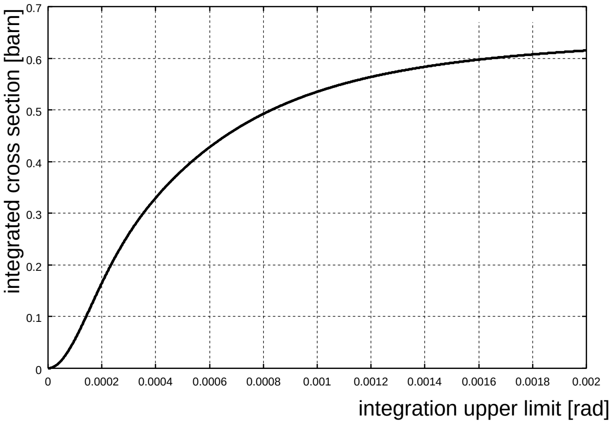

Figure 3.7: Integrated cross section within a given aperture. The integrated cross section is plotted as a function of the upper limit of an angle aperture shown in the abscissa.

$$\text{Electron distribution of a beam : } P_e(y) = \frac{I}{e}\frac{1}{\sigma_e\sqrt{2\pi}}\exp\left(-\frac{y^2}{2\sigma_e^2}\right) \tag{3.10}$$

$$\text{Photon distribution of a laser : } P_{lw}(y,\mu) = \frac{\lambda P}{hc^2}\frac{1}{\sigma_{lw}\sqrt{2\pi}}\exp\left(-\frac{(y-\mu)^2}{2\sigma_{lw}^2}\right) \tag{3.11}$$

The luminosity of this collision is given by the convolution of these two;

$$\mathcal{L}(\mu) = \int P_{lw}(y,\mu)P_e(y)dy \tag{3.12}$$

$$= \frac{\lambda}{hc^2}\frac{1}{e}\frac{1}{\sqrt{2\pi}\sqrt{\sigma_{lw}^2+\sigma_e^2}}\exp\left[-\frac{\mu^2}{2(\sigma_{lw}^2+\sigma_e^2)}\right] \tag{3.13}$$

$$\times P[\mathrm{W}] \times I[\mathrm{A}] \quad . \tag{3.14}$$

The event rate of the process ($\frac{dY}{dt}$) is calculated from the luminosity ($\mathcal{L}$) and the cross section of the process (σ):

$$\frac{dY}{dt} = \sigma\mathcal{L} \quad . \tag{3.15}$$

In order to give a feeling for the expected counting rate, we use the following representative values for the actual case;

laser wave length: $\lambda = 532$ nm
laser effective power: $P = 100$ W
integrated cross section (within the aperture of 0.2 mrad): $\sigma = 0.16$ barn
convoluted laser and electron beam size: $\sqrt{\sigma_{lw}^2+\sigma_e^2}$=10$\mu$m
electron current: $I = 1$ A

Then the expected counting rate is 3.5 kHz when the laser beam is placed at the center of the electron beam.

3.2 Optical cavity

We have employed a Fabry-Perot optical cavity. The laserwire is produced inside the optical cavity, and the electron beam passes through between the two mirrors, as shown in Figure 3.8. The role of the optical cavity is two fold. First, it enhances the effective laser power and thus the intensity of the signal. The enhancement factor depends on the reflectivity and loss factor of the cavity mirrors. Second, the geometrical properties of the laser beam inside the cavity are completely defined by the boundary conditions. This fact makes us free from details and/or variations of the laser profile.

In this section, we will describe the theoretical aspects of our optical cavity. An introductory explanation of optical cavities can be found in [26] or [27].

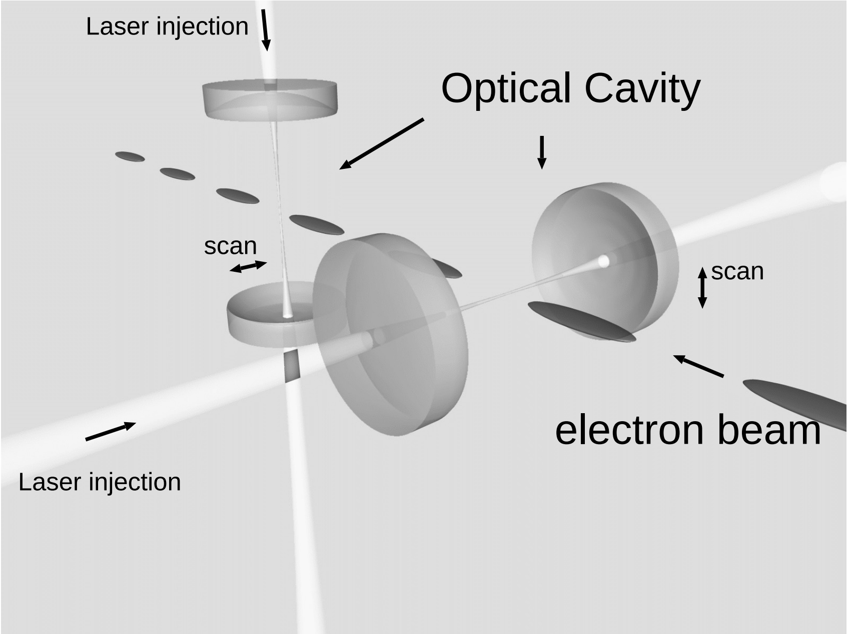

Figure 3.8: Schematic view of the laserwires interacting with the electron beam.

3.2.1 Principle of the power enhancement

First, we consider the power enhancement nature of an optical cavity. Here, we treat the laser beam as a plane wave for simplicity. An optical mirror splits a laser beam into two parts (into three if there is loss): reflected and transmitted part. The power-reflectance (R) and the power-transmittance (T) of a mirror are defined as the ratio of the reflected or transmitted power to that of the incident laser beam. When we consider a coherent summation of transmitted and/or reflected electromagnetic fields, it is convenient to introduce the amplitudes of the waves, namely an amplitude-reflectance ($r = \sqrt{R}$) and an amplitude-transmittance ($t = \sqrt{T}$).

When a laser beam is injected into the Fabry-Perot optical cavity from one end, a part of the beam comes inside the cavity and reflects back and forth between two mirrors. This phenomenon is schematically illustrated in Figure 3.9. The amplitude of each optical path can be calculated by considering the reflection and transmission experienced at the interface of the mirrors. The phase of the each optical path is calculated from the path length and the phase flip experienced at the mirror. The cavity's amplitude-transmittance t_{cav} (amplitude-reflectance r_{cav}) as a whole is the sum of all transmitted (reflected) waves;

$$\begin{aligned} t_{cav} &= t_1 t_2 [1 + r_1 r_2 e^{i\theta} + (r_1 r_2 e^{i\theta})^2 + \cdots] & (3.16) \\ &= \frac{t_1 t_2}{1 - r_1 r_2 e^{i\theta}} & (3.17) \\ r_{cav} &= r_1 - t_1 r_2 t_1 e^{i\theta} [1 + r_1 r_2 e^{i\theta} + (r_1 r_2 e^{i\theta})^2 + \cdots] & (3.18) \\ &= r_1 - \frac{t_1 r_2 t_1 e^{i\theta}}{1 - r_1 r_2 e^{i\theta}} \quad , & (3.19) \end{aligned}$$

where θ is the phase advance gained during one round trip inside the cavity. t_i and r_i are the amplitude-transmittance and amplitude-reflectance of the mirror i (i=1,2).

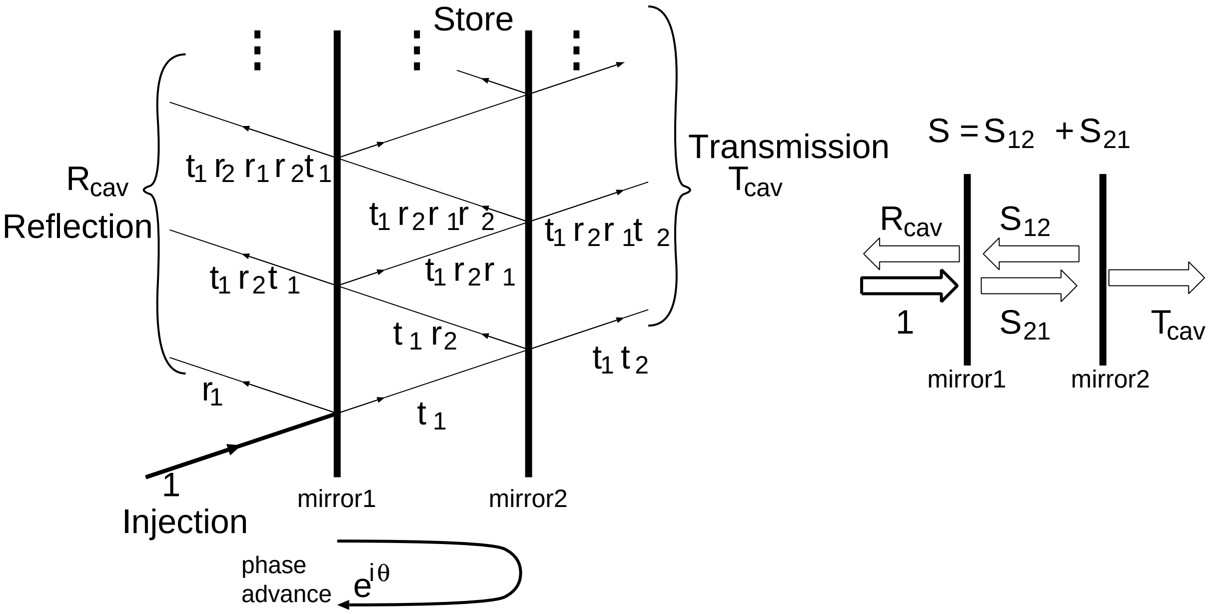

Figure 3.9: Schematic diagram of the power enhancement in an optical cavity.

The amplitude of the waves inside the cavity can be calculated in the same way. The amplitude of the wave going from mirror-1 to mirror-2 (s_{12}) and the one going from mirror-2 to mirror-1 (s_{21}) are

$$
\begin{aligned}
s_{12} &= t_1[1 + r_1 r_2 e^{i\theta} + (r_1 r_2 e^{i\theta})^2 + \cdots] && (3.20)\\
&= \frac{t_1}{1 - r_1 r_2 e^{i\theta}} && (3.21)\\
s_{21} &= t_1 r_2[1 + r_1 r_2 e^{i\theta} + (r_1 r_2 e^{i\theta})^2 + \cdots] && (3.22)\\
&= \frac{t_1 r_2}{1 - r_1 r_2 e^{i\theta}} \quad . && (3.23)
\end{aligned}
$$

The power-transmittance, the power-reflectance and the power enhancement factor of the cavity (T_{cav}, R_{cav} and S_{cav}, respectively) are obtained by squaring respective amplitudes;

$$
\begin{aligned}
T_{cav} &= |t_{cav}|^2 = \frac{T_1 T_2}{(1-\sqrt{R_1 R_2})^2 + 4\sqrt{R_1 R_2}\sin^2\frac{\theta}{2}} && (3.24)\\
R_{cav} &= |r_{cav}|^2 = (R_1 + T_1) - \frac{T_1(1 - R_1 R_2 - T_1 R_2)}{(1-\sqrt{R_1 R_2})^2 + 4\sqrt{R_1 R_2}\sin^2\frac{\theta}{2}} && (3.25)\\
S_{cav} &= |s_{12}|^2 + |s_{21}|^2 = \frac{T_1(1 + R_2)}{(1-\sqrt{R_1 R_2})^2 + 4\sqrt{R_1 R_2}\sin^2\frac{\theta}{2}} && (3.26)\\
&= \frac{1+R_2}{T_2} T_{cav} \sim \frac{2}{T_2} T_{cav} \quad (\text{if } R_2 \sim 1) \quad . && (3.27)
\end{aligned}
$$

The phase advance in one round trip, θ $(= 2\pi\frac{2L}{\lambda})$, depends on the cavity length and the wavelength of the light. It is convenient to define a quantity called the resonating efficiency η, which is basically the denominator of Eq. 3.24-3.26;

$$
\eta = \frac{(1-\sqrt{R_1 R_2})^2}{(1-\sqrt{R_1 R_2})^2 + 4\sqrt{R_1 R_2}\sin^2\frac{\theta}{2}} \quad . \qquad (3.28)
$$

It represents the resonating properties of a cavity; η becomes larger only when $\theta = 2n\pi$ (n: integer), and it is said the cavity is in resonance. As can be understood by Eq. 3.28, the width of the resonance is controlled by the mirror's reflectance; in particular, the full-width-half-maximum ($\delta\theta$) is given by

$$\delta\theta = \frac{1 - R_{eff}}{\sqrt{R_{eff}}} \tag{3.29}$$

$$\text{and} \quad R_{eff} = \sqrt{R_1 R_2} \quad . \tag{3.30}$$

Figure 3.10 shows η as a function of θ for several R_{eff} values, while Figure 3.11 shows T_{cav} and R_{cav} near the resonance.

This picture can also be defined in the frequency domain of the laser wave. The resonance period, which corresponds to π phase advance, is called Free-Spectral-Range (FSR) in the frequency domain and denoted by $\Delta\nu$. It is determined by the cavity length (L);

$$\Delta\nu = \frac{c}{2L} \tag{3.31}$$

where c is the speed of light. The full-width-half-maximum of the resonance is given by $\delta\theta$ in the phase; the corresponding quantity in the frequency domain is denoted by $\delta\nu$ (called the line width) and is given by $\delta\nu = (2\pi L/c)\delta\theta$. We now introduce an important cavity parameter called "finesse". This is defined as the ratio of $\delta\nu$ and $\Delta\nu$;

$$\mathcal{F} \equiv \frac{\Delta\nu}{\delta\nu} = \frac{\pi\sqrt{R_{eff}}}{1 - R_{eff}} \quad . \tag{3.32}$$

3.2.2 Properties of a laser beam

Gaussian beam

It can be shown that the Maxwell equation is simplified for a single frequency wave traveling in one direction (say z) to

$$\left(\frac{\partial^2}{\partial x^2} + \frac{\partial^2}{\partial y^2} + \frac{\partial^2}{\partial z^2} - 2ik\frac{\partial}{\partial z}\right)\psi(x,y,z) = 0 \quad , \tag{3.33}$$

where the scaler quantity ψ is a part representing spatial variation of the electric field E ($E(t,x,y,z) \equiv \psi(x,y,z)\exp(i\omega t - ikz)$), ω the angular frequency, and k the wave number.

In the case that a paraxial approximation holds ($|\frac{\partial^2}{\partial z^2}| \ll |k\frac{\partial}{\partial z}|$, $|\frac{\partial^2}{\partial x^2}|$ and $|\frac{\partial^2}{\partial y^2}|$), it can be further simplified to

$$\left(\frac{\partial^2}{\partial x^2} + \frac{\partial^2}{\partial y^2} - 2ik\frac{\partial}{\partial z}\right)\psi(x,y,z) = 0 \quad . \tag{3.34}$$

This equation holds in the vicinity of z-axis (called the near-axis wave equation), and is used to treat a field of laser beams.

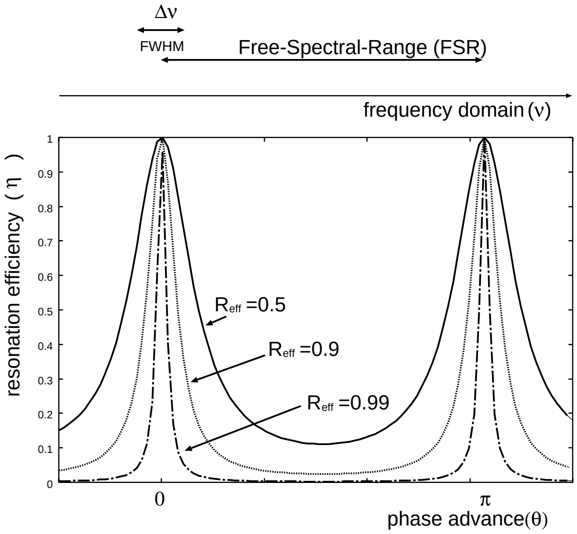

Figure 3.10: Resonance efficiency (η) as a function of phase advance (θ). An optical cavity resonates when the phase advance of one round-trip is an integer multiple of 2π.

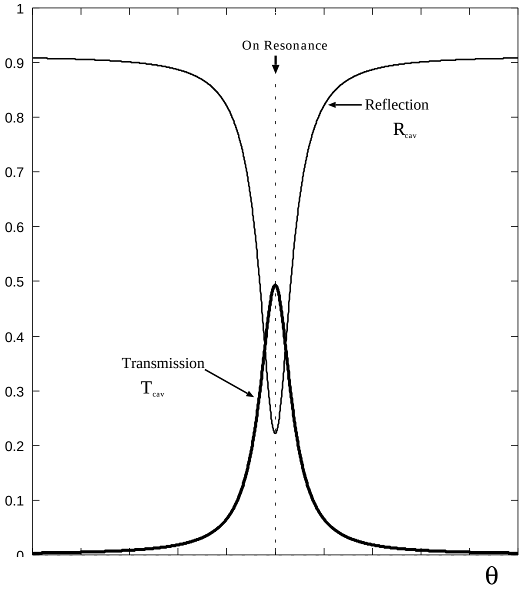

Figure 3.11: Cavity response near the resonance condition. Transmittance (T_{cav}) and reflectance (R_{cav}) of the cavity near the resonance condition.

An optical cavity introduces a geometrical boundary condition on Eq. 3.34. In order to realize an optical cavity, the wave-front of the field must coincide with the surfaces of the mirrors. The condition completely defines a set of electromagnetic fields which are allowed to resonate in the cavity. They are referred to as a Gaussian beam and denoted by TEM$_{mn}$ with m and n specifying various modes. Their electric field are represented by

$$\begin{aligned} E_{mn}(x,y,z) &= A\frac{w_0}{w(z)}\exp\left(-\frac{x^2+y^2}{w^2(z)}\right)H_m\left(\frac{\sqrt{2}x}{w_0}\right)H_n\left(\frac{\sqrt{2}y}{w_0}\right) \\ &\times \exp\left(-ik\cdot\frac{x^2+y^2}{2R(z)}\right)\exp\left(i\Phi(z)\right)\times\exp(i\omega t-ikz) \end{aligned} \tag{3.35}$$

with

$$w(z) = w_0\sqrt{1+\left(\frac{z}{z_0}\right)^2}, \tag{3.36}$$

$$R(z) = z\left\{1+\left(\frac{z_0}{z}\right)^2\right\}, \tag{3.37}$$

$$\Phi(z) = (m+n+1)\arctan\left(\frac{z}{z_0}\right), \tag{3.38}$$

$$z_0 = \frac{\pi w_0^2}{\lambda}, \tag{3.39}$$

where λ represents the wave length, $w(z)$ the beam spot size at the location z, $R(z)$ the curvature of the wave front, $\Phi(z)$ the Guoy phase factor, and z_0 the Rayleigh length.

$H_n(x)$ is the Hermite polynomial of n-th order. The parameter w_0 is called a beam waist, and represents the smallest spot size realized at $z = 0$. The wave-front curvature $R(z)$ must coincide with the curvature of the mirrors at the surface (ρ). We use TEM_{00} mode in this laserwire. This mode has a Gaussian intensity distribution in both transverse directions. The longitudinal shape of the solution and the relation to the mirrors are illustrated in Figure 3.12.

The beam waist (w_0) is related to the curvature of the mirror (ρ) and/or the cavity length (L). In fact, the condition that the wave-front at the mirrors to coincide with the mirror's curvature, $R(-L/2) = -\rho$ and $R(L/2) = \rho$, leads to the relation

$$w_0^2 = \frac{\lambda}{\pi} \frac{\sqrt{L(2\rho - L)}}{2} \quad . \tag{3.40}$$

In our case, ρ and L are mechanically fixed, hence, we can stably realize small w_0 over a long period of time.

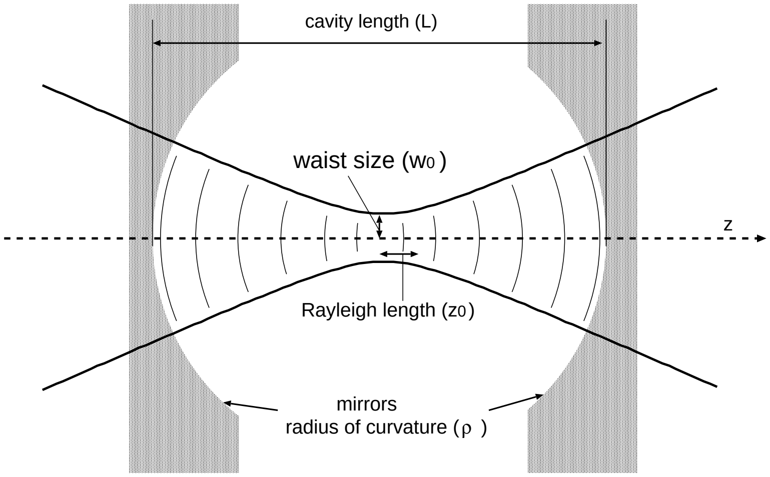

Figure 3.12: Pattern of the field allowed to exist in an optical cavity. The wave-front at the mirror must coincide with the shape of the mirror. The waist size at the center (w_0) is controlled by changing the cavity length (L) .

Resonance of a Gaussian beam in an optical cavity

Due to the additional phase (Φ : Guoy phase) in Eq. 3.38, the resonance condition discussed in Sec. 3.2.1 needs a modification in the case of the Gaussian beam. The phase advance in one round-trip should be integer multiples of π to satisfy a resonance condition. It depends not only on the cavity length but also on the Guoy phase. The Guoy phase depends both on the order of the transverse mode ($m + n$) and the beam waist (w_0). Hence, the various transverse resonances may be realized at different cavity length depending on the order of the mode. If we vary the cavity length and measure its resonances, then we should observe various modes with different orders at different cavity lengths. It is illustrated in Figure 3.13.

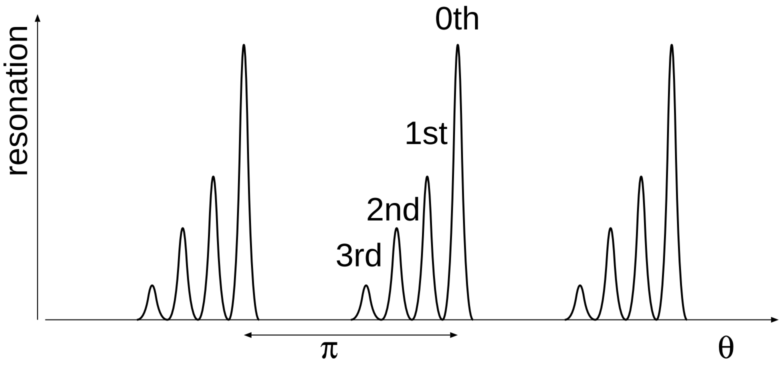

Figure 3.13: Resonance conditions of various transverse modes. The cavity length which satisfies the resonance condition depends on the order (m+n) of the modes. They appears as sub-peaks when the cavity length is swept.

3.3 Experimental setup

3.3.1 Layout

The experimental layout is shown in Figure 3.14. Two laserwires were installed in the north straight section of the damping ring. One is to measure vertical beam size (horizontal-wire) and the other to measure horizontal one (vertical-wire). The electron beam passes through from right to left at the interaction points. A photon detector was placed 12.7 m downstream of the vertical-wire. We designed the interaction points to be placed in the straight section of the ring. This made the emittance measurement free from the effects of the momentum dispersion. From the view point of detector backgrounds, however, this configuration had a disadvantage. Backgrounds were mainly caused by γ-rays which were in turn stemmed from beam loss of the spent electrons and beam scattering with residual gases. They tended to come along the beam, and thus most of the backgrounds generated in the whole north-straight section came into the detector. This problem was partly cured by placing collimators in front of the detector.

3.3.2 Optical system

Cavity assembly and the chamber system

The cavity and other related components were structured into one assembly called a cavity assembly. The cavity itself was composed of two spherical mirrors with the same curvature of $\rho = 20$ mm; they were apart by $L \simeq 40$ mm. The optical properties of the cavities will be detailed in Sec. 3.3.3. The cavity assembly consisted of two mirrors, mirror holder systems and a cylindrical spacer which defined the cavity length. In order to have precision control over the cavity length, both mirror holders were supported by a piezo actuator through a disk-type plate spring. The piezo actuators had a hollow to let a laser beam go through. The mechanical resonance frequency of the plate spring was found to be around 6 kHz. It limited the bandwidth of the feedback control on the cavity length.

There were two sets of cavity assemblies: one for the horizontal-wire and the other for the vertical one. They were mostly identical, but were placed in orthogonal. They were mounted in a vacuum chamber as shown in Figure 3.15. The laser beam was injected

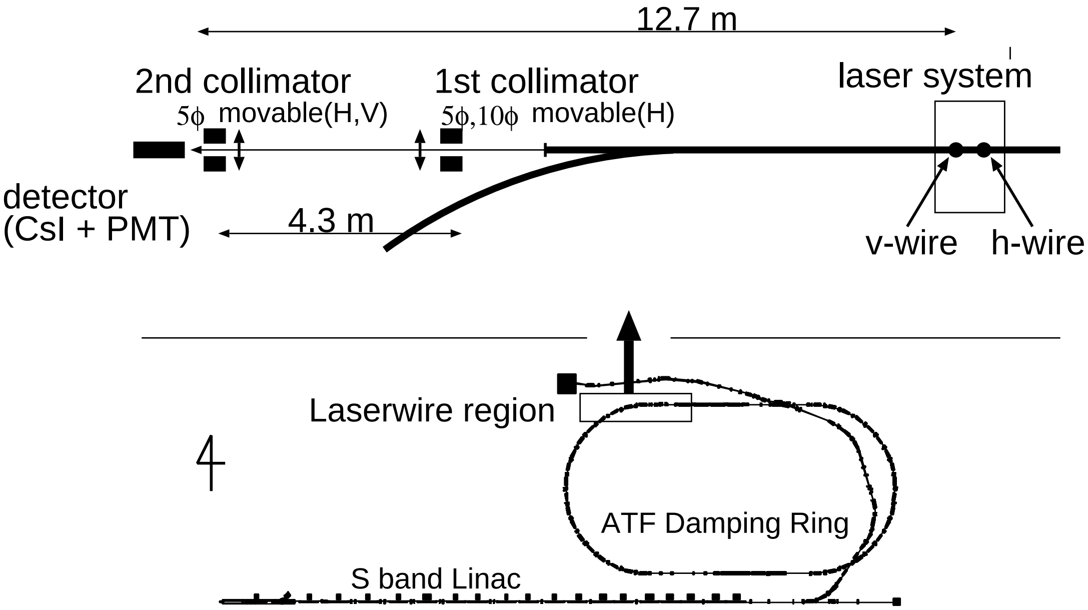

Figure 3.14: Layout of the laserwire setup.

through a view port attached on the flange. Two cavity chambers were installed in the beam line as shown in Figure 3.16.

Optical path and optical components

Figure 3.17 shows a schema of laser beam paths to the two chambers. The entire optical system was placed on a movable table. A detailed layout of optical components is displayed in Figure 3.18. It consisted of a CW laser, an optical isolator to protect the laser from the reflected light, a beam switching system, two sets of a matching lens system, two optical cavities, and several photo-diodes to monitor light intensities at various positions.

We utilized a diode-pumped solid state laser with a wave length of λ=532 nm (LightWave Series 142 [28]). This laser employs the Non-Planer Ring-Oscillator (NPRO) technique to realize ultra-low line width (10kHz/msec). Its nominal output power is 300mW. The beam switching system changes an optical path from one cavity to the other. This is a combination of a polarizing beam splitter (PBS) and a Pockels cell which rotates the polarization plane. The power transmission efficiency from the laser output to the matching section was found to be 50%. The switching efficiency, the ratio of the power going in the desired direction to that to the un-desired direction, was more than 95%. A set of mirrors downstream of the switching section aligned the injection axis with respect to the optical cavity. Two lenses were placed to make the laser beam match to the TEM_{00} mode of the cavity.

The transmitted light of an optical cavity is known to be proportional to the laser intensity inside the cavity (see Eq.3.24 and 3.26). Thus each of the cavities had a photodiode to monitor the transmitted light intensity. Signals from these monitors were also used in a feedback system to control the cavity length. A part of the transmitted light was projected on a screen to monitor its profile by a CCD camera. The reflected light

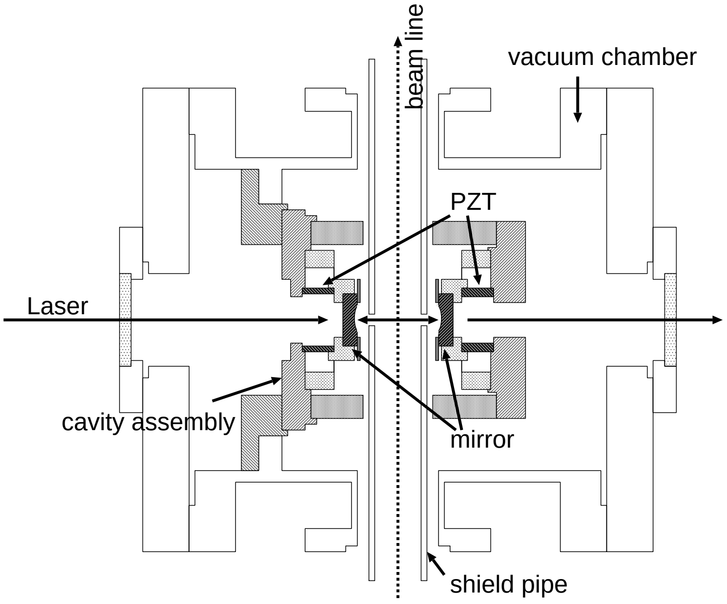

Figure 3.15: Cavity assembly and vacuum chamber. The cavity assembly (darkened parts) is mounted in the vacuum chamber. A laser beam is injected and extracted through the view ports on the flanges. A SUS shield pipe is inserted through in order to keep the impedance of the beam line constant. The pipe has two 5-mm-diameter holes to let a laser beam go through.

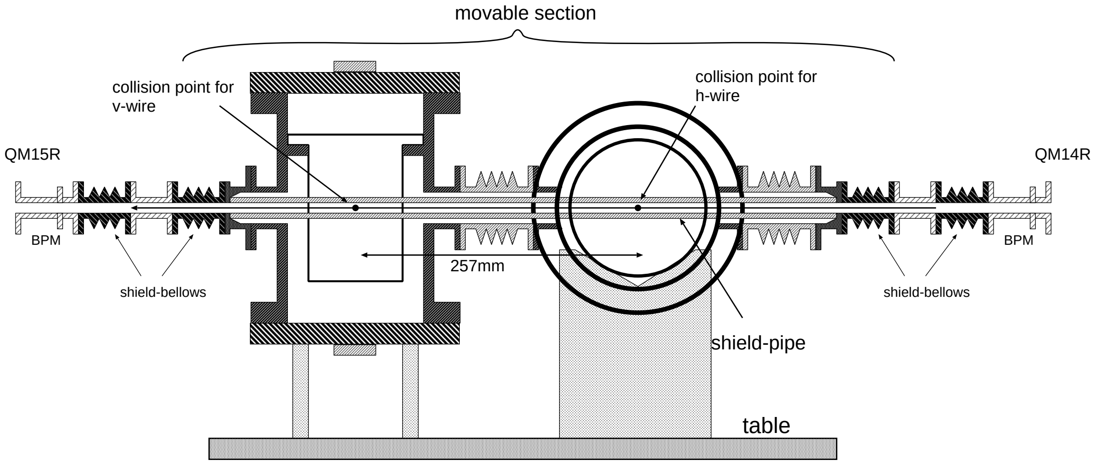

Figure 3.16: Chamber system of the laserwire. Two cavity chambers are placed on the movable table. They are connected to the other parts of the damping ring via two shield-bellows.

from the cavity was also monitored by a photo-diode.

Matching to the cavity mode

In order to excite the optical cavity efficiently, position, angle, spot-size and divergence of the injected laser beam have to be tuned to coincide with the fundamental transverse mode of the cavity. This tuning procedure is called mode matching. Imperfect matching excites higher-order modes in the cavity. To observe the excitation of various modes in the cavity, the cavity length was varied repeatedly by the piezo actuator (PZT). The piezo actuators were driven by a triangular wave through a HV amplifier. We call this operation of the PZT “sweep mode”. At first, excitations of some higher-order modes were observed as peaks in the cavity-transmittance signal (Figure 3.19(a)). Then the injection axis of the laser beam and the positioning of the two matching lenses were tuned to minimize the higher-order excitation. After this procedure was completed, prominent peaks except TEM_{00} could be eliminated (Figure 3.19(b)). The matching efficiency is defined to be the fraction of the injected power which coupled to the TEM_{00} mode of the cavity. We estimated the matching efficiency from the sizes of residual higher-order modes (in reality, we measured the lower modes of the order 3 or less). It was more than 80%.

3.3.3 Properties of the optical cavities and their control

Properties of the optical cavities

The qualities of the cavity mirrors (especially its loss factor at the surfaces) strongly affect the power gain of the cavity. We utilized multi-layer dielectric mirrors with high-reflectivity and low-loss factor (manufactured by REO [29]). The dimensions of the mirrors are shown in Figure 3.20. After being assembled into the cavity, various parameters were measured. During the measurement, the cavities were operated in the sweep mode as in the matching procedure. First, the finesse was measured from the ratio of the full-width-half-maximum of the resonance peak and the distance of the nearest TEM_{00} peaks. (see Eq.3.32). Then the cavity-transmittance (T_{cav}) and reflectance (R_{cav}) on resonance were measured. We also measured the transmittance of each mirror (T_1 and T_2). From those values, the power enhancement factor of the cavities could be estimated [30]. Given the mirror's parameter set (T_1, T_2, R_1 and R_2), finesse, T_{cav} and R_{cav} is calculated according to Eq.3.24∼3.27. A most likely mirror's parameter set which explains the all measured values of finesse, T_{cav}, R_{cav}, T_1, and T_2 was sought. Finally, S_{cav} was estimated using the best mirror parameters.

The actual cavity parameters are listed in Table 3.1. The measurement of the beam waist will be explained in Sec. 3.4.

Feedback control of the cavity and its power modulation

In order to subtract backgrounds from detected events statistically, the data with laser power off should be taken in addition to the ordinary measurements. To this end, we modulated the cavity length, and realized both laser “ON” and “OFF” states periodically.

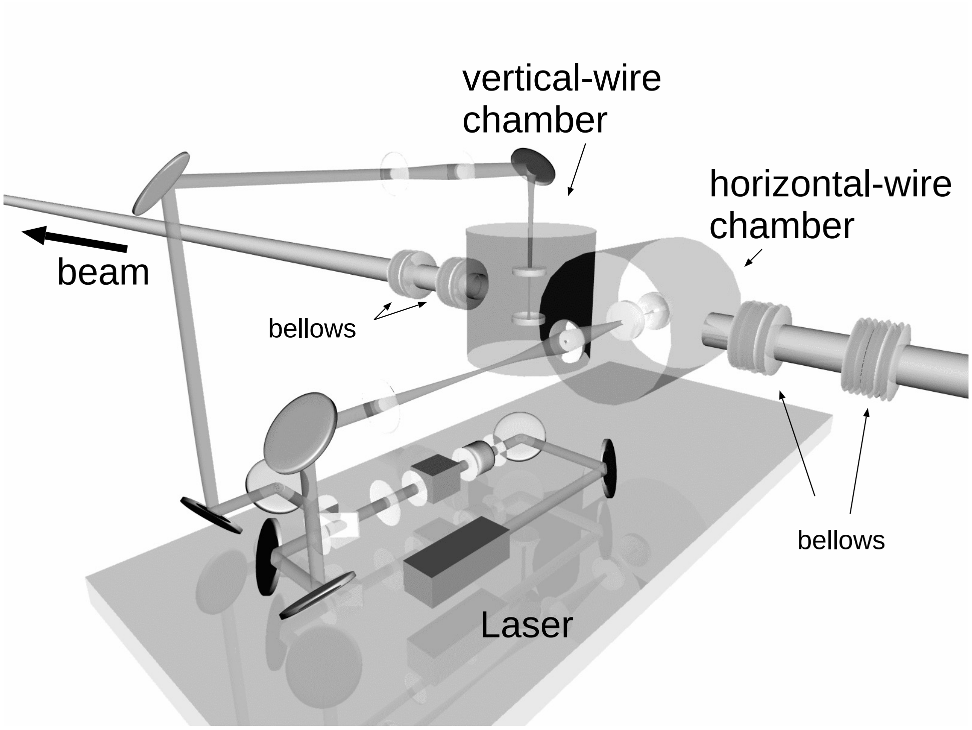

Figure 3.17: Bird's view of the laserwire vacuum chambers and the laser beam transport.

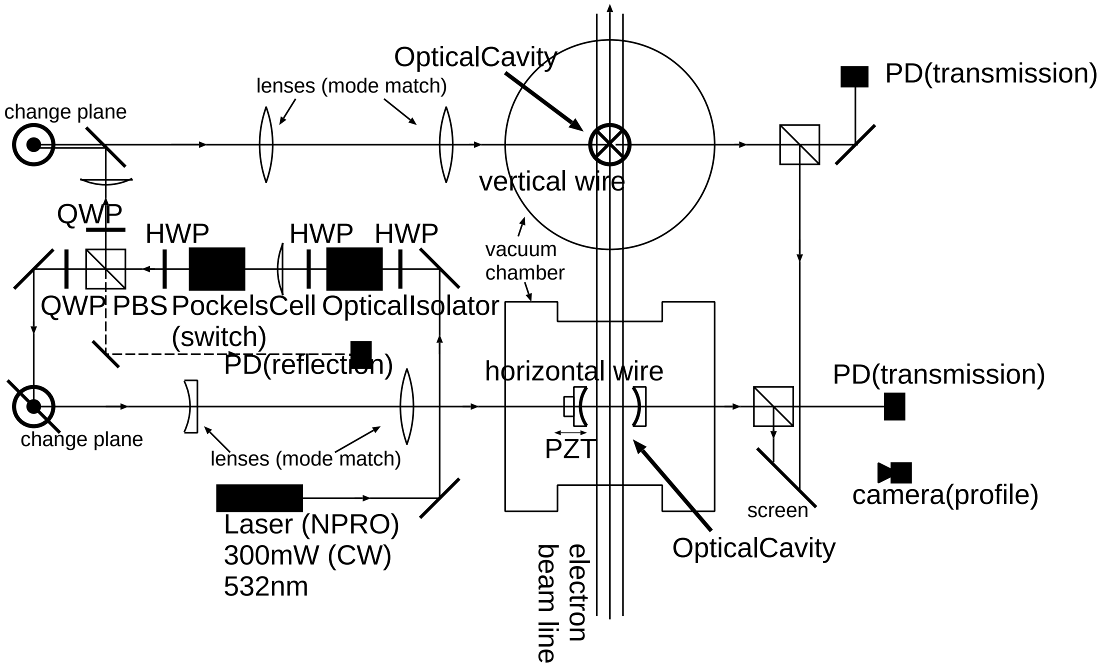

Figure 3.18: Layout of the optical components. The symbols stand for photo-diodes (PD), half-wave plate (HWP), quarter-wave plate (QWP), polarizing beam splitter (PBS), and piezo actuator (PZT).

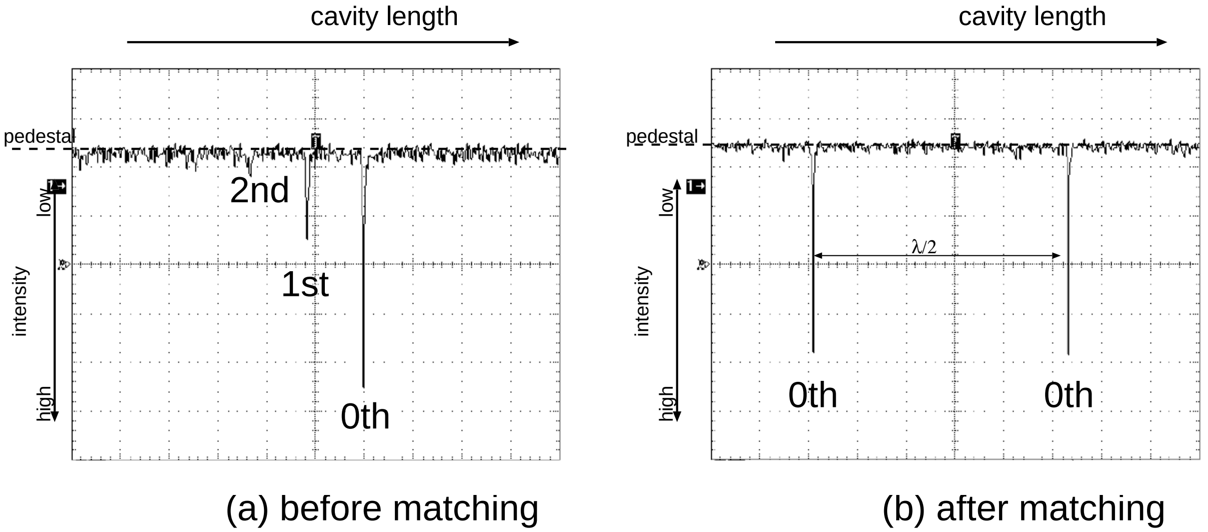

Figure 3.19: Mode matching procedure of the laser beam and the cavity. Before the tuning, excitations of some higher-order modes were observed in the sweep mode (a). After the tuning, only main peaks were seen in all free-spectral-range (b).

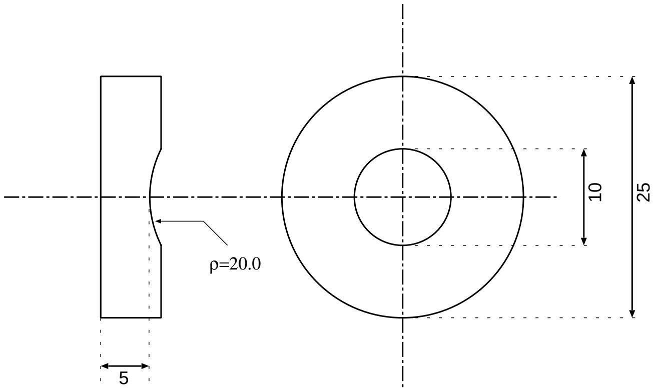

Figure 3.20: Geometry of the cavity mirror. The substrate is made of fused silica. The outer diameter is 25 mm and the thickness is 5 mm. The center part of 10ϕ has a concave shape and super-polished. The radius of the curvature is 20.0 mm.

Table 3.1: Specifications of the optical cavities.

parameter	horizontal wire	vertical wire
mirror reflectivity (front)	99.1% (Sigma)	99.8% (REO (coated by SOC))
mirror reflectivity (rear)	99.9% (REO)	99.9% (REO)
mirror curvature	20.0 mm	20.0 mm
finesse (measured)	620	1700
T_{cav}(on resonance)	0.22	0.57
R_{cav}(on resonance)	0.52	0.24
power gain	660	1300
effective laser power	79 ± 7 W	156 ± 13 W
waist size (w_0)	$11.30 \pm 0.16\ \mu$m	$29.43 \pm 0.47\ \mu$m
Rayleigh range	760 μm	5100 μm

Actually, the cavity length was set at the halfway of the resonance peak, and was varied by a sinusoidal modulation signal from the off resonance point to the top of the peak (see the inset of Figure 3.21). In order to keep the cavity resonating, its length must be controlled with an accuracy of less than 0.1 nm. A closed-loop feedback system was necessary to maintain the resonance condition. A schematic diagram of this feedback loop is displayed in Figure 3.21. A photo-diode signal monitoring the cavity transmittance was compared to a reference voltage set by a function generator. The mean value of the reference voltage was adjusted to the half of the maximum photo-diode output at the resonance peak. The error signal was formed by subtracting a photo-diode output from the reference voltage. After integration, it was feed-backed to the piezo actuator controlling the cavity length.

The photo-diode signal was also fed into a multi-level comparator to define the status of the optical cavity. The status of the cavity was classified into three states according to its effective power; they were “ON”, and ”OFF” states, and a state between these two. The threshold levels were set in such a way that the average power of the “ON” (“OFF”) state was about 85% (7.5%) of the maximum. The frequency of the modulation was about 100 Hz. The operation time was found to be distributed equally among these three states. Figure 3.22 displays actual outputs of the relevant signals. The transmission intensity of the cavity is displayed on the top. Other two channels shows the output of the comparator which defined cavity status.

3.3.4 Photon detector and collimators

A photon detector, placed 12.7 m downstream of the vertical wire, counted the signal yields. The energy range of the Compton signal is expected to be 23.0 − 28.6 MeV, where the high and low limits are determined by the kinematics and the collimator's bore radius (corresponding to the angle aperture of 0.2 mrad) placed in front of the detector. We used a pure CsI crystal of $70 \times 70 \times 300$ mm^3 as the photon detector (Figure 3.23). Figure 3.24 shows the result of a simulation on the detector response to the Compton

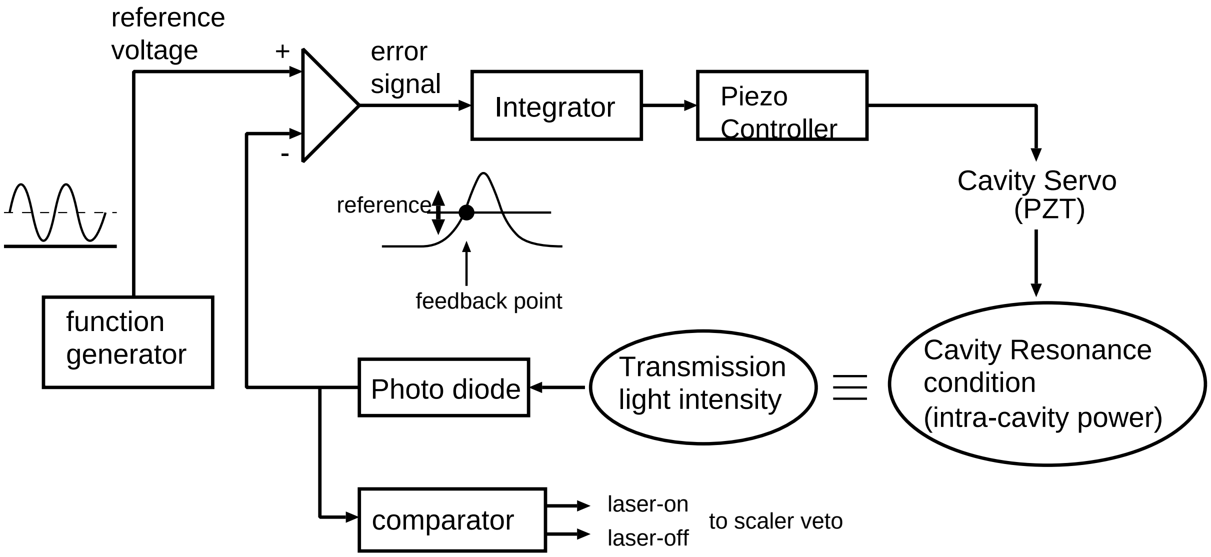

Figure 3.21: Schematics of the feedback circuit. The stored power in the cavity is monitored by measuring the transmittance signal. The error signal is formed by comparing it with a reference voltage given from a function generator. After integration, it drives the piezo actuator to control the cavity length.

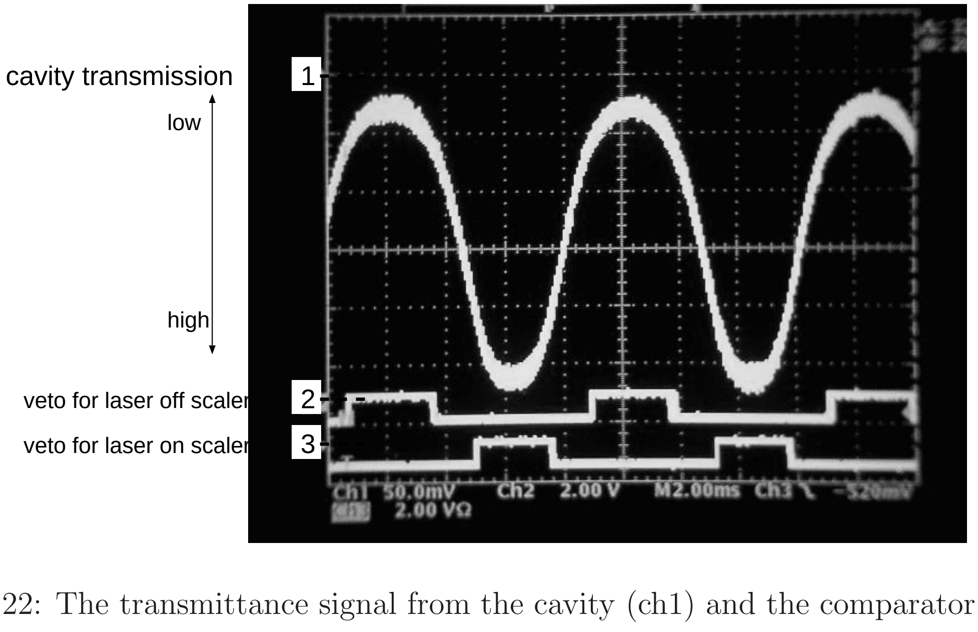

Figure 3.22: The transmittance signal from the cavity (ch1) and the comparator outputs (ch2 and ch3). The outputs of the comparator define the state of the cavity, and control the scaler's action.

signal. A 2-inch photomultiplier was attached at the downstream end of the crystal to detect its scintillation light. The energy scale was calibrated using through-passing cosmic rays (Figure 3.25).

In order to reduce backgrounds, a collimator system was placed in front of the detector. This collimator system consisted of two lead blocks of 100mm thick with a 5-mm-diameter bore. The first block was placed halfway between the interaction point and the detector (8.4 m downstream of the laserwire) while the second one right in front of the detector. The transverse positions of both blocks were remote controlled. Prior to beam size measurements, these collimators were aligned with respect to the beam axis. The alignment was performed in a beam-based way, monitoring energy spectrum of the Compton scattering events. This procedure will be detailed later in Sec. 3.3.7.

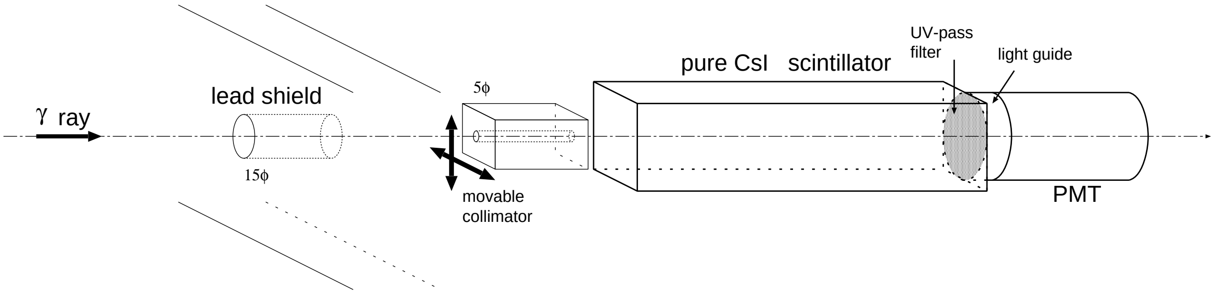

Figure 3.23: Photon detector setup. A pure CsI crystal viewed by a photomultiplier was used as a photon detector. Two movable collimator blocks are placed to reduce backgrounds. The detector and the second collimator is placed behind a lead shield with 15-mm-diameter aperture. The first collimate is also a 100mm thick lead block with 5-mm-diameter aperture and is placed 4.3 m upstream of the detector (not shown in this figure).

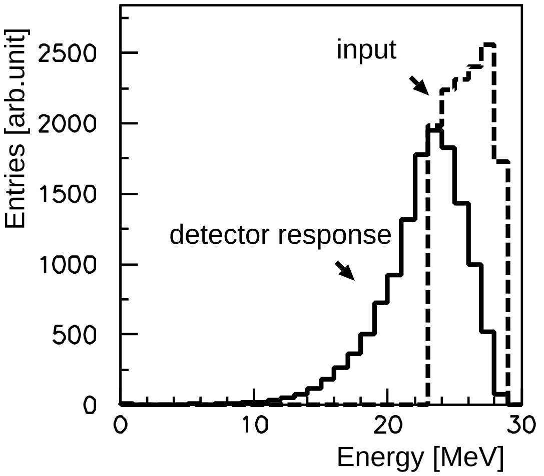

Figure 3.24: Simulation result of the detector response to the Compton scattered photons. The dashed line shows an input energy spectrum while the solid line an actual energy spectrum deposited in the detector. Since most of the events fell in 15 - 25 MeV, we set this range as the signal window.

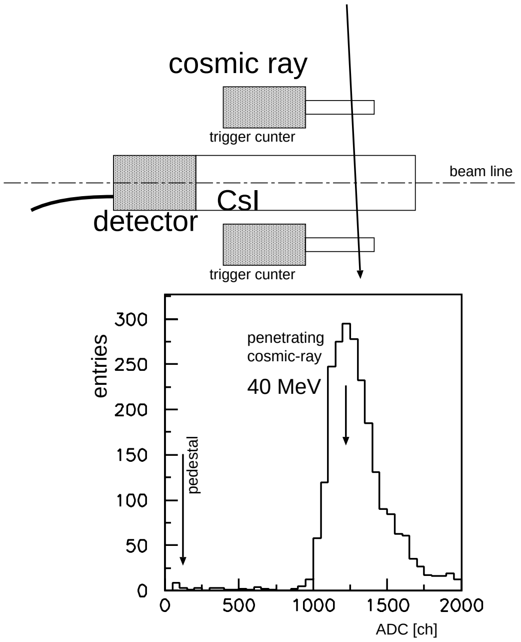

Figure 3.25: Calibration of the detector. The energy calibration was done by measuring the response to the through-passing cosmic rays, which are expected to deposit 40MeV according to the Bethe-Bloch formula. Two small counters are placed up and down side of the detector, and their coincidence is used as a trigger.

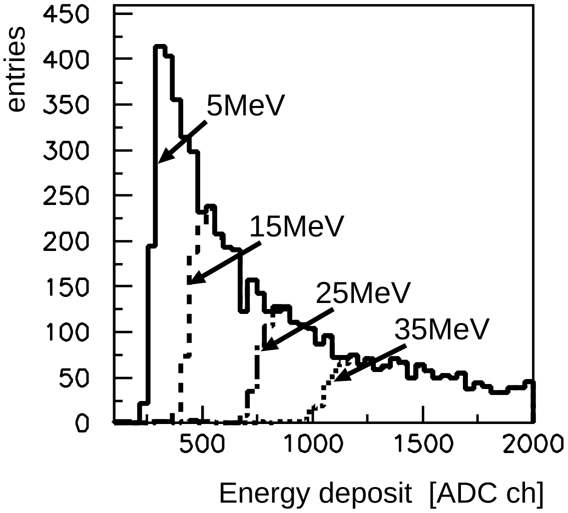

Figure 3.26: Energy spectrum of the background events. The edges are determined by four threshold levels of the discriminator (corresponding to 5, 15, 25 and 35 MeV).

3.3.5 Readout circuits

The signal from the photomultiplier was processed by a series of electronics circuits schematically shown in Figure 3.27. First, the raw signal was amplified and was discriminated with four different threshold levels corresponding to 5, 15, 25 and 35 MeV. Figure 3.26 shows the energy spectrum of the backgrounds; the edges determined by the four thresholds are also shown. The outputs from the discriminators were counted by scalers which were in turn read out via a CAMAC system. Hence, we could count the number of events in four energy bins (A: 5 - 15 MeV, B: 15 - 25 MeV, C: 25 - 35 MeV and D: 35 MeV -). Two sets of scalers were used; one was enabled only when the laser states was “ON” and the other when ”OFF”. The active time of the scalers were monitored by feeding a clock to one channel of the scalers. The scaler data together with beam current data taken by a DCCT, positions of the optical table, etc... were read out every one second.

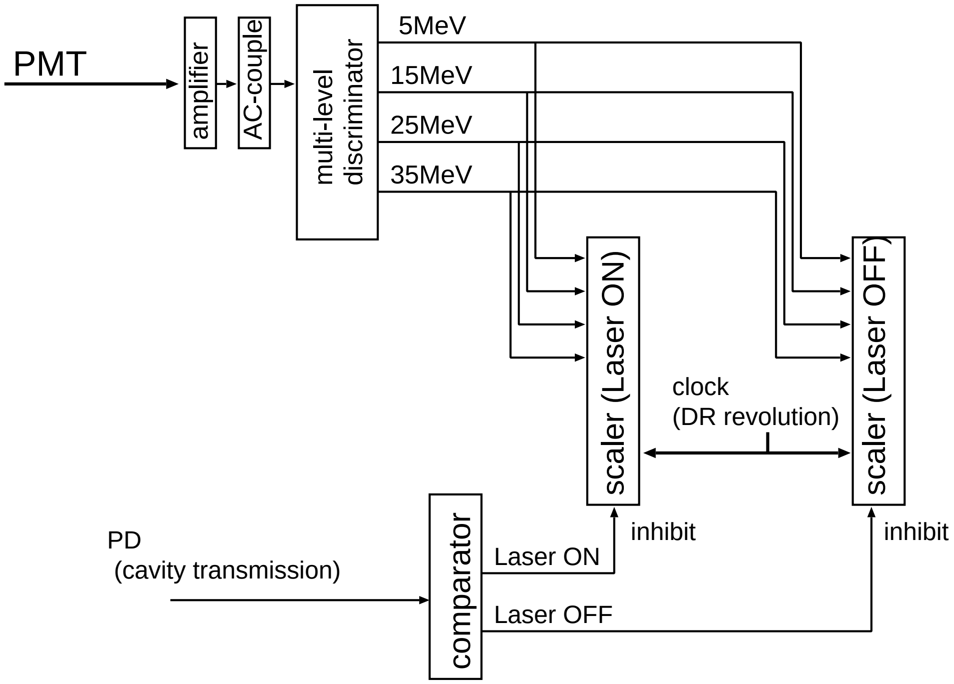

Figure 3.27: Schematic diagram of the readout circuits. A signal from the detector is discriminated with four levels of 5, 15, 25, and 35 MeV, and counted by two scaler modules. The activation of the scalers are automatically controlled by the Laser “ON/OFF” signal which is in turn determined by the photo-diode transmitted signal from the cavity.

3.3.6 Data processing

The scaler count data were first normalized by the active time of the scaler to convert them to count rates (Hz). The contribution of the backgrounds was statistically removed by subtracting the count rate of laser “OFF” case from that of “ON”. Then, the signal rate was normalized by the beam current recorded simultaneously. The current-normalized signal rate (Hz/mA) obtained in the process above was used to plot the beam profile.

3.3.7 Setup procedure of the detector system

Prior to the beam size measurement, the collimator blocks were aligned in a beam-based-way. At first, the laser and electron beam collision was established. Monitoring the count rate both laser “ON” and “OFF”, signal enhancement of laser “ON” was sought by scanning the position of the laserwire. In this step, no collimators was inserted in the beam line. Figure 3.28 shows an example of the count rate profile when the laserwire was placed on the center of the beam position. A $\sim$ D represent the four different energy bins of the discriminator. A clear enhancement of the count rate is seen in the energy bin B , where the Compton signal is expected. Then, alignment procedure of the collimator system started. The 2nd collimator block (the one right in front of the detector) was inserted and aligned by monitoring the energy spectrum (Figure 3.29 and Figure 3.30 show the count rate profiles before and after this procedure.) After that, the 1st collimator was inserted. Figure 3.31 shows a typical count rate profile after all these procedures were completed.

Figure 3.32 and 3.33 are the data when the laserwire was placed at the center of the beam (on beam) and off the beam (off beam), respectively. The data were taken for the beam current up to 2mA, and were classified into 4 energy bins. As can be clearly seen, the laser “ON” data significantly differs only when the laserwire is on the beam (Figure 3.32) and for the energy bin B. Figure 3.34 shows an energy spectrum (the count rate vs 4 energy bins) for the “on beam” and “off beam” cases. As expected, the signal is seen only in the B bin of the “on beam” data.

3.3.8 Scanning and data taking system

One run was defined to be one complete round trip from one position of an electron beam to another, and back to the original position. The scanning was computer controlled and automated. The stepping motors of the table mover were controlled by a computer via GPIB connection. For the vertical scan, the data taking time was 10 second long per point at 10 μm interval. For the horizontal scan, it was 30 second long at every 50 μm. It took about 6 minutes to obtain one profile for the vertical beam size measurement, and 15 minutes for the horizontal.

3.4 Measurement of the beam waist

The laser beam waist is an important parameter in extracting an electron beam size. We developed three different methods to measure this value. They are the beam divergence method, transverse mode difference method and waist scan by an electron beam, and are described below.

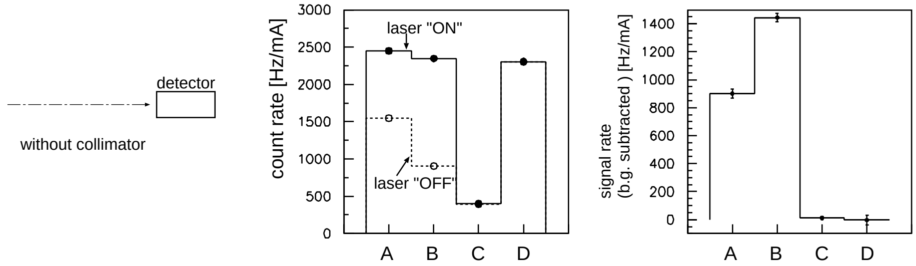

Figure 3.28: Alignment of the collimator system (step 1): In this step, both collimator blocks were out of the beam line. The count rate of the four energy bins for the laser “ON” (solid) and “OFF (dotted)” states (left histogram). The difference of the two states (“ON”−”OFF”) represents the signal rate of the Compton scattering (right histogram).

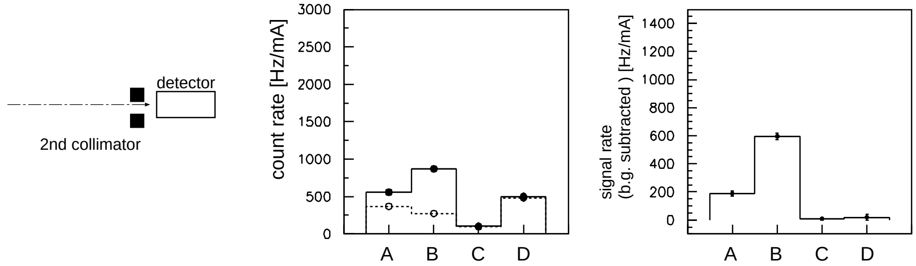

Figure 3.29: Alignment of the collimator system (step 2): A part of the signal is lost when the 2nd collimator is inserted because it is not well aligned yet.

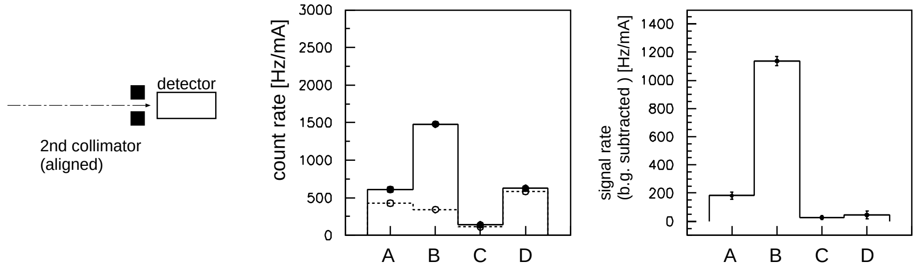

Figure 3.30: Alignment of the collimator system (step 3): The position of the 2nd collimator is adjusted to maximize the signal rate in the energy bin B.

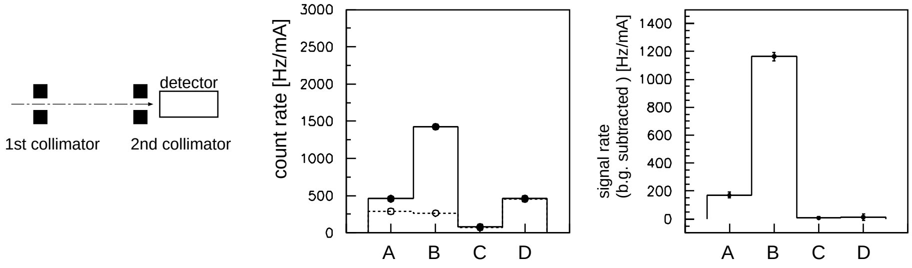

Figure 3.31: Alignment of the collimator system (step 4): The 1st collimator is inserted and aligned.

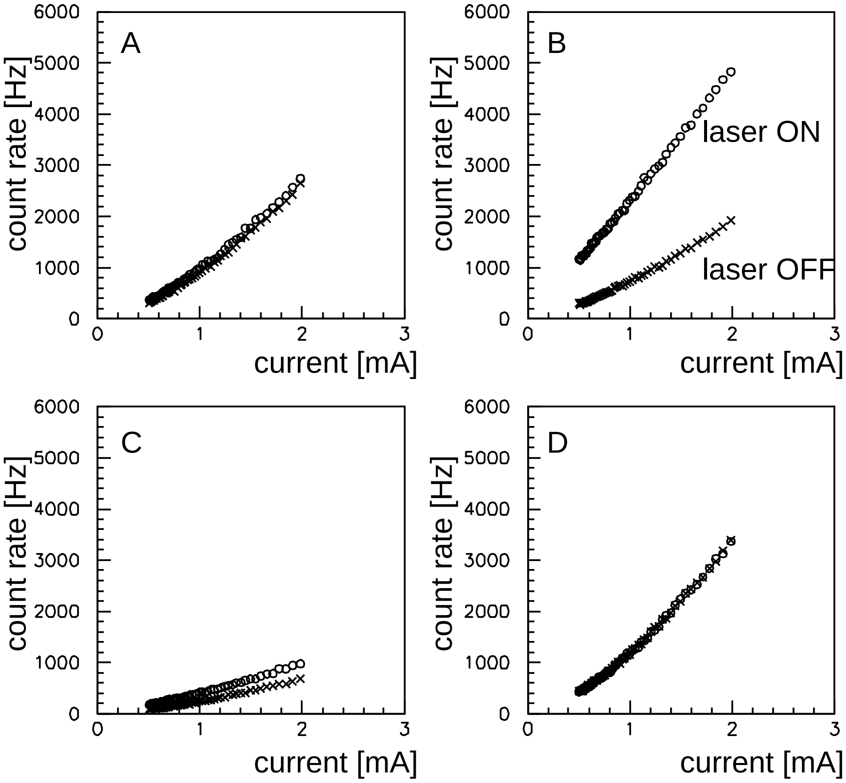

Figure 3.32: Count rates vs the beam current (on beam). The count rates of 4 energy bins (A∼D) are plotted as a function of the beam current.

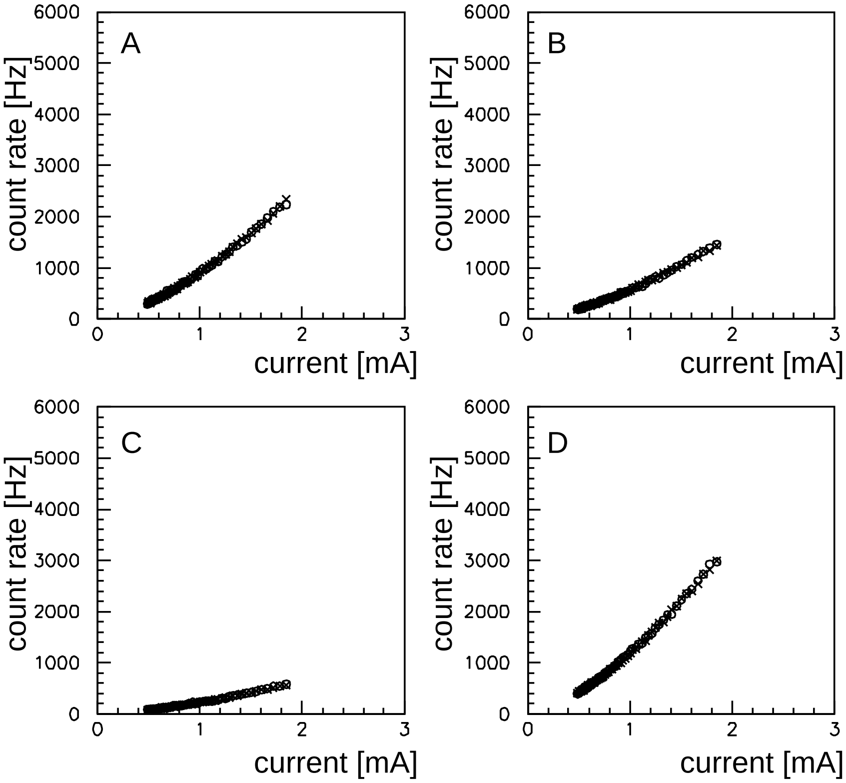

Figure 3.33: Count rates vs the beam current (off beam). The count rates of 4 energy bins (A∼D) are plotted as a function of the beam current.

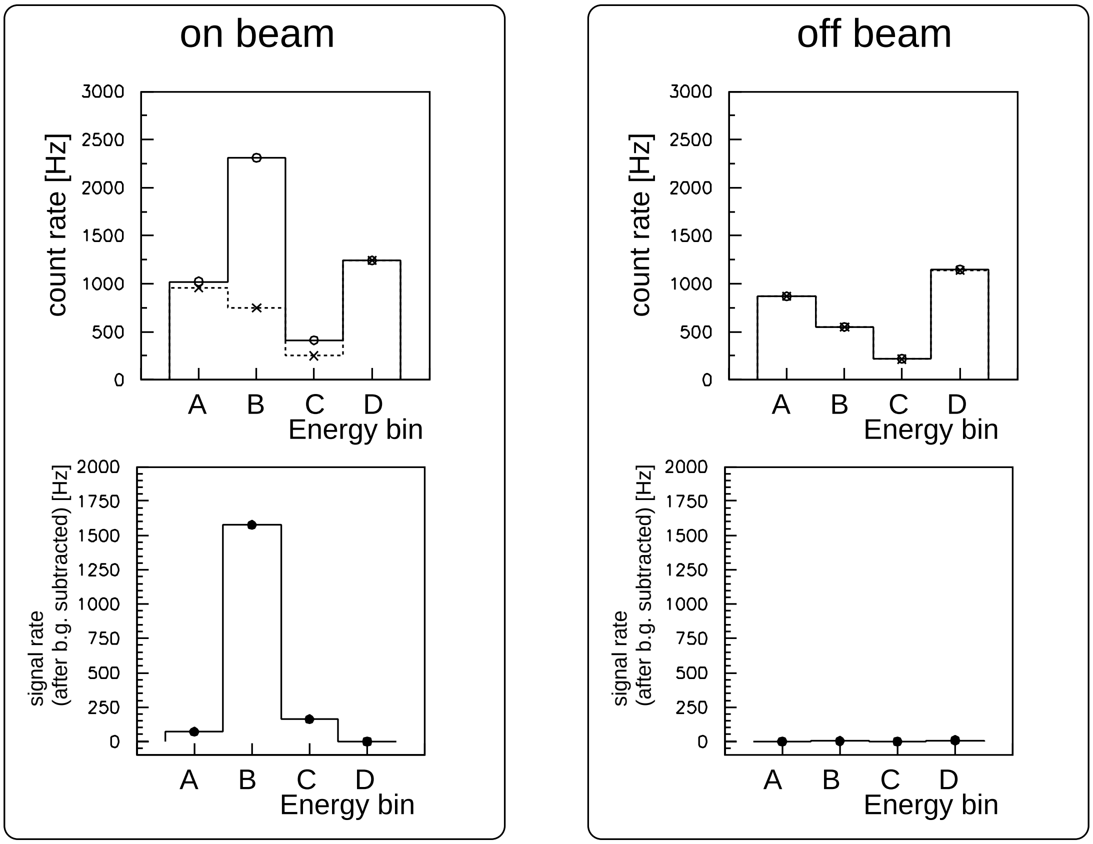

Figure 3.34: Energy spectrum of the signal and background. The count rates are shown for 4 energy bins (A∼D). (left) The count rates taken on the electron beam for the laser "ON" (solid) and "OFF" (dashed) states (upper figure) and the difference of "ON" and "OFF" (lower figure) (right) The same plot taken off the electron beam.

Table 3.2: Summary of the w_0 measurement by the divergence method.

	θ (mrad)	w_0 (μm)	χ^2/ν
horizontal-wire	10.54±0.095(±0.181)	11.37±0.10(±0.19)	14.6/4
vertical-wire	4.20±0.027(±0.067)	29.43±0.19(±0.47)	25.2/4

3.4.1 Beam divergence method

The spot size of a laser beam at the distance z from the focal point (center of the optical cavity) is represented by $w(z) = w_0\sqrt{1+(z/z_0)^2}$, where z_0 $(= \frac{\pi w_0^2}{\lambda})$ is the Rayleigh length. In the case of $z \gg z_0$, the divergence angle (θ_0) can be approximated as

$$\theta_0 \equiv w(z)/z \quad \approx \quad \frac{\lambda}{\pi w_0} \quad . \tag{3.41}$$

Thus the beam waist can be determined by measuring the beam divergence angle (θ_0). Since the rear surface of the cavity mirror is flat, it works as a concave lens. This changes the divergence angle by factor n:

$$\theta = n\theta_0 \quad , \tag{3.42}$$

where n is the index of the mirror substrate, actually n=1.46 for the substrate made of fused silica.

The diverging angle θ was obtained by measuring the spot size of the transmitted laser beam while changing the longitudinal measuring positions. The schematic setup of this measurement is shown in Figure 3.35. The optical cavity was locked to the TEM$_{00}$ mode and the “ON”/”OFF” modulation was not applied during this measurement. The profiles of the laser were measured by a linear image sensor ([32]), a charge-coupled device with 256 cells in a line. The laser profiles were measured at 6 longitudinal positions with a 30-mm step.

The measurement results are shown in Figure 3.36 and 3.37 for the horizontal-wire and the vertical-wire, respectively. Each profile was fitted with a Gaussian function and its width ($\sigma(z)$) was extracted. In fitting the profile, a common error was given for each pixel of the sensor in such a way that the reduced-χ^2 (χ^2/ν) of the fit became unit. The lower plots in Figure 3.36 and 3.37 show the spot size as a function of the longitudinal position. To extract the divergence angle, these data were fitted by a linear function. Table 3.2 summarizes the results of the analysis. The last column is χ^2 of the linear fitting. To include unknown systematic errors, the errors on each spot size were scaled so that χ^2/ν became unit. The errors in parentheses in θ and w_0 are the value after rescaling the error.

The measurement of the horizontal-wire was done after it was installed in the beam line, under a vacuum condition. In contrast, the measurement of the vertical-wire was done at the test bench before the installation.

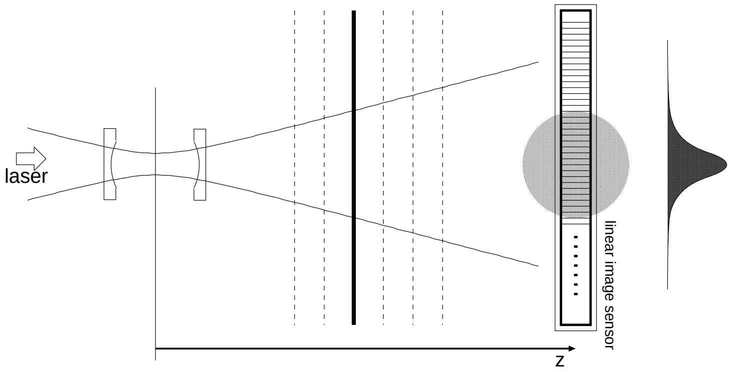

Figure 3.35: Schematic of the beam divergence method. A linear image sensor, placed down stream of the cavity, measures the laser beam profile at several z positions.

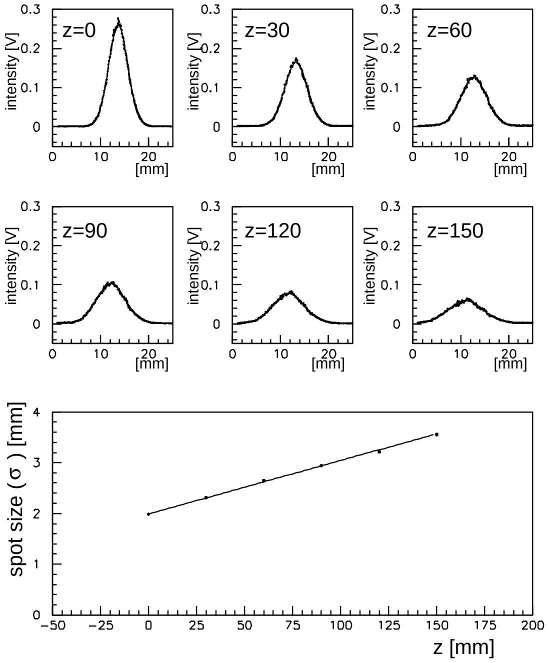

Figure 3.36: Results of the beam divergence method (h-wire). (top) The laser beam profiles at several z positions. (bottom) The laser beam width vs z position. The quantity z in this plot has an arbitrary offset with respect to the cavity center. The relevant quantity is the slope of the linear fit.

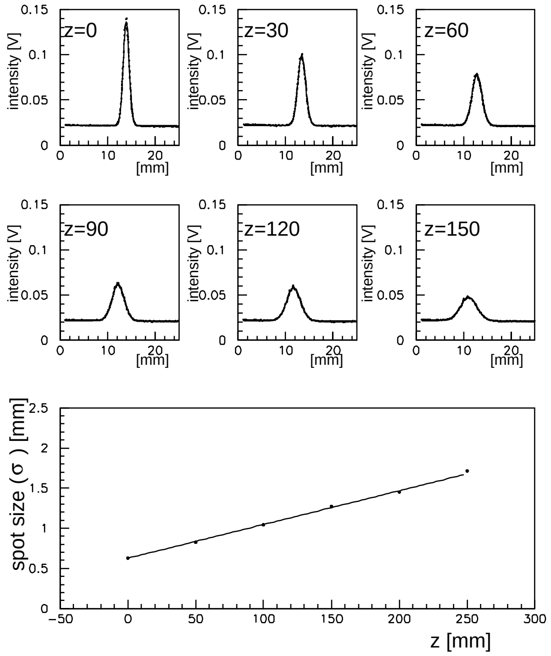

Figure 3.37: Results of the beam divergence method (v-wire). (top) The laser beam profiles at several z positions. (bottom) The laser beam width vs z position. The quantity z in this plot has an arbitrary offset with respect to the cavity center. The relevant quantity is the slope of the linear fit.

3.4.2 Transverse mode difference method

The second method utilizes a property of cavity modes. As written down in Eq.3.38, the additional phase factor (Guoy phase, Φ) depends on the order of the mode $(m+n)$. For this reason, the modes with a different order have a different resonance condition on the cavity length. We can actually observe different resonant peaks with different orders in the sweep mode. Figure 3.38 shows an example of such sweeps; beside the biggest peak corresponding the TEM_{00} mode (0th order), peaks corresponding to TEM_{01} (1st order) and TEM_{02} (2nd order) can be seen.

We now want to determine the cavity length itself from these peaks. Given the cavity length, the difference of the total phase advance of one round trip between two modes arises solely from the Guoy factor. In particular, the difference of the two modes that differ the order by 1 is given, from Eq.3.38, by

$$\begin{align} \Delta\Phi = \Phi(L/2) - \Phi(-L/2) &= \arctan(-L/2z_0) - \arctan(L/2z_0) \tag{3.43}\\ &= \arccos(L/\rho - 1) \quad , \tag{3.44}\end{align}$$

from one mirror to the other. The phase difference $\Delta\Phi$ can be measured experimentally with Figure 3.38. It is easy to show that $\Delta\Phi$ is proportional to ΔL, the difference in the cavity length between the two peaks corresponding to TEM_{00} and TEM_{01}, in Figure 3.38. The actual relation is

$$\Delta\Phi = \pi\frac{\Delta L}{\lambda/2} \tag{3.45}$$

where $\lambda/2$ is the difference between the two TEM_{00} peaks in Figure 3.38. With Eq.3.44 and Eq.3.45, the beam waist is given by

$$\begin{align} w_0^2 = \frac{\lambda}{\pi}\frac{\sqrt{L(2\rho - L)}}{2} &= \frac{\lambda L}{2\pi}\sqrt{\frac{1-(1-L/\rho)}{1+(1-L/\rho)}} \tag{3.46}\\ &= \frac{\lambda L}{2\pi}\sqrt{\frac{1-\cos(\Delta\Phi)}{1+\cos(\Delta\Phi)}} \quad , \tag{3.47}\end{align}$$

where L is the cavity length. This relation is plotted in Figure 3.39.

In our experiment, 6 periods of resonance structure could be seen in the maximum dynamic range of the PZT (Figure 3.40). Among these peaks, we used two peaks at the center (referred to as 3 and 4 in the figure) for the actual analysis. The $\lambda/2$ was defined to be the averaged distance to the adjacent peaks on both sides. We repeated the measurement three times. The value $\frac{\Delta L}{\lambda/2}$ and the calculated result of w_0 are listed in Table 3.3. Averaging these values, we obtained the final value of $w_0 = 11.08 \pm 0.38\ \mu$m., where the error was estimated from the rms fluctuation of the measurements.

3.4.3 Waist scan by an electron beam

The third method for the waist measurement is a direct method which utilizes an electron beam itself. The width of a laser beam changes parabolically along its beam axis. This

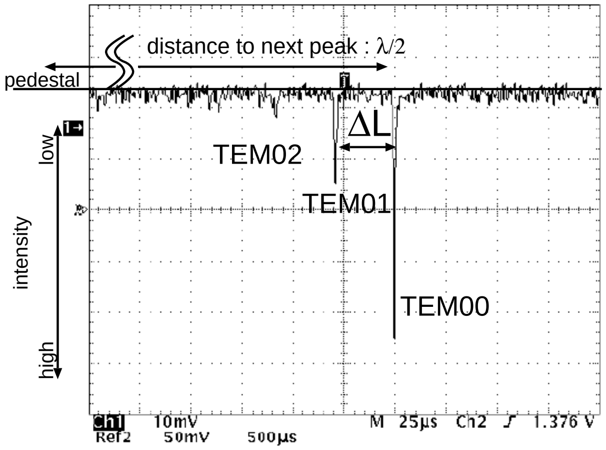

Figure 3.38: Waist measurement by the transverse modes. Several higher-order modes are seen as a peak in the transmittance signal of the sweep mode. The difference ΔL in the cavity length between the TEM$_{00}$ and TEM$_{01}$ peaks is used to determine w_0.

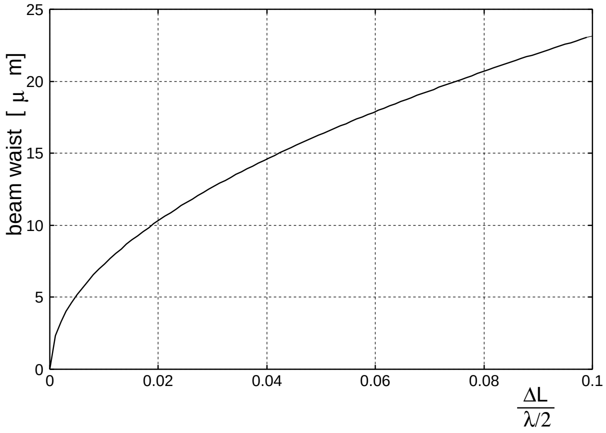

Figure 3.39: The beam waist (w_0) vs $\frac{\Delta L}{\lambda/2}$ for the case of $\rho = 20$mm and $\lambda = 532$nm.

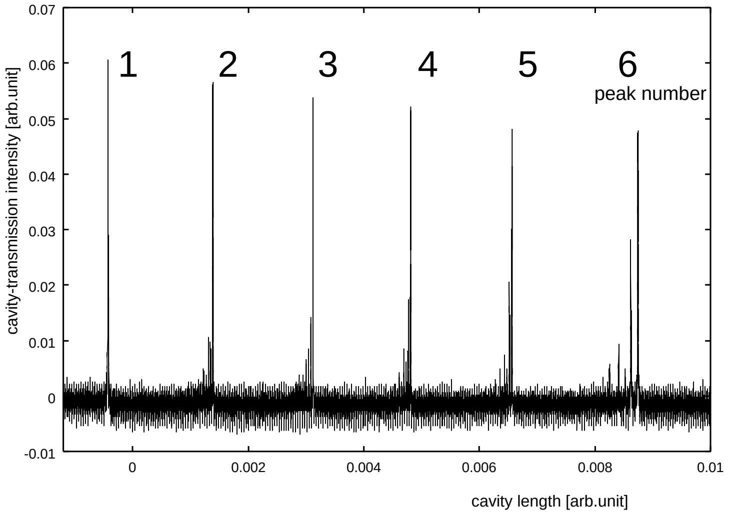

Figure 3.40: Resonance structure observed in the transmittance signal of the sweep mode. There are 6 TEM$_{00}$ peaks seen in the full range of the PZT movement.

Table 3.3: Summary of the w_0 measurements by the transverse mode method

	number 3 peak		number 4 peak	
measurement	$\frac{\Delta \text{Ł}}{\lambda/2}$	w_0 (μm)	$\frac{\Delta \text{Ł}}{\lambda/2}$	w_0 (μm)
1	0.0258	11.72	0.0230	11.07
2	0.0211	10.60	0.0244	11.40
3	0.0221	10.85	0.0222	10.85

dependence is characterized by w_0 (and also by λ). The measured width of the signal profile (σ_{meas}) is a convolution of an electron beam size and a laser beam size, and is expressed by

$$\sigma_{meas} = \sqrt{(\sigma_e)^2 + (w(z)/2)^2} \tag{3.48}$$

$$= \sqrt{(\sigma_e)^2 + \left(\frac{w_0}{2}\right)^2 \left(1 + \left(\frac{\lambda z}{\pi w_0^2}\right)^2\right)} \quad . \tag{3.49}$$

Here z represents the location along the cavity axis. We carried out vertical scans changing horizontal position of the horizontal laserwire. The electron beam size was assumed to remain same during these scans. Figure 3.41 shows the measured width as a function of the horizontal position (z in Eq.(3.49)) of the laserwire. (See the next chapter for the detail of the analysis procedure.) We fitted these data to Eq. 3.49 with three free parameters (σ_e, w_0 and the offset of z), and obtained the solid curve shown in Figure 3.41. We could determine in this way the laser beam waist w_0 experimentally.

We carried out this kind of measurements 8 times in the time span of more than 4 months. These results are summarized in Figure 3.42. The electron beam sizes varied from one measurement to another due to different beam tuning, but the obtained laser waists agreed well with each other, proving that w_0 remained same during this period. The combined result is

$$w_0 = 11.27 \pm 0.29 \quad (\mu\text{m}) \quad . \tag{3.50}$$

The electron beam should be scanned at the most focused part of the laserwire. The results of this measurement experimentally determines the minimum position. Thus this measurement was regularly done prior to the vertical beam size measurement.

3.4.4 Summary of the beam waist measurement

The vertical wire was measured only by the divergence method. The result was $w_0 = 29.43 \pm 0.47$ μm. ($\sigma_{lw} = 14.7 \pm 0.2$ μm.) The horizontal wire was measured by three methods. They were summarized in Figure 3.43, and were consistent with each other. The averaged result was $w_0 = 11.30 \pm 0.16$ μm. ($\sigma_{lw} = 5.65 \pm 0.08$ μm.)

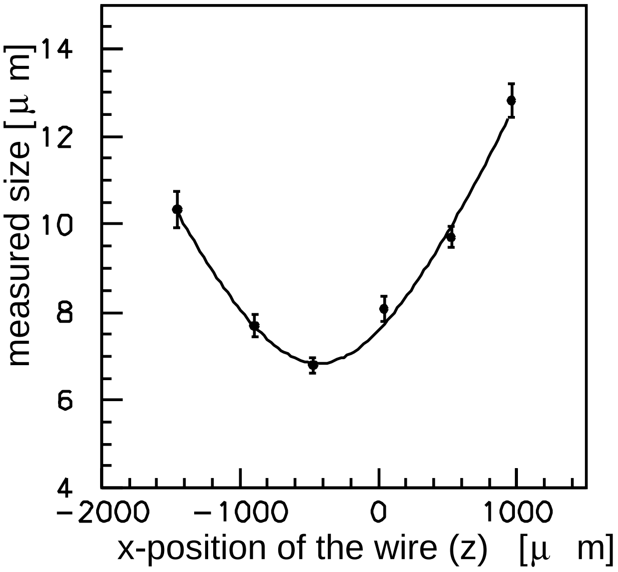

Figure 3.41: Results of the beam waist scan. Vertical scans were carried out changing the horizontal position of the horizontal laserwire. The solid line is the fitting result by the function of Eq.3.49.

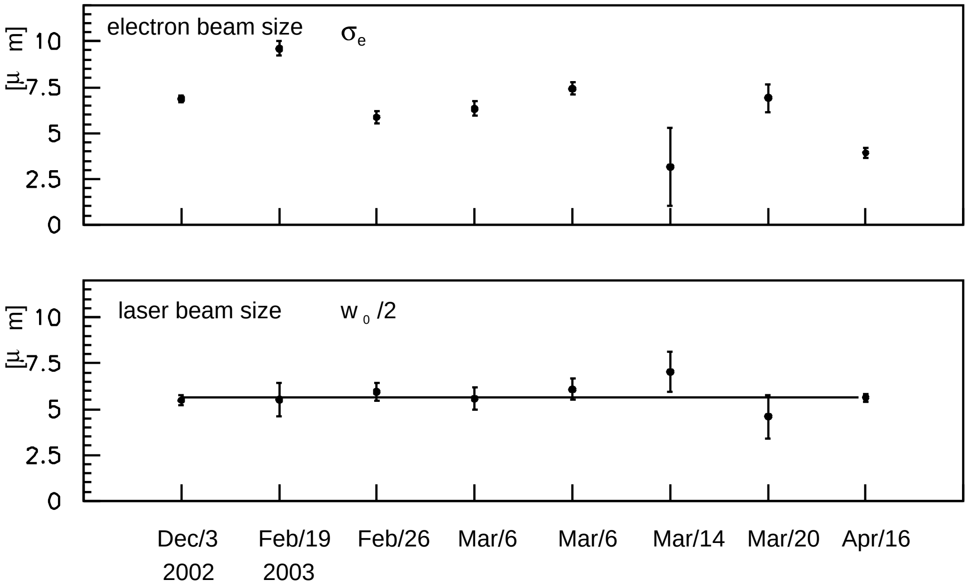

Figure 3.42: Fitting result of σ_e and $w_0/2$. The electron beam size (top), and the laser beam size ($w_0/2$) (bottom) were measured over the time period of 4 months. The laser waist remained same during this period.

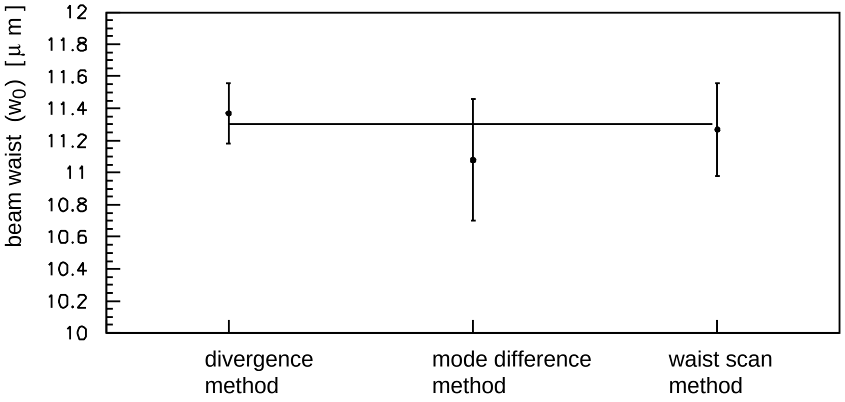

Figure 3.43: Comparison of the beam waist measurements by three methods.

Chapter 4

Experiments with a Single-Bunch Beam

We performed a series of emittance measurements with a single bunch beam stored in the damping ring over the time period of four months from February 2003 to May 2003 ([33]). Although the goal of the ATF damping ring is to confirm realization of the target emittance with a multi-bunch beam, verification with a single-bunch beam is the first important step to be done. Also a single bunch beam is suitable for studying basic beam dynamics such as intra-beam scattering, which are not related to the coupled-bunch motion.

The main purposes of this experiment were :

1. Verification of a stable production of a low emittance beam satisfying the requirements of the linear colliders.
2. Observation of possible emittance dilution which depends on the beam intensity under various beam conditions, and understanding the mechanisms of the emittance growth.

4.1 Introduction

4.1.1 Emittance measurements prior to this experiment

First, we give a short review of the results of emittance studies at the moment we started this experiment ([34]).

As the first step after the ATF commissioning, an extracted beam was examined by the solid-wire scanner system ([35]). The production of a small emittance, 1.37 ± 0.03 nm·rad, in the horizontal plane at the bunch intensity of 3-5$\times 10^9$ electrons was confirmed. This should be compared with the expected value of 1.27-1.34 nm·rad which included the effect of intra-beam scattering to the designed natural emittance of 1.07 nm·rad. The result was a good verification of the ring design.

Then the next step was to measure the vertical emittance. The target value for the vertical emittance was 1% of the horizontal one. The smallness of the vertical emittance posed a number of difficulties for the measurement system. In the extraction line, it was not easy to stabilize the beam orbit within a fraction of the vertical beam size. It was also not straightforward to estimate actual emittances from measured values. This was because, in the diagnostic section of the extraction line, even a small amount of the residual dispersion could mimic an apparent (false) vertical beam size. A technique for the precision measurement of the dispersion effect and its correction had to be developed for an accurate measurement. Another difficulty was the x-y coupling. Some unknown coupling source could give a small tilt in the transverse beam profile. Due to the high aspect ratio of the beam profile, the vertical size could easily be contaminated by the much bigger horizontal sizes. We struggled to find out the hidden coupling sources and/or to correct them by introducing additional skew magnets.

Systematic studies of the emittance in the extraction line were continued from April 2000 to June 2001 ([36],[37]). From the studies, the vertical emittance was found to be 15 pm·rad for low intensity and to grow to 23 pm·rad at the beam intensity of 8×10^9 electrons per bunch. This outcome gave rise to puzzles as well as interests ([38]); the intensity dependence of the vertical emittance was surprisingly strong, and could not be reproduced by the standard calculation involving the intra-beam scattering, which explained well the horizontal intensity dependence. Various scenarios were considered to explain the observation; for example, possibilities to require a modification in the intra-beam scattering model, and/or existence of other intensity dependent effects in the vertical plane. However, considering the measurement difficulties mentioned above, it was concluded that there might be still unknown measurement errors, and they were the most likely source of the disagreement. At the same time, the importance of the measurement in the ring itself was stressed.

As for the measurement in the ring, we had been developing the SR interferometer monitor since the beginning of the ring operation. This monitor worked well for a large beam size. However, its practical resolution limit was found to be around 10 μm. The system was not understood well enough for such a small vertical size of our interest.

The commissioning of the laserwire monitor started in May 2000. The first vertical emittance measurement was carried out in December 2000 [39], and it resulted (11.8 ± 0.8) pm·rad as the average of all the data points. No clear dependence on the beam intensity was observed within the measurement errors dominated by the statistical fluctuation.

The results in the extraction line (by the solid-wire scanner) and in the ring (by the laserwire and SR monitor) at this moment are plotted in Figure 4.1.

4.1.2 Improvements to the ATF damping ring

To settle the issue on the current dependence of the vertical emittance, we focused our efforts to accurate measurements in the ring: upgrade of the laserwire. At the same time, various efforts were made to reduce the emittance further. We first describe several essential improvements to the ATF damping ring itself. They are as follows:

1. The read-out circuits for the beam position monitors (BPMs) in the damping ring were replaced by a new type. Their position resolution was, thereby, improved from

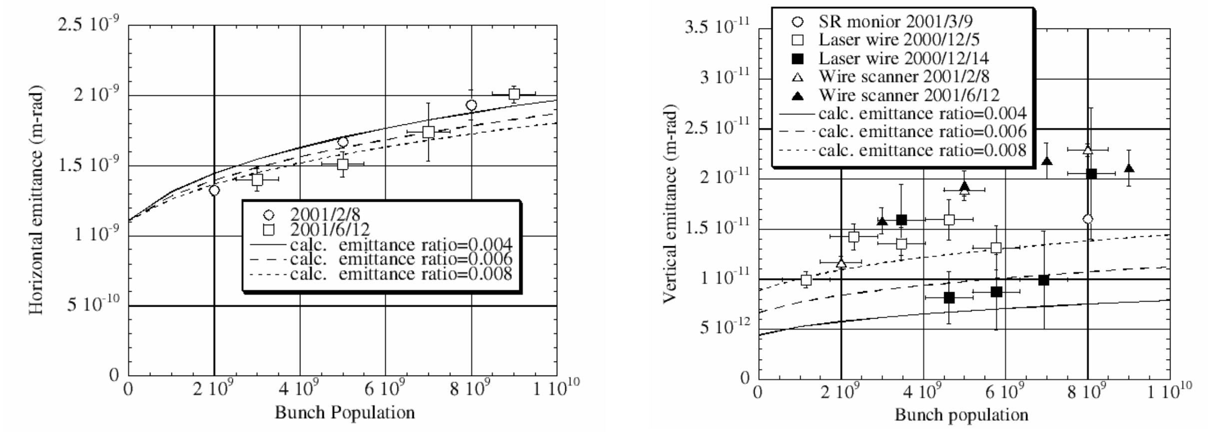

Figure 4.1: Single bunch emittance data of the 2000-2001 runs: Horizontal (left) and vertical (right) emittance data measured by three different monitors are plotted as a function of bunch intensity. The lines are the results of a model calculation involving the intra-beam scattering; the x-y coupling of 0.004, 0.006 and 0.008 is assumed.

20 μm to 2 μm.

2. Since 2003, the orbit measurement for damping ring tuning has been done in a storage mode. In this mode, the beam extraction and re-fill process are stopped to store the same beam pulse in a long time. It made the beam intensity stable during the measurement, and the stability of BPM reading was greatly improved.

3. The position offsets of the BPMs with respect to the field center of the nearest magnet were measured by a beam-based method. (See Sec.2.3.2.)

4. The positions of most of the magnets in the damping ring were re-aligned and also measured in a beam based way. (See Sec.2.3.2.)

5. The optics were further refined. The improvement became possible by the upgraded sensitivity of BPMs. The strength of each quadrupole magnet is determined in a beam based way. Measuring the amount of the kick received in the magnet while steering the beam orbit by corrector magnets, the strength of the magnet was precisely determined.

As to the laserwire, several improvements were made as already described in Chapter 3. They are summarized as follows.

1. Two laserwire systems were installed, which measure both the vertical and the horizontal beam size.

2. The width of the horizontal wire was reduced so that it could measure smaller electron beams.

3. The effective laser power was increased by about one order of magnitude to shorten the data acquisition time.

Table 4.1: List of ring conditions for runs A∼F

		status of skew correctors		
date	run	SD series	SF series	comment
2/26	A	ON	ON	reference run
4/16	B	ON	ON	low emittance tuning
5/15	C	ON	OFF	
5/20	D	ON	ON	low emittance tuning (reproducibility)
5/23 (1)	E	OFF	REVERSE	
5/23 (2)	F	OFF	OFF	

4.2 Procedure of the experiment

In order to study beam dynamics such as the effects of intra-beam scattering, it is important to know all three dimensional beam properties in the same beam condition. The following items were simultaneously measured for a given beam condition:

- The horizontal and vertical emittance (by the laserwire).
- The bunch length (by the streak camera).
- The momentum spread (by the screen monitor in the extraction line).

In this chapter, one run was defined to be a complete set of these measurements in one fixed condition of the ring. Since we were interested not only in the achievement of the smallest emittance but also in the collective effects and their dependence on the bunch volume, some runs were taken under beam conditions intentionally worsened (*e.g.* large vertical emittance).

4.2.1 Beam tuning and damping ring conditions

As already stated, the vertical emittance expected to be determined predominantly by x-y coupling. All sextupole magnets in the arc sections of the damping ring had trim windings which were designed to produce a skew quadrupole component (see Sec.2.3.3.). Each trim coil was controlled independently so as to correct the local x-y coupling. For certain runs, we intentionally turned off or excited them with the reversed current flow to enlarge the vertical emittance. There are two families of sextupole magnets, SD and SF series for different polarities; the conditions of their trim coils for each run are listed in Table 4.1.

Before each run (except for run A), we carried the standard emittance-tuning procedure and made the initial ring condition almost the same for all runs. The detail of this procedure was already explained in Sec. 2.3.3. In run C,E and F, we then enlarged the vertical emittance as stated.

4.2.2 Measurements of transverse beam profiles

One of the main goals of the study is to clearify the intensity dependence of the emittances. We thus made the measurements up to the maximum possible intensity. Actually, there existed typically 9 scans in a run with each scan being for a certain intensity region. Although the scanning and data acquisition were automated for the most part, beam injection into the damping ring and intensity control had to be done manually.

Data taking

As we stressed, the electron beam intensity was one of the most important parameters. For each scan, we defined the intensity to be measured (we call it intended intensity region). To realize it, the emission of the electron gun was tuned, and the injected beam intensity was made to agree with the maximum of the intended intensity region. After the beam was stored in the ring, the scanning process was started. One scan was defined to be one complete round trip measuring an entire electron profile. Typical data taking procedures are shown in Figure 4.2∼4.3; the beam current, the position of the laserwire and the measured signal rate are plotted as a function of the data-acquisition time. During the measurement, the electron beam current decreased according to its life time. When the current reached the minimum of the intended intensity region, the data taking was manually paused to re-fill an electron beam and then it was resumed. Thus data of one scan contained several fills, especially in the data of a high intensity region. Since the damping time of the ring was around 20 msec, the stored beam immediately reached the equilibrium. We assumed that the multiple fills had no effect on our measurement. It took about 6 minutes for a vertical scan, and 15 minutes for horizontal. The beam-intensity region, required number of fills and total number of data points for each scan are listed in Table 4.2∼4.7. The average beam current during the scan and its rms variation are also listed. We used these values as the average and its interval of the intended intensity region.

Fitting of the signal profile

The first step of the analysis is to plot the signal profile. The current-normalized signal rate (Hz/mA) was calculated, and was plotted as a function of the laserwire position. Figure 4.4 and 4.5 are examples of such measurements for vertical and horizontal directions. We fitted these data points by a Gauss function with three free parameters (peak height, position and width). We defined the width of the fitted Gauss function as the measured peak width (σ_{meas}). The resultant σ_{meas} values are listed in the last column but one in Table 4.2∼4.7. The chi-square (χ^2) per degree of freedom (ν) of the fit is also listed. The value of χ^2/ν larger than unity indicates existence of some systematic effects. It has been observed that there exists a slow beam orbit drift in a few 100 seconds time scale. Since the vertical beam size was as small as 5 μm, even orbit drift of 1 μm order (much less than the measurement accuracy of the BPMs) could affect the measurement. We suspect a temperature change in some component of the ring caused this drift. In any case, to include the effect of the systematic effects, we took a conservative way. Namely,

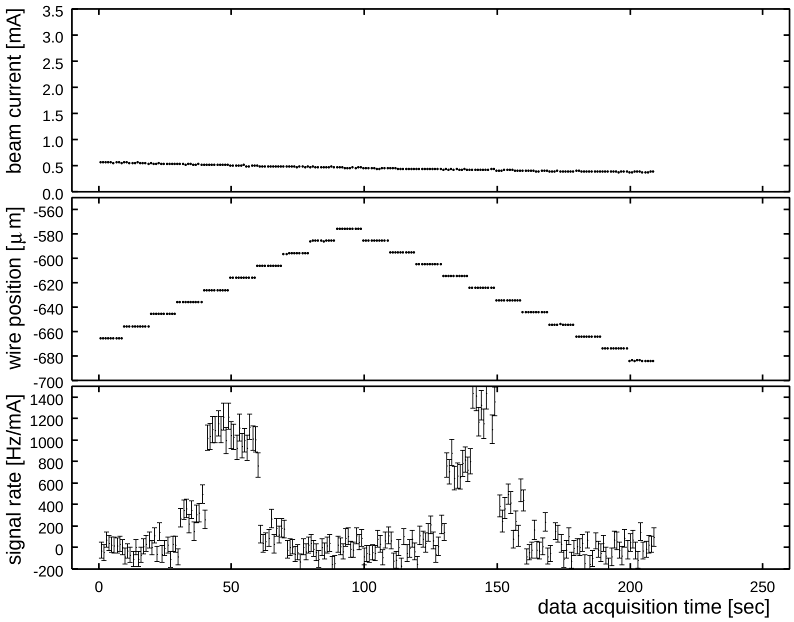

Figure 4.2: Example of the scan procedure (low intensity case) [scan y4 in run B]. The beam current (top), the position of the laserwire (middle) and the current-normalized signal rate (bottom) are plotted as a function of the data-acquisition time. In this measurement, the intended intensity region was defined to be 0.55∼0.35 mA. Only one fill was needed to complete the scan thanks to the gradual decrease in the beam current.

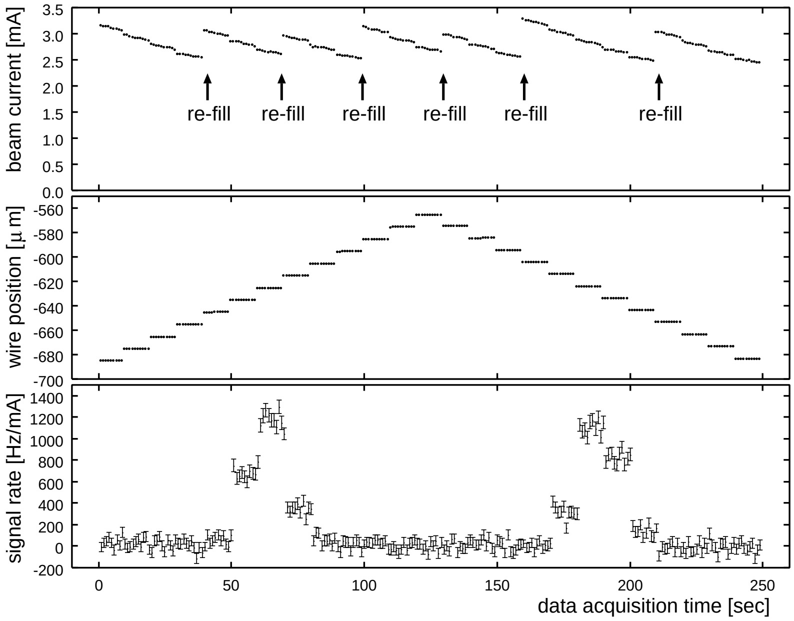

Figure 4.3: Example of the scan procedure (high current case) [data take y1 in run B]. Same plot as Figure 4.2. In this measurement, the intended intensity region was defined to be 3.2∼2.5 mA. Seven fills were required in this region.

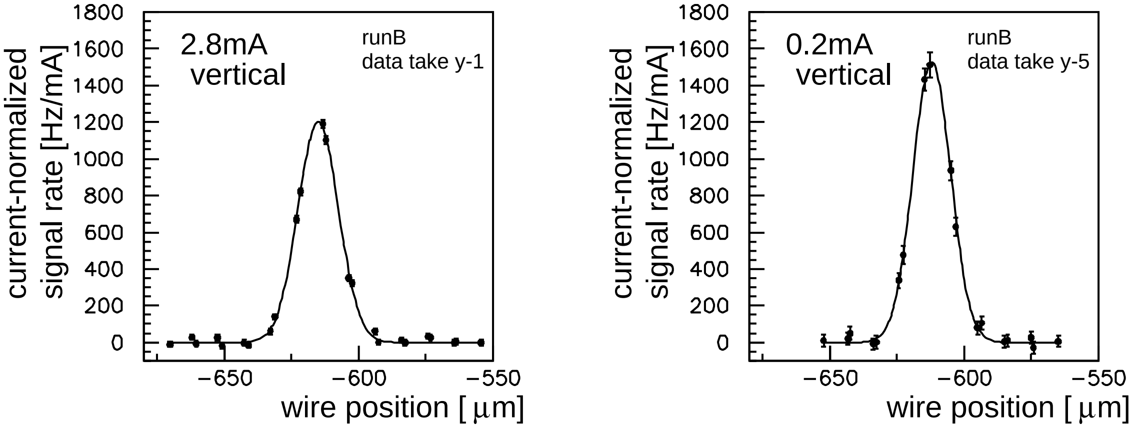

Figure 4.4: Example of the measured profile and the fit result (vertical scan): The signal count rate normalized to the electron beam current (Hz/mA) is plotted as a function of the laserwire position. The solid line is a fit result by a Gauss function. The actual data are y1 in run B, an example for the high current case (left) and y5 in run B for the low current case (right).

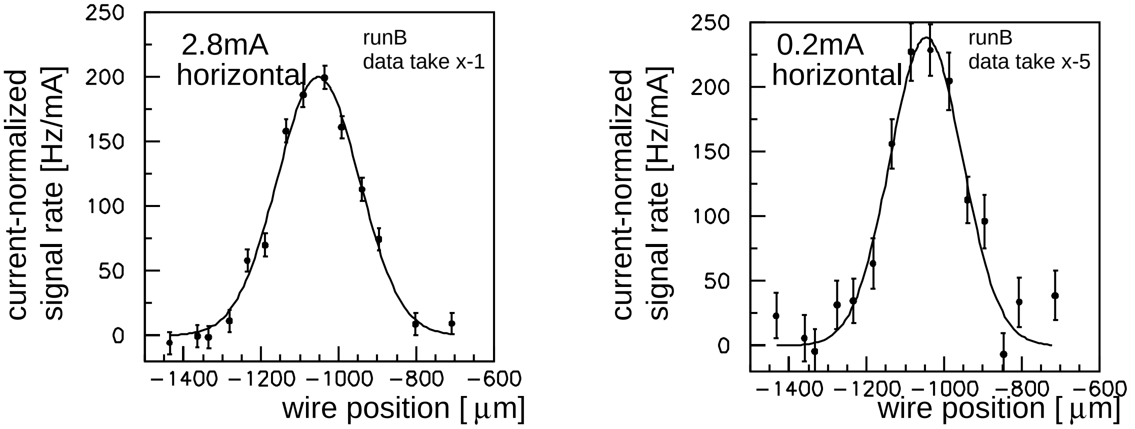

Figure 4.5: Example of the measured profile and the fit result (horizontal scan): The signal count rate normalized to the electron beam current (Hz/mA) is plotted as a function of the laserwire position. The solid line is a fit result by a Gauss function. The actual data are x1 in run B, an example for the high current case (left) and x5 in run B for the low current case (right).

we enlarged the errors of all data points uniformly so that χ^2/ν of the fitting became unit. The enlarged errors on σ_{meas} are listed in the parentheses. We employed these values in the following analysis.

Table 4.2: Scan list (run A)

	intended intensity region (mA)	intensity (mA) average±rms	total fill	total step	peak width σ_{meas} (μm)	χ^2/ν
y 1	$3.8 \sim 3.2$	3.43 ± 0.50	14	44	8.68 ± 0.05 ($\pm$ 0.19)	16.7
2	$3.1 \sim 2.2$	2.67 ± 0.26	9	51	9.58 ± 0.05 ($\pm$ 0.21)	16.7
3	$2.0 \sim 1.4$	1.67 ± 0.20	4	43	8.38 ± 0.06 ($\pm$ 0.11)	3.9
4	$1.0 \sim 0.6$	0.81 ± 0.12	2	40	8.06 ± 0.07 ($\pm$ 0.20)	9.3
5	$0.60 \sim 0.3$	0.45 ± 0.07	1	40	8.04 ± 0.08 ($\pm$ 0.27)	11.2
6	$0.23 \sim 0.17$	0.19 ± 0.02	1	35	8.05 ± 0.11 ($\pm$ 0.25)	5.2
7	$3.0 \sim 1.1$	2.57 ± 0.26	6	36	8.63 ± 0.05 ($\pm$ 0.12)	6.3
8	$3.7 \sim 3.2$	3.44 ± 0.23	11	35	8.63 ± 0.05 ($\pm$ 0.23)	25.1
x 1	$3.7 \sim 3.0$	3.27 ± 0.65	15	18	113.2 ± 2.4	1.3
2	$2.9 \sim 2.3$	2.56 ± 0.21	9	19	108.0 ± 2.4	0.6
3	$2.0 \sim 1.3$	1.62 ± 0.21	4	20	106.2 ± 2.4	0.4
4	$1.2 \sim 0.7$	0.94 ± 0.15	2	20	96.7 ± 2.4	1.2
5	$0.50 \sim 0.30$	0.36 ± 0.05	1	20	97.8 ± 3.6	1.0

4.2.3 Measurement of dispersion function at the collision points of laserwires

Electrons in a ring oscillate in the transverse direction around the center-orbit (betatron oscillation). The dispersion of the beam line introduces an energy dependent change in the orbit;

$$\Delta x(y) = \eta_{x(y)} \frac{\Delta p}{p} \quad , \tag{4.1}$$

where $\eta_{x(y)}$ is the dispersion function of $x(y)$ plane, p the nominal momentum, and Δp the actual momentum with respect to p. Thus the energy spread of the beam can contribute to the beam size through the dispersion term as

$$\sigma = \sqrt{\beta\epsilon + \left(\eta \frac{\Delta p}{p}\right)^2} \quad . \tag{4.2}$$

We estimated the dispersion functions at the collision points of the laserwire by measuring the response of the beam center position to the slight energy change. The beam energy in the damping ring is proportional to the frequency of the RF cavity;

$$\frac{\Delta p}{p} = \frac{1}{\alpha_M} \frac{\Delta f}{f_{RF}} \tag{4.3}$$

Table 4.3: Scan list (run B)

	intended intensity region (mA)	intensity (mA) average±rms	total fill	total step	peak width σ_{meas} (μm)	χ^2/ν
y 1	3.2 ∼ 2.5	2.80 ± 0.20	7	25	7.53 ± 0.09 (± 0.12)	1.7
2	2.3 ∼ 1.6	1.89 ± 0.20	4	24	7.72 ± 0.12 (± 0.17)	2.3
3	1.1 ∼ 0.7	0.89 ± 0.12	2	22	7.29 ± 0.12 (± 0.15)	1.5
4	0.55 ∼ 0.35	0.44 ± 0.06	1	21	7.39 ± 0.16 (± 0.21)	1.7
5	0.25 ∼ 0.18	0.21 ± 0.02	1	19	7.01 ± 0.19	0.6
6	0.55 ∼ 0.35	0.43 ± 0.06	1	20	7.18 ± 0.15 (± 0.24)	2.3
7	1.1 ∼ 0.7	0.92 ± 0.14	2	21	7.33 ± 0.12 (± 0.14)	1.3
8	2.2 ∼ 1.7	1.90 ± 0.17	4	21	7.14 ± 0.09 (± 0.12)	1.7
9	3.2 ∼ 2.5	2.82 ± 0.19	7	25	7.84 ± 0.09 (± 0.12)	1.8
x 1	3.2 ∼ 2.6	2.88 ± 0.20	15	15	105.8 ± 3.5 (± 3.8)	1.1
2	2.1 ∼ 1.6	1.85 ± 0.16	14	14	105.5 ± 3.9 (± 4.3)	1.2
3	1.1 ∼ 0.8	0.93 ± 0.08	4	14	105.5 ± 4.5	0.5
4	0.55 ∼ 0.35	0.42 ± 0.05	2	16	95.6 ± 4.6 (± 6.0)	1.7
5	0.32 ∼ 0.18	0.24 ± 0.04	1	16	93.3 ± 5.8 (± 6.8)	1.4
6	0.55 ∼ 0.36	0.45 ± 0.05	2	16	92.8 ± 4.3 (± 6.7)	2.4
7	1.1 ∼ 0.8	0.93 ± 0.11	4	16	99.4 ± 3.8 (± 4.1)	1.2
8	2.2 ∼ 1.6	1.86 ± 0.15	8	18	107.1 ± 3.7	0.4
9	3.0 ∼ 2.3	2.67 ± 0.21	9	16	113.1 ± 3.6	0.7

Table 4.4: Scan list (run C)

	intended intensity region (mA)	intensity (mA) average±rms	total fill	total step	peak width σ_{meas} (μm)	χ^2/ν
y 1	3.6 ∼ 2.9	3.28 ± 0.25	8	25	12.61 ± 0.24 (± 0.26)	1.3
2	2.4 ∼ 1.9	2.17 ± 0.15	6	25	11.55 ± 0.24	1.0
3	1.3 ∼ 0.9	1.05 ± 0.13	3	23	11.35 ± 0.28	0.8
4	0.55 ∼ 0.44	0.49 ± 0.04	2	22	11.42 ± 0.30 (± 0.36)	1.5
5	0.20 ∼ 0.15	0.17 ± 0.01	1	22	9.43 ± 0.40 (± 0.55)	1.9
6	0.52 ∼ 0.42	0.46 ± 0.03	2	21	10.85 ± 0.33	0.7
7	1.5 ∼ 1.2	1.35 ± 0.12	4	24	10.95 ± 0.24	0.7
8	2.4 ∼ 1.9	2.20 ± 0.17	5	21	11.48 ± 0.24 (± 0.26)	1.3
9	3.5 ∼ 2.8	3.15 ± 0.20	8	24	12.25 ± 0.25 (± 0.26)	1.1
x 1	3.6 ∼ 2.6	3.09 ± 0.26	8	14	109.0 ± 4.1	1.0
2	2.6 ∼ 1.8	2.21 ± 0.22	6	14	107.1 ± 4.1	0.8
3	1.5 ∼ 1.1	1.26 ± 0.14	4	15	102.6 ± 4.3	0.9
4	0.60 ∼ 0.40	0.48 ± 0.06	2	16	97.6 ± 5.2	0.7
5	0.22 ∼ 0.14	0.17 ± 0.02	1	18	89.0 ± 6.4	1.0
6	0.55 ∼ 0.35	0.44 ± 0.06	2	16	97.5 ± 6.1	1.5
7	1.5 ∼ 0.9	1.21 ± 0.19	3	16	97.5 ± 6.1	1.5
8	2.5 ∼ 1.9	2.18 ± 0.21	7	16	108.5 ± 4.8	1.5
9	3.4 ∼ 2.6	2.98 ± 0.28	8	16	107.6 ± 4.3	0.7

Table 4.5: Scan list (run D)

	intended intensity region (mA)	intensity (mA) average±rms	total fill	total step	peak width σ_{meas} (μm)	χ^2/ν
y 1	0.25 ∼ 0.20	0.22 ± 0.01	1	15	7.35 ± 0.22	1.0
2	0.62 ∼ 0.46	0.53 ± 0.05	1	16	7.21 ± 0.16	0.7
3	1.5 ∼ 1.0	1.20 ± 0.14	1	15	6.73 ± 0.11	0.8
4	2.5 ∼ 1.9	2.18 ± 0.20	2	17	7.02 ± 0.09	0.6
5	3.6 ∼ 2.6	3.05 ± 0.30	2	19	7.21 ± 0.08 (± 0.09)	1.3
6	2.6 ∼ 1.7	2.10 ± 0.23	2	21	7.06 ± 0.09 (± 0.12)	1.8
7	1.35 ∼ 1.0	1.17 ± 0.10	1	18	6.94 ± 0.10 (± 0.11)	1.3
8	0.70 ∼ 0.50	0.59 ± 0.05	1	16	6.85 ± 0.14 (± 0.17)	1.3
9	0.28 ∼ 0.21	0.24 ± 0.02	1	19	6.87 ± 0.19 (± 0.21)	1.1
x 1	2.8 ∼ 1.8	2.20 ± 0.25	9	17	110.5 ± 4.4	1.8
2	1.6 ∼ 0.9	1.20 ± 0.22	4	17	103.7 ± 5.1	0.8
3	0.50 ∼ 0.30	0.41 ± 0.06	2	15	93.9 ± 5.7	1.3

Table 4.6: Scan list (run E)

	intended intensity region (mA)	intensity (mA) average±rms	total fill	total step	peak width σ_{meas} (μm)	χ^2/ν
y 1	3.4 ∼ 2.4	2.88 ± 0.30	7	26	20.11 ± 0.73	1.0
2	2.6 ∼ 1.9	2.24 ± 0.22	6	21	19.39 ± 0.68	0.9
3	1.7 ∼ 0.9	1.23 ± 0.22	2	21	19.72 ± 0.81	1.5
4	0.6 ∼ 0.4	0.50 ± 0.06	2	23	17.98 ± 0.86	1.6
5	0.27 ∼ 0.19	0.22 ± 0.02	1	19	18.85 ± 1.17	1.2
x 1	3.4 ∼ 2.6	3.01 ± 0.24	12	15	100.6 ± 2.9	1.1
2	2.7 ∼ 1.9	2.29 ± 0.20	9	16	103.4 ± 3.4	0.9
3	1.6 ∼ 0.8	1.12 ± 0.22	2	14	94.1 ± 3.3	0.7
4	0.70 ∼ 0.40	0.56 ± 0.08	2	16	94.3 ± 3.8	1.5

Table 4.7: Scan list (run F)

	intended intensity region (mA)	intensity (mA) average±rms	total fill	total step	peak width σ_{meas} (μm)	χ^2/ν
y 1	3.6 ∼ 2.6	3.13 ± 0.28	6	17	15.51 ± 0.57 (± 0.73)	1.7
2	2.7 ∼ 1.8	2.23 ± 0.28	3	17	14.81 ± 0.53	0.4
3	1.7 ∼ 1.0	1.32 ± 0.20	2	17	15.64 ± 0.62	0.7
4	0.65 ∼ 0.40	0.50 ± 0.08	1	17	16.35 ± 0.80 (± 1.08)	1.8
5	0.27 ∼ 0.20	0.23 ± 0.02	1	16	14.16 ± 0.87 (± 0.93)	1.1
6	0.70 ∼ 0.40	0.54 ± 0.09	1	19	14.75 ± 0.86 (± 0.96)	1.3
7	1.8 ∼ 1.1	1.43 ± 0.20	2	16	14.04 ± 0.58 (± 0.78)	1.8
8	2.6 ∼ 2.0	2.27 ± 0.21	5	17	15.88 ± 0.48 (± 0.68)	2.0
9	3.6 ∼ 2.9	3.22 ± 0.23	7	16	15.40 ± 0.45	0.8
x 1	3.6 ∼ 2.9	3.23 ± 0.20	14	16	108.4 ± 3.2	1.6
2	2.7 ∼ 1.8	2.21 ± 0.25	6	16	103.2 ± 3.3	0.8
3	1.7 ∼ 1.0	1.31 ± 0.20	3	16	101.4 ± 3.7	1.0
4	0.55 ∼ 0.35	0.46 ± 0.05	2	16	97.4 ± 4.9	0.5

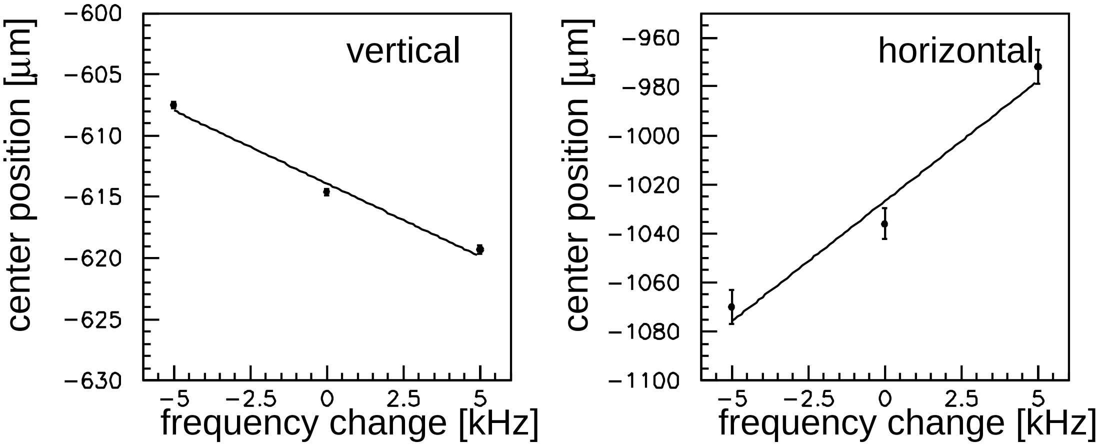

Figure 4.6: Example of the dispersion measurement. The vertical (left) or horizontal (right) beam position was measured changing the RF frequency. The center position was determined by the laserwire. The solid lines were the fit results by a linear function. Dispersion at the collision points were calculated from the dependence on the frequency (μm/kHz).

Table 4.8: Summary of the dispersion measurement

date	run	vertical position shift (μm/kHz)	vertical η_y at h-wire (mm)	horizontal position shift (μm/kHz)	horizontal η_x at v-wire (mm)
2/26	A	-1.43 ± 0.05	2.18 ± 0.08	1.11 ± 0.66	1.69 ± 1.00
4/16	B	-1.19 ± 0.05	1.81 ± 0.08	9.81 ± 0.99	15.0 ± 1.51
5/15	C	N/A		N/A	
5/20	D	-0.05 ± 0.04	0.08 ± 0.06	N/A	
5/23	E,F	N/A		N/A	

where α_M ($= 0.00214$) is the momentum compaction factor and f_{RF} ($= 714$ MHz) is the nominal RF frequency. We measured the beam center position by the laserwire under the different RF frequencies. An example of such measurements is shown in Figure 4.6. We note that the beam center position was extracted as one of the fitting parameter. The measured position shift and the calculated value of the dispersion (η) are summarized in Table 4.8. The vertical (horizontal) dispersion was found to be less than 2 mm (15 mm) for all measurements. Since the energy spread of the electron beam was less than 0.1%, the contribution to the beam size was estimated to be less than 2 μm for the vertical emittance measurement and 15 μm for the horizontal. The effect on the beam size measurement was smaller than 10% even in the case of the vertical beam size as small as 5μm. We neglected this contribution in the following analysis.

Table 4.9: Summary of the tune measurement

date	run	horizontal tune (ν_x)	vertical tune (ν_y)
2/26	A	15.1770	8.5637
4/16	B	15.1770	8.5610
5/15	C	15.1738	8.5419
5/20	D	15.1844	8.5589
5/23	E,F	15.1708	8.5547

4.2.4 Measurement of the beta function

The beta functions at the laserwire position were measured immediately after the every run. Analysis to extract the beta function was done in two stages. First, we measured the beam tunes (ν) by varying the strength of three quadrupole magnets in the neighborhood of the laserwire, namely QM13R, QM14R and QM15R (the laserwire was placed between QM14R and QM15R, see Figure 4.7). The tune was determined by a spectrum measurement of a beam position oscillation excited by the beam exciter. The procedure of the measurement is already described in Sec. 2.2.3. The measured tune values corresponding to the original magnet settings (nominal tune) are listed in Table 4.9. The dependence of a tune is expressed by

$$2\cos(2\pi\nu) = 2\cos(2\pi\nu_0) - \beta_0 \Delta k \sin(2\pi\nu_0) \quad , \tag{4.4}$$

where ν_0 and ν are the nominal tune and the tune corresponding to a quadrupole strength changed by Δk, and β_0 is the beta function to be determined. Figure 4.8 shows the measured values of $\cos(2\pi\nu)$ plotted as a function of Δk. The beta functions at each magnet position were obtained as the slope of a linear function fitted to the data. They are listed in Table 4.10.

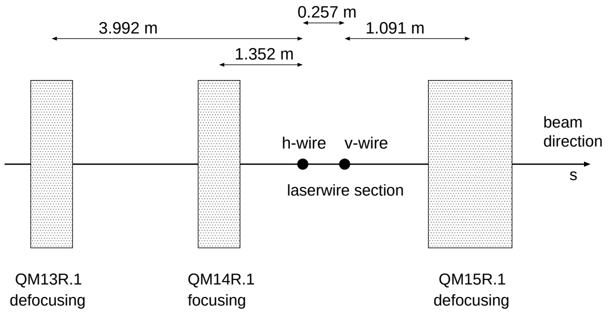

magnet	effective length(l)[m]	$k = Kl$
QM13R.1	0.0855	-0.5133
QM14R.1	0.0855	0.50607
QM15R.1	0.1987	-1.1159

Figure 4.7: Layout of the quadrupole magnets in the neighborhood of the laserwire. In the horizontal direction, QM13R and QM15R are defocussing magnets, and QM14R is a focusing magnet. Their quadrupole strength is listed in the table.

In the second stage, we determined the beta functions at the collision point of the laserwire. The actual procedure is as follows. We use a linear optics model of the ring, and let free the Twiss parameters, α_{LW} and β_{LW}, at the laserwire. The beta function

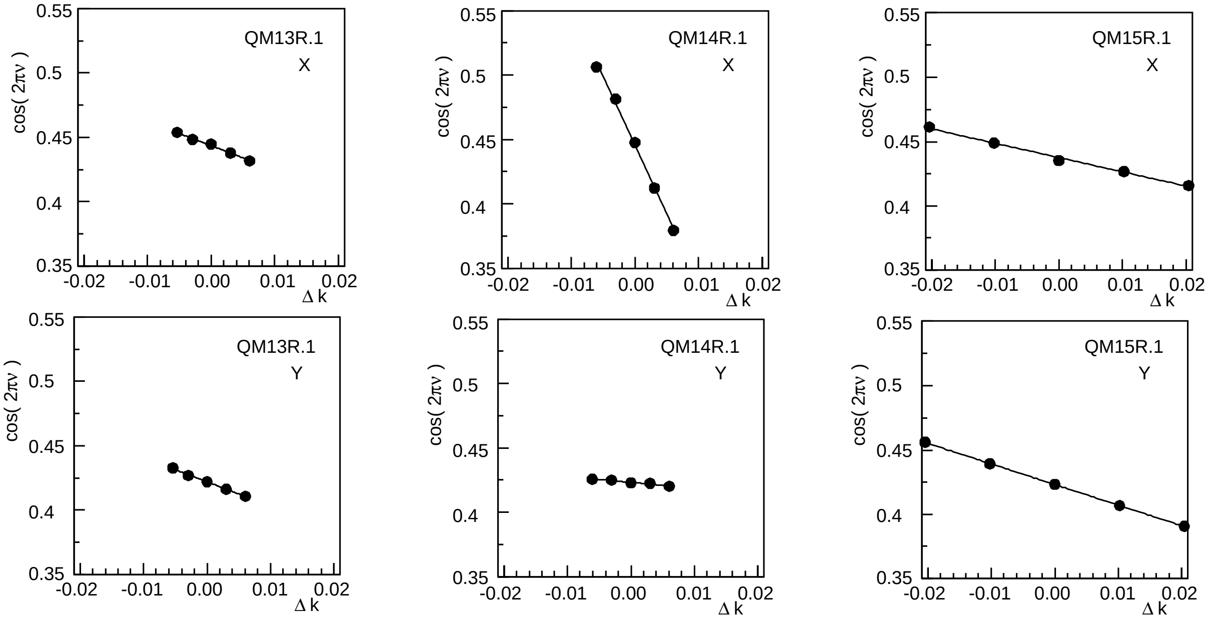

Figure 4.8: Tune shift vs the quadrupole strength. The data taken in run B are shown as an example. The ordinate represents $\cos(2\pi\nu)$ while the abscissa is the change Δk in the quadrupole strength. The solid lines are the fit results by a linear function.

Table 4.10: Results of the beta function measurement at quadrupole magnets.

			beta function at quadrupole magnets		
date	run	direction	QM13R	QM14R	QM15R
2/26	A	x	3.42 ± 0.66	21.47 ± 0.57	2.51 ± 0.15
		y	11.50 ± 0.57	2.12 ± 0.19	8.27 ± 0.18
4/16	B	x	4.20 ± 0.24	23.79 ± 0.82	2.46 ± 0.11
		y	10.12 ± 0.29	2.47 ± 0.26	8.50 ± 0.05
5/15	C	x	2.42 ± 0.59	19.79 ± 0.42	3.07 ± 0.51
		y	10.94 ± 0.50	2.48 ± 0.48	7.74 ± 0.15
5/20	D	x	3.47 ± 0.45	20.75 ± 0.72	2.52 ± 0.06
		y	10.50 ± 1.27	2.22 ± 0.23	7.30 ± 0.19
5/23	E,F	x	3.87 ± 0.27	21.30 ± 0.17	2.24 ± 0.14
		y	10.02 ± 1.36	2.32 ± 0.06	7.80 ± 0.07

Table 4.11: Results of the beta function measurement at the laserwire.

date	run	β_x at h-wire (m)	β_y at v-wire (m)
2/26	A	7.77±0.2	4.57±0.20
4/16	B	8.45±0.4	4.67±0.08
5/15	C	7.67±1.0	4.32±0.18
5/20	D	7.48±0.5	4.00±0.20
5/23	E,F	7.12±0.2	4.34±0.15

can be predicted using the optics model for any given α_{LW} and β_{LW}. We then compared the measured beta function at the magnets (QM13R, QM14R and QM15R) with the predicted values, and minimized the quantity

$$\chi^2(\alpha_{LW}, \beta_{LW}) = \sum_{n=QM13R}^{QM15R} \left(\frac{\beta_{n,meas} - \beta_n(\alpha_{LW}, \beta_{LW})}{\sigma_{n,meas}} \right)^2 \quad , \tag{4.5}$$

where the suffix n specifies the quadrupole magnets and the suffix $meas$ means the measured beta functions at the magnets. $\sigma_{n,meas}$ is the measurement error of $\beta_{n,meas}$. An example of the fit result is shown in Figure 4.9. Typically, β_y at the horizontal-wire was 4.51 m, and β_x at the vertical-wire was 7.45 m. These values were stable within 10% in this series of experiments. They are listed in Table 4.11.

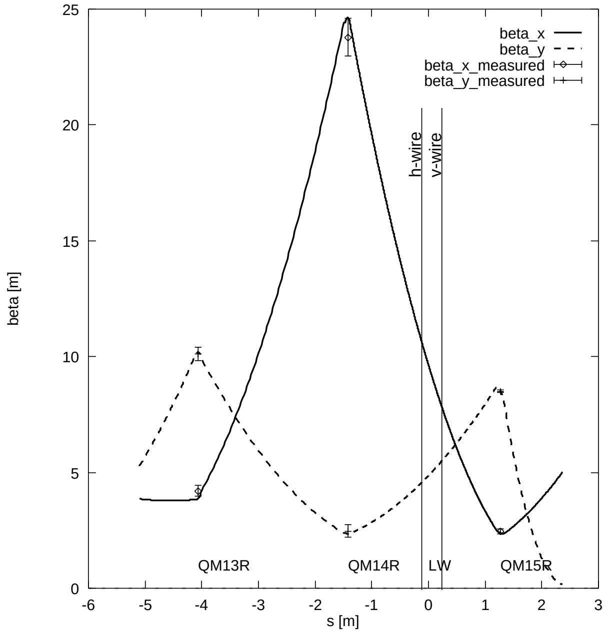

Figure 4.9: Example of the beta function measurement. The measured values of the beta function at three quadrupole magnets are shown by the data points with error bars. The solid (dotted) line is the fit result for the horizontal (vertical) beta function based on the linear optics model. The two laserwire collision points (h-wire and v-wire) are shown by the vertical lines.

4.2.5 Estimation of the transverse emittances

The measured peak width (σ_{meas}) obtained in Sec. 4.2.2 was deconvoluted to obtain an electron beam size (σ_e) using the relation

$$\sigma_e = \sqrt{\sigma_{meas}^2 - \sigma_{lw}^2} \tag{4.6}$$

where σ_{lw} stands for the laserwire width. In Sec.3.4, this was estimated to be σ_{lw}(h-wire) = 5.65 ± 0.08 μm and σ_{lw}(v-wire) = 14.72 ± 0.24 μm. Then the electron beam size was converted into an emittance, using the measured beta function, by

$$\sigma_e = \sqrt{\beta\epsilon} \quad . \tag{4.7}$$

The error on σ_e has contributions from errors on σ_{meas}, σ_{lw} and β. Among them, the errors on σ_{meas} are individual errors associated with each measurement. The errors on σ_{lw} or β, however, is a common error to all data points within a single run. Below, we do not include those common errors in a plot because we would be able to see more clearly the trend or character of the data within a run. At the final stage where comparison between runs is needed, those common errors will be included.

Figure 4.10 ∼ 4.15 show the plot of the emittances as a function of the ring current. The solid and dashed lines in the plots show the fitting results by two kinds of empirical functions, which will be explained in Sec. 4.3.1. As seen in Figure 4.11 (run B) or 4.13 (run D), the data of the best-tuned beam, the vertical emittance reached as small as 4 pm·rad. Also clearly seen is the current dependence for both vertical and horizontal directions. In particular, for the vertical emittance, these are the first data which unambiguously proved the current dependence.

4.2.6 Measurement of the bunch length

The bunch length of the electron beam was measured by a streak camera. It actually measured the pulse length of the synchrotron light. One example is shown in Figure 4.16. In the figure, the vertical axis corresponds to the time structure, and the horizontal axis to the horizontal profile of the SR light. We defined an area for the synchrotron light signal to be inside the box in Figure 4.16. The signal intensity distribution was projected into the time axis, and was fitted by a Gaussian function to estimate the size on the CCD camera. The bunch length was calculated using the calibration factor of the time axis (1.85 [pixel/psec]). Prior to the measurement, we checked the focusing condition without a sweep signal for the time axis. The input light was found to be well focused on the photo-cathode, as shown in Figure 4.17. It was confirmed that the signal width without the sweep was negligible compared to an actual time structure by the beam.

We took three sets of the bunch length data corresponding to the ring conditions of run D, E and F. Actually, those data were taken on May 23, the last day of this series of runs, reproducing the respective ring conditions.

The data were continuously taken using a stored beam every ∼7 seconds, and were classified according to the beam current of every 0.5 mA. The results of three data sets (denoted as D', E', F') are shown in Figure 4.18. The errors were defined to be the fluctuation of the results (rms). A linear function was employed to fit the current dependence of the data.

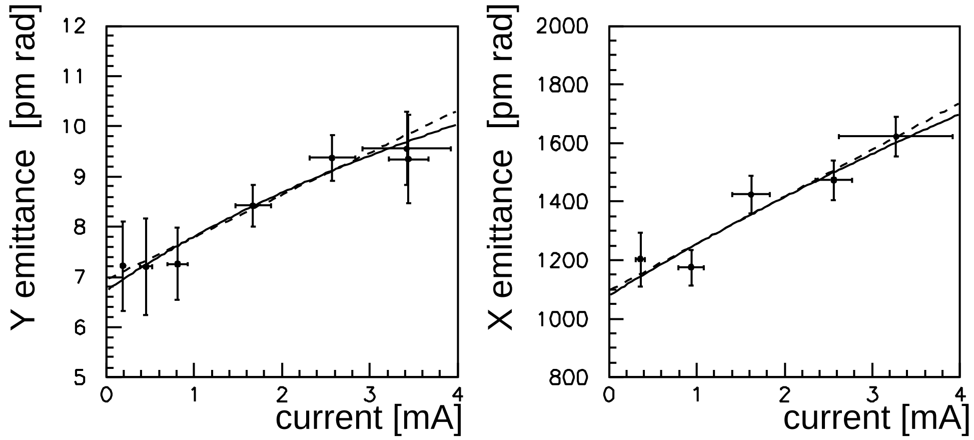

Figure 4.10: Current dependence of emittances (run A). The error bars include the uncertainty stemming from σ_{meas}, not from σ_{lw} or β.

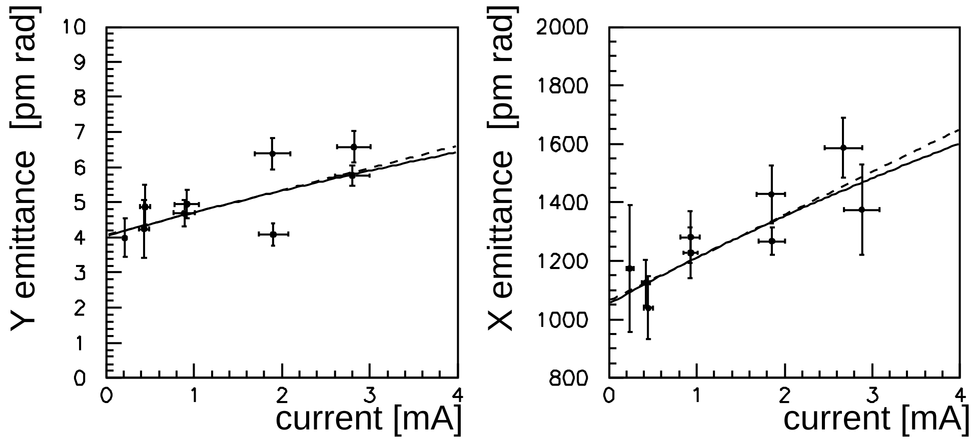

Figure 4.11: Current dependence of emittances (run B). The error bars include the uncertainty stemming from σ_{meas}, not from σ_{lw} or β.

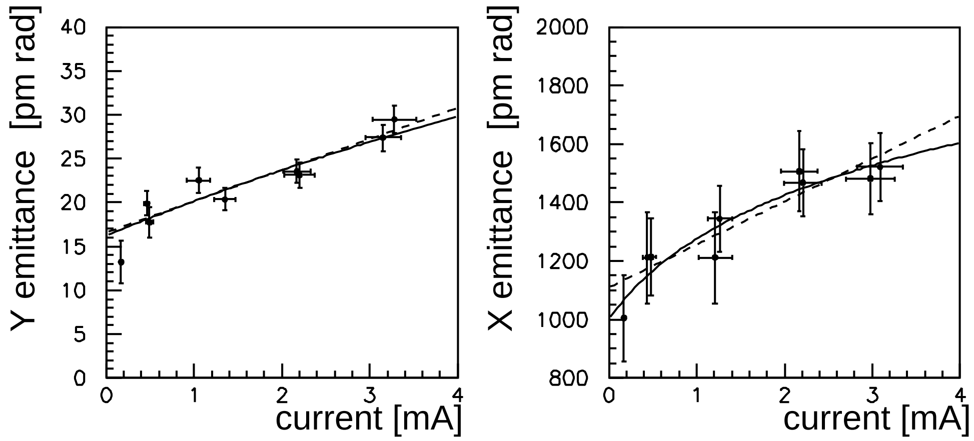

Figure 4.12: Current dependence of emittances (run C). The error bars include the uncertainty stemming from σ_{meas}, not from σ_{lw} or β.

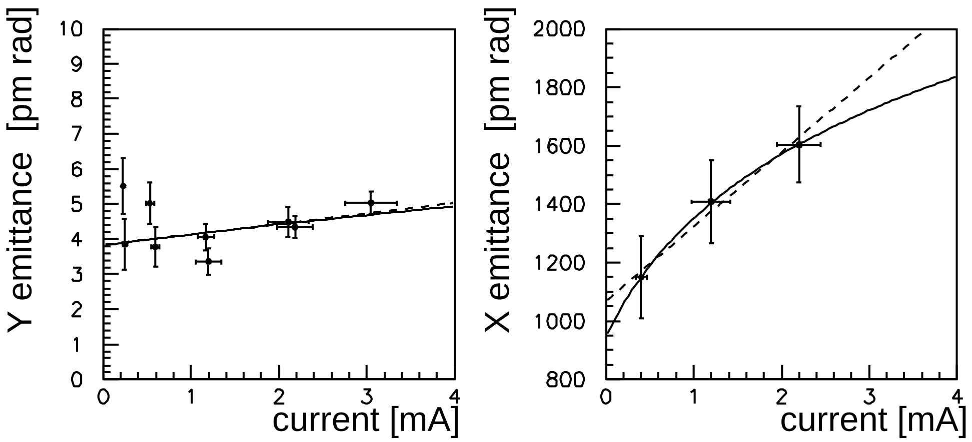

Figure 4.13: Current dependence of emittances (run D). The error bars include the uncertainty stemming from σ_{meas}, not from σ_{lw} or β.

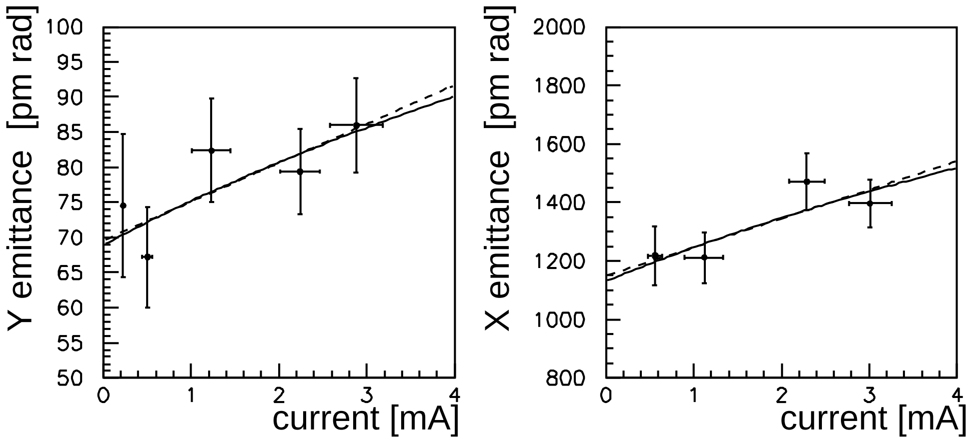

Figure 4.14: Current dependence of emittances (run E). The error bars include the uncertainty stemming from σ_{meas}, not from σ_{lw} or β.

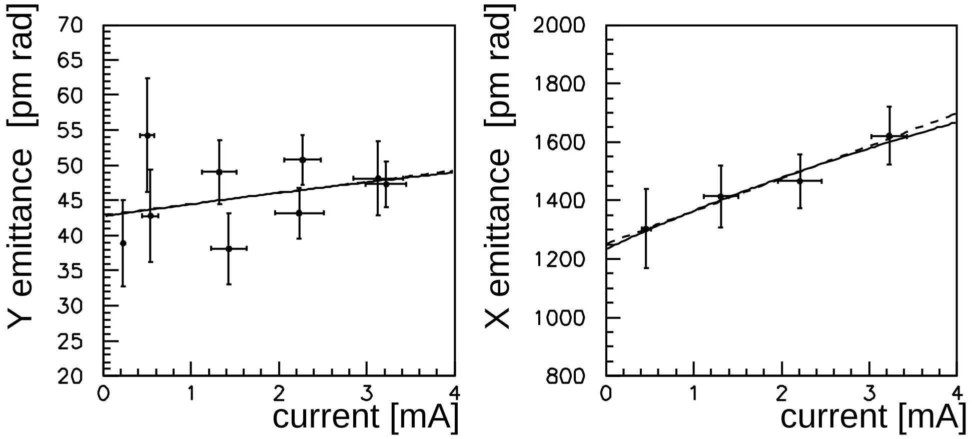

Figure 4.15: Current dependence of emittances (run F). The error bars include the uncertainty stemming from σ_{meas}, not from σ_{lw} or β.

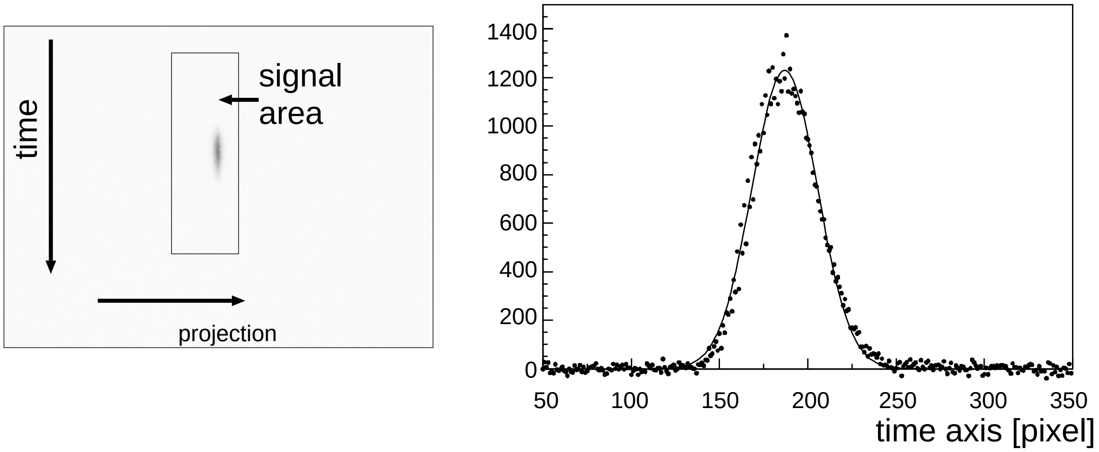

Figure 4.16: Example of the bunch length measurement by the streak camera. (left) Two dimensional plot of the measured light intensity. The vertical (horizontal) axis corresponds to the time (spatial) distribution of the light. The full scale of the vertical axis is about 2 nsec. The rectangular box is the selected area for synchrotron light signal. (right) The projected data on the time axis. The solid line is the fit result by a Gaussian function.

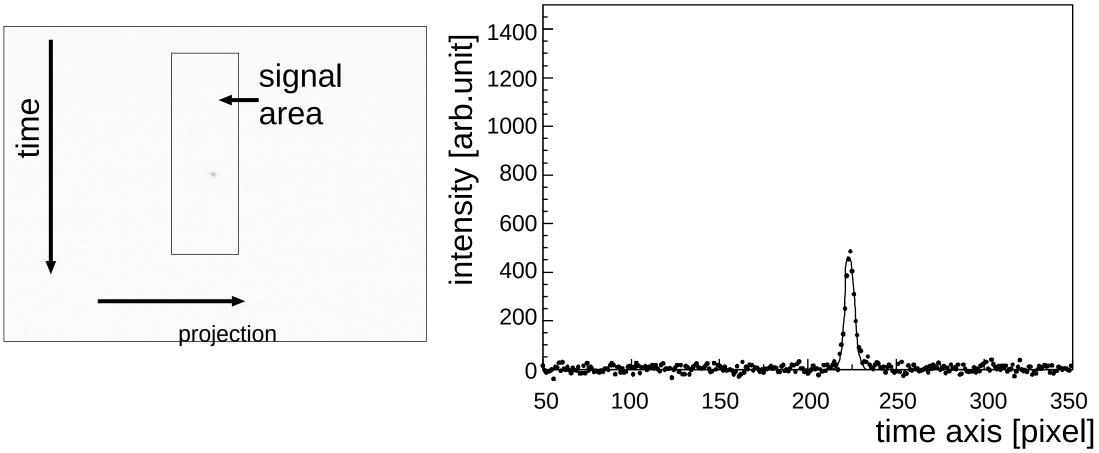

Figure 4.17: Example of the calibration measurement by the streak camera. The data was taken without the sweep signal to check the focusing property. (left) Two dimensional plot of the light intensity. (right) The projected data on the time axis. The contribution of the spatial size of the light was confirmed to be negligible.

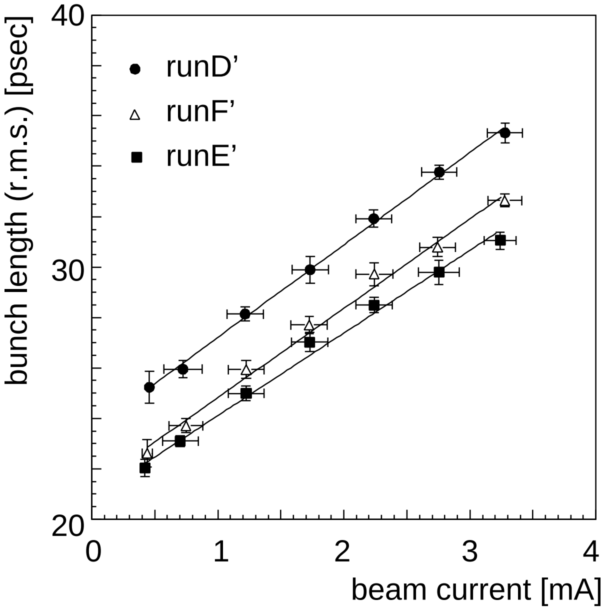

Figure 4.18: Current dependence of the bunch length. The measured values are shown as a function of the beam current for three runs (D', E', and F') with different beam tuning conditions. The solid lines are the fitting result with a linear function.

4.2.7 Measurement of the momentum spread

We took two sets of the momentum spread data. One was taken on the same day as run D, the best-tuned beam. The other was taken two weeks after run E, reproducing the same condition of run E (run E'). The electron beam profiles were measured by the screen monitor in the high dispersion region of the extraction line. The horizontal beam sizes (σ_x), dominated by the dispersion effect, were obtained by fitting the horizontal profiles with a Gaussian function. The dispersion at the screen was measured to be $\eta_x = 1.79$m. The momentum spread ($\Delta p/p$) was estimated from σ_x via Eq.2.4.

The results are shown in Figure 4.19. A clear current dependence is seen especially in the data of run D. The solid lines are the fitting results which will be explained in Sec. 4.3.3.

4.3 Results

As already seen, all measured values of the emittance, bunch length and momentum spread have clear intensity dependence. In order to discuss the overall nature of current dependence, we will characterize these values with two parameters: one is the value at the zero current, and the other is the ratio of the value at 10^{10} [electron/bunch] and the zero current. We call the latter parameter "the enhancement factor" in this section. The zero current value of the horizontal (vertical) emittance, bunch length and momentum spread are denoted by $\epsilon_{x(y)}^{(0)}$, $\sigma_z^{(0)}$ and $(\Delta p/p)^{(0)}$, and those corresponding enhancement factors by $r_{\epsilon_{x(y)}}^{(10)}$, $r_{\sigma_z}^{(10)}$ and $r_{\Delta p/p}^{(10)}$, respectively. We will compare these parameters with those obtained by simulation.

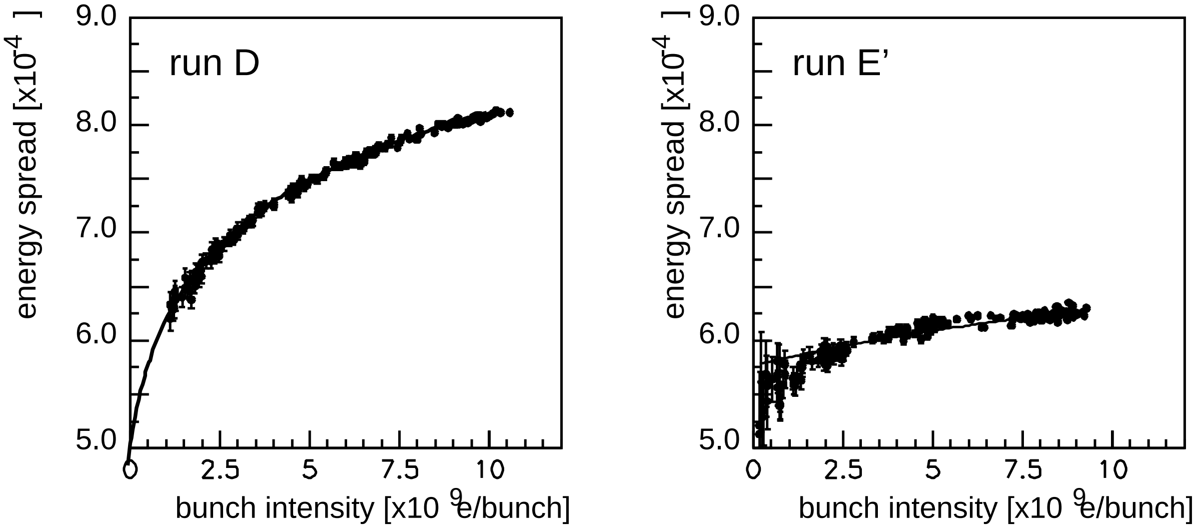

Figure 4.19: Current dependence of the momentum spread. The measured values are plotted as a function of the beam intensity for two different runs (D and E'). Run D was the best-tuned beam while run E' was the worst-tuned beam. The solid lines are the fit results by a logarithmic function of Eq.4.10.

4.3.1 Transverse emittances

We extracted the emittance at zero intensity limit ($\epsilon^{(0)}_{x(y)}$) and the emittance enhancement factor ($r^{(10)}_{\epsilon_{x(y)}}$) in the following manner. In Figure 4.10 ∼ 4.15, we plotted the measured emittances as a function of the beam current. Those data points were fitted by two types of empirical functions to estimate $\epsilon^{(0)}_{x(y)}$ and $r^{(10)}_{\epsilon_{x(y)}}$. One was a simple linear function with two free parameters:

$$\epsilon(N) = a\ N + \ b \quad , \tag{4.8}$$

where a and b are free parameters, and N represents the bunch intensity ([electrons/bunch]). From the resultant parameters, we estimated the value at zero current ($\epsilon(0) = b$), and the value at $N = 10^{10}$ ($\epsilon(10^{10}) = a \times 10^{10} + b$). We then determined the enhancement factor $r^{(10)}_{\epsilon} = \epsilon(10^{10})/\epsilon(0)$.

The other fitting function was an empirical function which could well reproduce the simulation results by the SAD program [21] (It will be explained in Sec. 4.4.2.),

$$\epsilon(N) = a\ \log(\ b\ N + c\ ) \quad , \tag{4.9}$$

with three free parameters (a, b and c). Two values, $\epsilon^{(0)} = a\log(c)$ and $r^{(10)}_{\epsilon} = \frac{\epsilon(10^{10})}{\epsilon(0)} = \log(b \times 10^{10} + c)/\log(c)$, were extracted from the resultant parameters.

In the case that χ^2/ν was larger than unity, we enlarged the errors of all data points uniformly so that $\chi^2/\nu = 1$. Unknown systematic effects were conservatively included in this treatment.

The broken and the solid line in Figure 4.10 ∼ 4.15 are the results of the fitting with a linear and logarithmic functions, respectively. In these figures, 3.5 mA corresponds to $N = 10^{10}$ electrons/bunch. As seen, both functions fit the data points fairly well.

In the second step, we considered the contribution of the uncertainty from σ_{lw} and β measurements. The procedures of the first step were repeated while randomly changing the values of σ_{lw} and β according to a Gaussian distribution with the standard deviation determined by the measurement. The rms fluctuation stemmed from this treatment was defined to be a systematic error for $\epsilon_{x(y)}^{(0)}$ and $r_{\epsilon_{x(y)}}^{(10)}$.

The results of the two analysis are listed in Table 4.12. Each value has two errors; the first one stems from the uncertainty in the σ_{meas} measurement, while the second one includes the additional contribution from the uncertainty in σ_{lw} and β measurements. The total error was the convolution of these two in quadrature, which will be used in Sec. 4.4.

It should be noted that we attained the vertical emittance of 4 pm·rad at the zero-intensity limit (ϵ_0) in run B and D. These were the smallest values ever recorded in the world.

4.3.2 Bunch length

As already described, the data of the bunch length showed a clear linear dependence on the beam current (see Figure 4.18.). Thus the data were fitted only with a linear function. The value at zero current and the enhancement factor at 10^{10} [e/bunch] were estimated from the result of the fitting, and are listed in Table 4.13.

4.3.3 Momentum spread

The data of the momentum spread were analyzed in a similar way. We used the same logarithmic fitting function used in the emittance analysis.

$$\frac{\Delta p}{p}(N) = a \ \log(\ b \ N + c \ ) \quad , \tag{4.10}$$

with three free parameters (a, b and c). The fitting result is shown by the solid line in Figure 4.19. Two values, the momentum spread at zero-current ($(\Delta p/p)^{(0)}$) and the enhancement factor at 10^{10} [e/bunch] ($r_{\Delta p/p}^{(10)}$), were extracted from the resultant parameters. These results are listed in Table 4.14.

4.4 Discussion

There are several prominent features in the data shown in the previous section. First of all, we observed a strong current dependence of the momentum spread. (see Figure 4.19.). Second, the bunch length data themselves showed a clear current dependence, but not their slopes (see Figure 4.18.). Third, the vertical emittance was affected drastically by the beam tuning conditions. As for the transverse emittances, a clear current dependence was observed in both horizontal and vertical direction.

There are two important mechanisms which may cause these current dependences. The first one is the longitudinal wake field induced by the impedance of the beam line. The longitudinal wake field reduces the effective accelerating voltage (V_c) in the ring, resulting

Table 4.12: Results of fitting analysis (emittance). Two types of functions, a linear and logarithmic functions, are employed to estimate the emittance of zero-current limit ($\epsilon_{x(y)}^{(0)}$) and the emittance enhancement factor at 10^{10} [e/bunch] intensity ($r_{\epsilon_{x(y)}}^{(10)}$). Each value has two errors. The first error is from σ_{meas}, the statistical error of the count rate of the γ rays and the reproducibilities of the Gaussian beam profiles obtained in one round trip. The second error is the systematic error originated from the uncertainty of the beta function (β) and the width of the laser beam (σ_{lw}). The chi-square per degree of freedom (χ^2/ndf) of the fitting is also listed.

horizontal (fitting by a straight line)			
run	$\epsilon_x^{(0)}$ [10^{-9} m rad]	$r_{\epsilon_x}^{(10)}$	χ^2/ν
A	1.096 ± 0.073 ± 0.029	1.50 ± 0.16 ± 0.00	0.83
B	1.066 ± 0.062 ± 0.051	1.47 ± 0.15 ± 0.00	0.92
C	1.131 ± 0.86 ± 0.158	1.45 ± 0.17 ± 0.00	0.30
D	1.073 ± 0.167 ± 0.073	1.81 ± 0.49 ± 0.00	0.10
E	1.149 ± 0.099 ± 0.025	1.29 ± 0.17 ± 0.00	0.77
F	1.253 ± 0.123 ± 0.027	1.30 ± 0.18 ± 0.00	0.07
vertical (fitting by a straight line)			
run	$\epsilon_y^{(0)}$ [10^{-12} m rad]	$r_{\epsilon_y}^{(10)}$	χ^2/ν
A	6.97 ± 0.53 ± 0.46	1.41 ± 0.16 ± 0.02	0.19
B	4.11 ± 0.53 ± 0.34	1.53 ± 0.30 ± 0.05	3.09
C	16.68 ± 1.09 ± 0.79	1.72 ± 0.17 ± 0.02	1.20
D	3.87 ± 0.43 ± 0.44	1.27 ± 0.23 ± 0.03	1.87
E	69.86 ± 6.37 ± 4.13	1.27 ± 0.19 ± 0.01	0.49
F	43.10 ± 3.71 ± 2.56	1.13 ± 0.14 ± 0.00	1.05

horizontal (fitting by a logarithmic function)			
run	$\epsilon_x^{(0)}$ [10^{-9} m rad]	$r_{\epsilon_x}^{(10)}$	χ^2/ν
A	1.08 ± 0.09 ± 0.03	1.51 ± 0.18 ± 0.00	1.26
B	1.05 ± 0.07 ± 0.05	1.46 ± 0.15 ± 0.00	1.09
C	1.01 ± 0.11 ± 0.12	1.55 ± 0.16 ± 0.02	0.215
D	0.94 ± 0.31 ± 0.06	1.88 ± 0.64 ± 0.01	/
E	1.12 ± 0.14 ± 0.02	1.31 ± 0.21 ± 0.01	1.49
F	1.23 ± 0.14 ± 0.02	1.31 ± 0.19 ± 0.00	0.181
vertical (fitting by a logarithmic function)			
run	$\epsilon_y^{(0)}$ [10^{-12} m rad]	$r_{\epsilon_y}^{(10)}$	χ^2/ν
A	7.11 ± 0.62 ± 0.49	1.42 ± 0.16 ± 0.02	0.195
B	4.47 ± 0.64 ± 0.37	1.48 ± 0.30 ± 0.04	3.64
C	16.85 ± 1.32 ± 0.79	1.71 ± 0.19 ± 0.01	1.44
D	4.30 ± 0.51 ± 0.47	1.23 ± 0.23 ± 0.03	2.21
E	69.21 ± 6.78 ± 2.34	1.27 ± 0.18 ± 0.00	0.721
F	43.07 ± 4.21 ± 1.49	1.13 ± 0.15 ± 0.00	1.22

Table 4.13: Results of fitting analysis (bunch length). The bunch length of zero-current limit ($\sigma_z^{(0)}$) and the enhancement factor at 10^{10} [e/bunch] ($r_{\sigma_z}^{(10)}$) are listed.

run	zero-current limit ($\sigma_z^{(0)}$) [psec]	enhancement factor ($r_{\sigma_z}^{(10)}$)	χ^2/ν
D'	23.5 ± 0.5	1.54 ± 0.05	0.09
E'	20.8 ± 0.4	1.54 ± 0.04	0.39
F'	21.3 ± 0.5	1.58 ± 0.05	0.35

Table 4.14: Results of fitting analysis (momentum spread). The momentum spread of zero current limit ($(\Delta p/p)^{(0)}$) and the enhancement factor at 10^{10} [e/bunch] ($r_{\Delta p/p}^{(10)}$) are listed.

run	zero current limit [$\times 10^{-4}$] ($(\Delta p/p)^{(0)}$)	enhancement factor ($r_{\Delta p/p}^{(10)}$)	χ^2/ν
D	4.730 ± 0.103	1.713 ± 0.037	0.74
E'	5.767 ± 0.014	1.095 ± 0.003	2.46

in the bunch lengthening. The second is the intra-beam scattering, *i.e.* the multiple Coulomb scattering of the particles in a bunch which transforms the transverse momentum into the longitudinal motion, resulting in the growth of the momentum spread. In addition, due to the dispersion, this momentum transfer excites the transverse emittance at the same time.

The dominant source of the intensity dependence of the transverse emittance and the momentum spread is considered to be intra-beam scattering. The higher the particle density (smaller vertical emittance), the stronger is the effect of intra-beam scattering. This has been clearly seen in the momentum spread data though it was less evident in the transverse emittances. On the other hand, the current dependence of the bunch length was strong even in the data for which the vertical emittance was worsened on purpose (see Figure 4.18 run E'.). This current dependence of the bunch length is thus considered to be caused mainly by the longitudinal wake fields. The bunch lengthening dilutes the particle density, and makes slower the growth rate by the intra-beam scattering.

Below, we try to understand the overall nature of the observed intensity dependences more quantitatively employing models and simulations.

4.4.1 Estimation of the impedance effect

Naively, the bunch length is determined by the slope of the RF voltage, $dV_{RF}(t)/dt$, which gives a restoring force of the synchrotron motion. Since the RF voltage is given by a sinusoidal function, the slope of the voltage is proportional to its peak voltage (V_C). The impedance-induced wake field changes in principle the effective RF voltage. For example, if the impedance is purely inductive, the wake field can be expressed as

$$V_{w.f.} = -L\frac{dI(t)}{dt} \tag{4.11}$$

where L is the impedance of the beam line and I the beam current. The effective RF voltage is reduced by $V_{w.f.}$ in this case. In fact, the calculation based on the structure of the chambers of the actual beam line suggests a purely inductive impedance. We tried to include this impedance effect in the SAD simulation program, and to compare its results with the actual data. Since the impedance effects could not be included directly in SAD, the impedance effect was simulated by changing the effective RF voltage (V_c).

In order to calculate $V_{w.f.}$ in Eq. 4.11, we need to know $I(t)$ and L. For $I(t)$, we employed a parabolic shape, as illustrated in Figure 4.20, for simplicity. It is expressed by

$$I(t) = \frac{3N}{4a}\left(1-\left(\frac{t}{a}\right)^2\right) \quad , \tag{4.12}$$

where a represents the bunch length, and N is the total charge. The wake field induced by this bunch shape is calculated to be

$$V_{w.f.} = -L\frac{dI(t)}{dt} = -L\frac{3N}{2a^3}t \quad . \tag{4.13}$$

In this model, the reduction of the effective RF voltage should be proportional to N/σ_z^3 ($\sigma_z \propto a$).

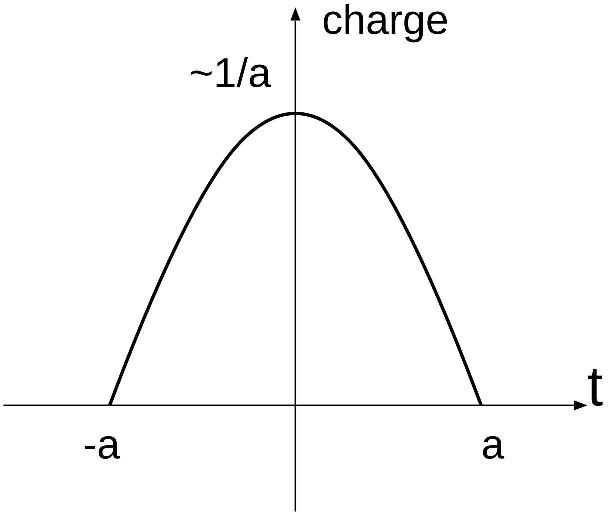

Figure 4.20: Simple model for the longitudinal bunch shape. The longitudinal charge distribution is expressed by a parabolic function of Eq. 4.12. In this model, the bunch length is given by a, and the total charge is the area under the parabola.

We now need to determine L, and it was done as follows using the actual bunch length data. We sought an effective V_c which could reproduce the data. In this procedure, we were in turn required to assume the x-y coupling, which affected the bunch length. To this end, we assumed 6% for run D', 3% for run F', and 0.4% for run E', based on the fact that the ratio of the vertical to horizontal emittance at zero current is 6%, 3%, and 0.4%, respectively for run D, E and F. (See the intersects at zero current in Figure 4.13, Figure 4.14 and Figure 4.15.)

The effective V_c obtained in this manner were plotted as a function of N/σ_z^3 (Figure 4.21). If the impedance was purely inductive, the reduction of effective V_c should be proportional to N/σ_z^3 as explained above. All data points in Figure 4.21 gather around a straight line, supporting the inductive impedance model with a common inductance L. The broken line is the result of fitting of all data points with a linear function.

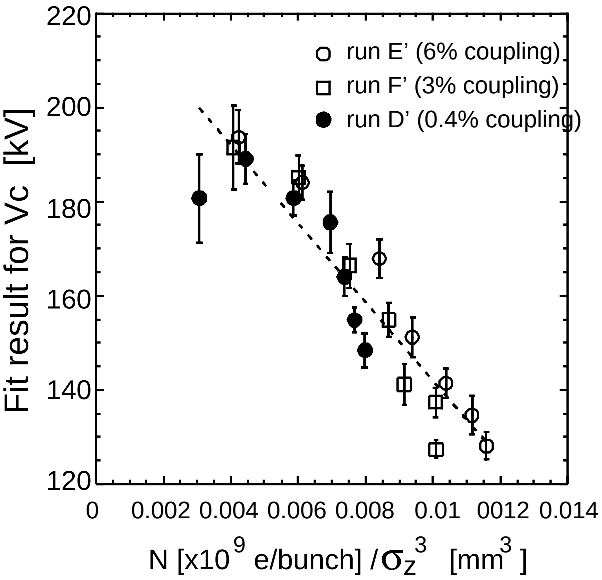

Figure 4.21: Fit result for V_c as a function of N/σ_z^3. The fit result for V_c is the best value which can explain the measured bunch length. The x-y coupling of 6%, 3% and 0.4% are assumed for run E', F' and D', respectively. The reduction in V_c is found to be proportional to N/σ_z^3, indicating that the impedance is purely inductive. The relation shown in the broken line is used in the simulation of the emittances and momentum spread.

4.4.2 Simulation of the emittance and the momentum spread

We are now in a position to examine the current dependence of the observed emittances and momentum spread. We actually employed the SAD simulation program which included both intra-beam scattering effect and impedance effect. As discussed in the previous section, the latter effect was taken as the effective V_c depending on the bunch current. The simulation was done for three conditions of the ring: 0.4%, 3% and 6% x-y coupling. Since the source of the vertical emittance was assumed to be dominated by the x-y coupling, the vertical emittance was simply 0.4%, 3% and 6% of the horizontal emittance. The results of the simulation were shown in Figure 4.22$\sim$4.24. The solid lines were the fitting results with the same logarithmic function of Eq. 4.9 or Eq. 4.10. To discuss the simulation and the experimental results in the same frame work, the intensity dependences were represented by two values, the value at zero-current limit and the enhancement factor at 10^{10}. They are listed in Table 4.15.

4.4.3 Comparison with the calculation

We can now compare the simulation results with the measured data. We have already summarized several characteristic parameters in Table 4.12, 4.14 and 4.15. In order to clarify key features of the data, we checked various correlations of these parameters. They are shown in Figure 4.25 $\sim$ 4.29, in which the data of 6 runs are plotted as rectangles, and the crosses shows the calculation result for three conditions. Figure 4.25, 4.26 and

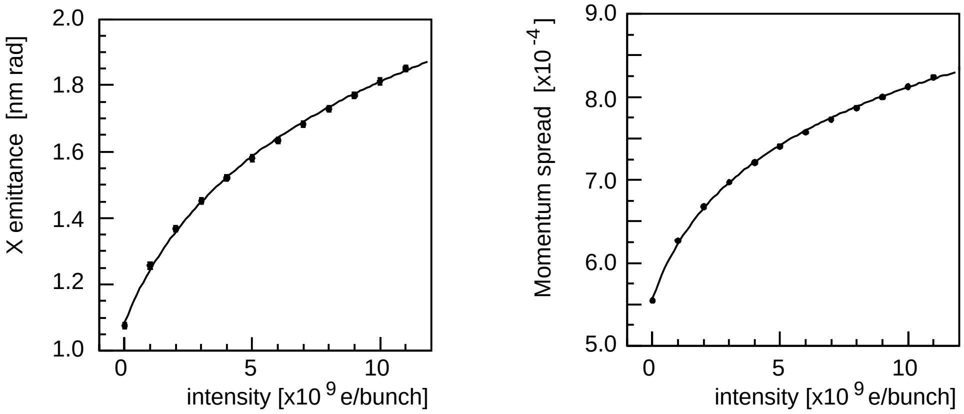

Figure 4.22: Simulation result for the emittance and the momentum spread (0.4% coupling)

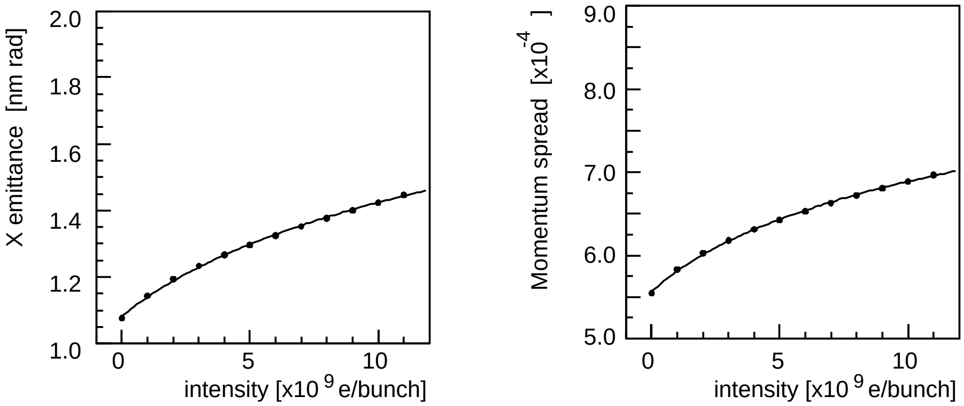

Figure 4.23: Simulation result for the emittance and the momentum spread (3% coupling)

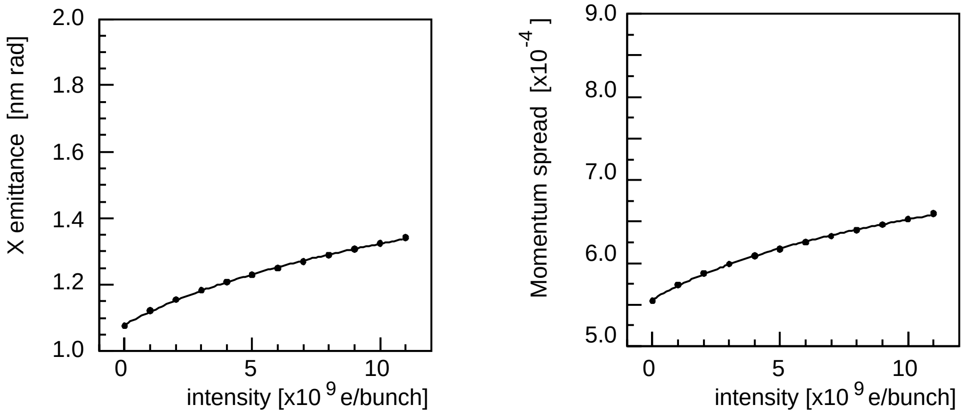

Figure 4.24: Simulation result for the emittance and the momentum spread (6% coupling)

Table 4.15: Simulation results of the current dependence.

	horizontal emittance		momentum spread	
coupling	zero current [nm rad]	enhancement factor at 10^{10} [e/bunch]	zero current [$\times 10^{-4}$]	enhancement factor at 10^{10} [e/bunch]
0.4%	1.077	1.683	5.547	1.464
3%	1.077	1.323	5.547	1.241
6%	1.077	1.230	5.547	1.177

4.27 show the correlations of $\epsilon_y^{(0)}$ vs $r_{\epsilon_y}^{(10)}$, $\epsilon_y^{(0)}$ vs $r_{\epsilon_x}^{(10)}$, and $\epsilon_y^{(0)}$ vs $r_{\Delta p/p}^{(10)}$, respectively. The calculation expects that $r_{\epsilon_{x(y)}}^{(10)}$ and $r_{\Delta p/p}^{(10)}$ decrease as $\epsilon_y^{(0)}$ increases. Since the particle density increases as the vertical emittance decreases, it makes the effect of the intra-beam scattering strong. The data shows the same tendency slightly for the emittances, and clearly for the momentum spread.

Figure 4.28 and 4.29 are the correlations of $\epsilon_y^{(0)}$ vs $\epsilon_x^{(0)}$, and $\epsilon_y^{(0)}$ vs $\Delta p/p^{(0)}$. In the zero current limit, the intra-beam scattering effect should vanish. Thus, no dependence on the bunch size is expected. The data supports this expectation.

4.5 Summary

We have presented the achievement of the smallest vertical beam emittance in the ATF damping ring. The improvements on the read-out circuit of the beam position monitors in the damping ring, the beam based correction of BPM offset, and the optics diagnostics involving beam based methods, all proved essential for this achievement. The transverse emittances were measured with the upgraded laserwire monitor. The measured smallest vertical emittance was 4 pm·rad in the limit of zero-current. Roughly speaking, the vertical and horizontal emittances were 1.5 times bigger at 10^{10} [electrons/bunch] intensity than those at zero current. No clear difference was seen in the strength of the current dependence between the horizontal and vertical plane. The current dependence seems to be weaker as the zero-current emittance becomes larger (larger coupling or vertical dispersion). This can be easily understood since the lower electron density reduces the rate of intra-beam scattering. The measured data and the calculations of intra-beam scattering were consistent within the error bars.

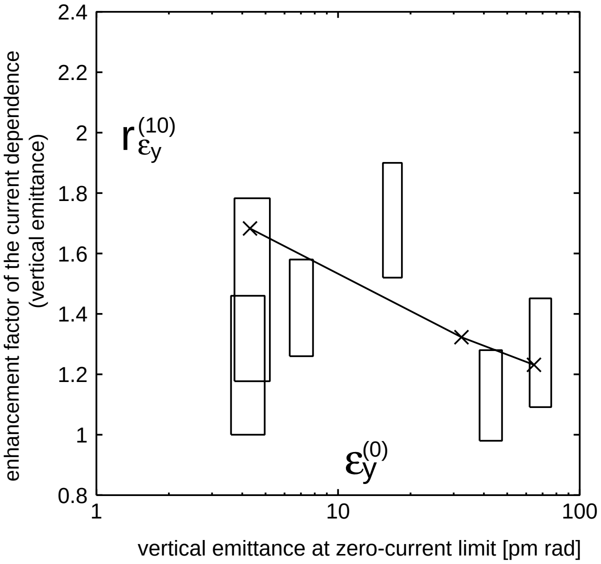

Figure 4.25: Correlation between $\epsilon_y^{(0)}$ and $r^{(10)}_{\epsilon_y}$. The measured values and the simulation results are shown by the box and cross, respectively. The simulation result indicates that the strength of intra-beam scattering increases as the bunch volume ($\epsilon_y^{(0)}$) decreases. This tendency seems to exist vaguely in the measurement results.

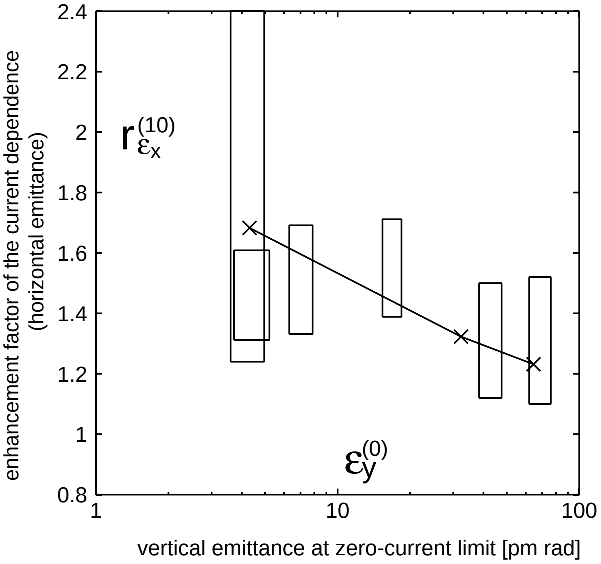

Figure 4.26: Correlation between $\epsilon_y^{(0)}$ and $r^{(10)}_{\epsilon_x}$. The measured values and the simulation results are shown by the box and cross, respectively. The simulation result indicates that the strength of intra-beam scattering increases as the bunch volume ($\epsilon_y^{(0)}$) decreases. This tendency seems to exist vaguely in the measurement results.

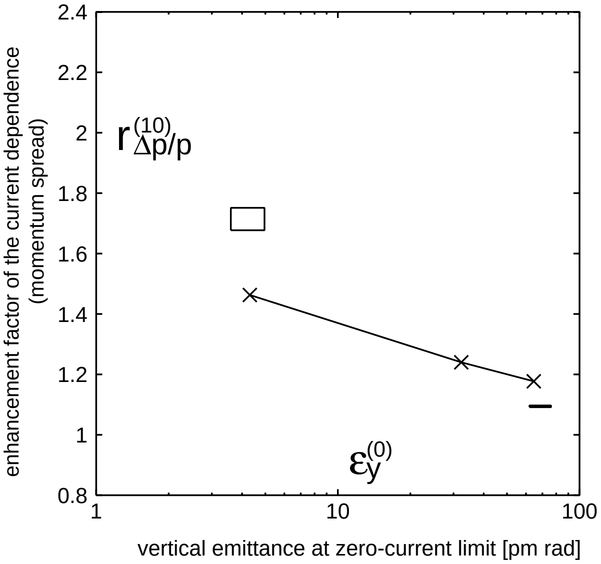

Figure 4.27: Correlation between $\epsilon_y^{(0)}$ and $r^{(10)}_{\Delta p/p}$. The simulation as well as the experimental results show a clear bunch-volume dependence.

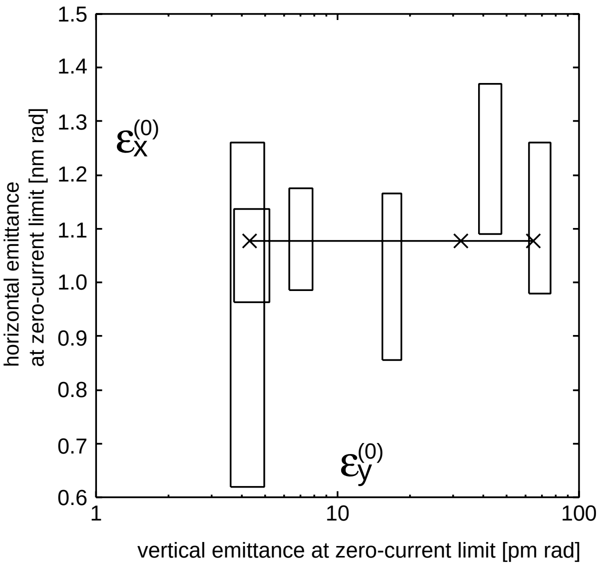

Figure 4.28: Correlation between $\epsilon_y^{(0)}$ and the $\epsilon_x^{(0)}$. The effect of intra-beam scattering vanishes at zero-intensity. No bunch volume dependence is expected in this plot. The experimental data support this expectation.

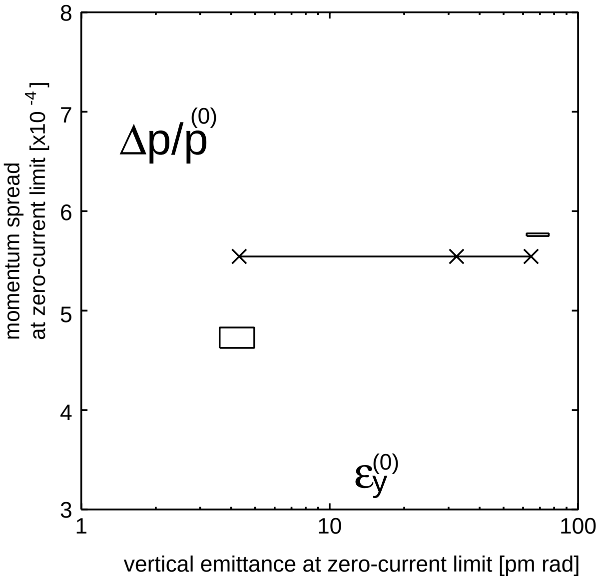

Figure 4.29: Correlation between $\epsilon_y^{(0)}$ and $\Delta p/p^{(0)}$. The effect of intra-beam scattering vanishes at zero-intensity. No bunch volume dependence is expected in this plot.

Chapter 5

Experiments with a Multi-Bunch Beam

5.1 Introduction

Future linear colliders are designed to use a multi-bunch beam to attain their required luminosity. Thus, realization of a small emittance in a multi-bunch beam should also be confirmed experimentally.

In this section, we begin by explaining needed modifications to the laserwire system, which enable a separate profile measurements for each bunch. Then we present the results of studies with the multi-bunch beams. We carried out 4 runs in total with the following purposes:

Run 1 A systematic emittance measurement of a multi-bunch beam ([41]). Both horizontal and vertical emittances were measured, and their bunch-number and intensity dependence were studied.

Run 2 and 3 A pair of runs to compare the vertical emittances between the single and multi-bunch modes under a well-tuned ring condition. The two modes were switched consecutively not to alter other ring conditions.

Run 4 A pressure dependence study. The vacuum pressure was intentionally increased to study the ion-induced coupled bunch effect.

Table 5.1: Experiments with a multi-bunch beam

date	run	aim
December 03, 2002	1	bunch-number and intensity dependence
June 06, 2002	2 and 3	comparison with the single bunch mode
June 13,2003	4	pressure dependence study

5.2 Laserwire monitor for multi-bunch beam measurement

In order to measure beam sizes of each bunch in a multi-bunch train, the laserwire monitor was upgraded. We describe below the modifications of the monitor and of the data analysis procedures for the multi-bunch modes.

5.2.1 Data taking system

Identification of an individual bunch in a multi-bunch beam can be made by detecting a timing signal of the Compton scattering.

In order to detect the signal timing, the readout circuits were modified, as shown in Figure 5.1. At the first stage of the circuits, energy and timing of each event were measured. Here, an amplified signal was discriminated with three different threshold levels of 5, 15 and 25 MeV. Among these three, the energy range of 15-25 MeV was defined as the signal window. When events had an energy in this range, a logic pulse of NIM level was produced with the timing given by the 5 MeV discriminator. This discriminator employed a technique of leading edge extrapolation to minimize time walk caused by pulse height variation. We estimated the timing resolution of this system using background events by a single bunch beam. The background signals had broad energy spectrum and were expected to be synchronized with the beam. The correlation between the energy and detected timing of the 5 MeV discriminator is shown in Figure 5.2(a). Figure 5.2(b) shows the timing distribution of the events in the signal window. From the width of the distribution in Figure 5.2(b), the timing resolution was estimated to be about 0.56 nsec; this should be compared with the 2.8 nsec bunch spacing, enough for the bunch identification.

At the second stage of the circuits, the bunch number was identified. A newly developed electronics module called "Bunch Marker" (BM) played this role. This module was made with a combination of a Time-to-Amplitude Converter (TAC) and a set of comparators, and had 24 outputs corresponding to each bunch. The beam revolution clock provided by the accelerator was used as a start signal to the BM. The stop signal was the timing signal formed in the first stage. The performance of the circuits is shown in Figure 5.3. Each channel of the BM output corresponds to each timing of the beam (each bunch). The output signals from the BM were fed into two 24-input scalers, one for the laser "ON" state and the other "OFF" state. Each scaler channel measures the signal counts for each bunch in the train. The data acquisition system of the multi-bunch experiment was the same as that of the single bunch case, but it had much more scaler channels to be read out.

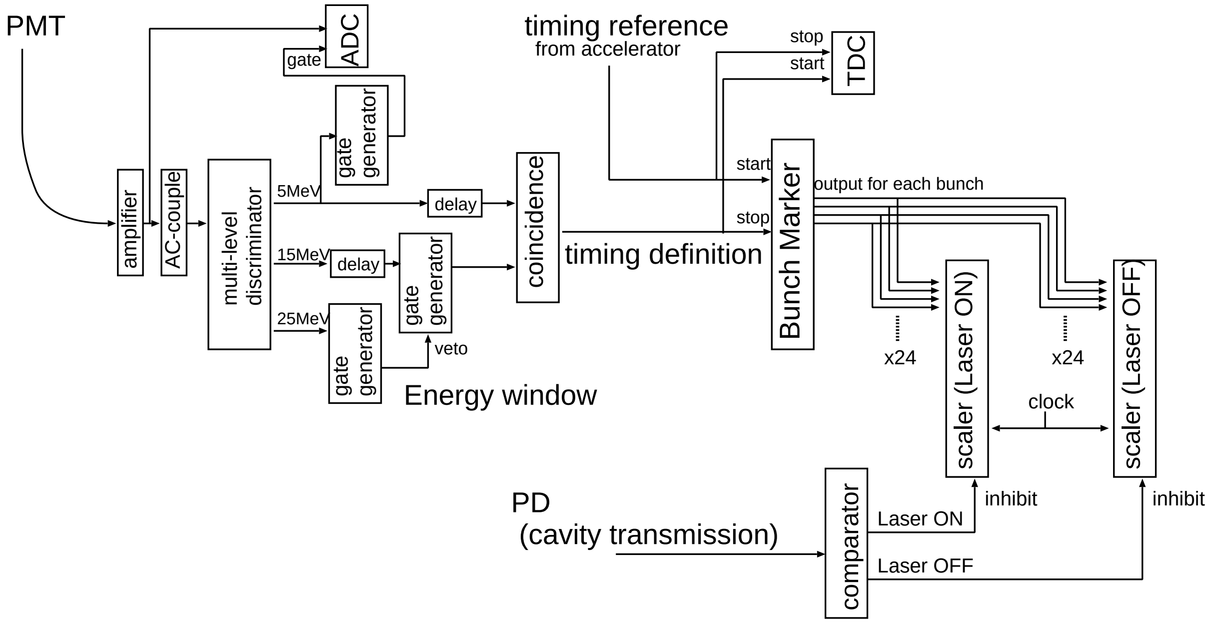

Figure 5.1: Schematic diagram of the readout circuits for the multi-bunch experiment. In the first stage, the energy of each event is measured by a set of discriminator, and the signal in 15-25 MeV range is passed to the subsequent stage with a more accurate timing produced by the 5 MeV discriminator. In the second stage, Bunch Marker identifies the bunch number based on the time difference between the event timing and the beam revolution signal given from the accelerator. Signals from different bunches are counted individually by two sets of 24 channel scalers.

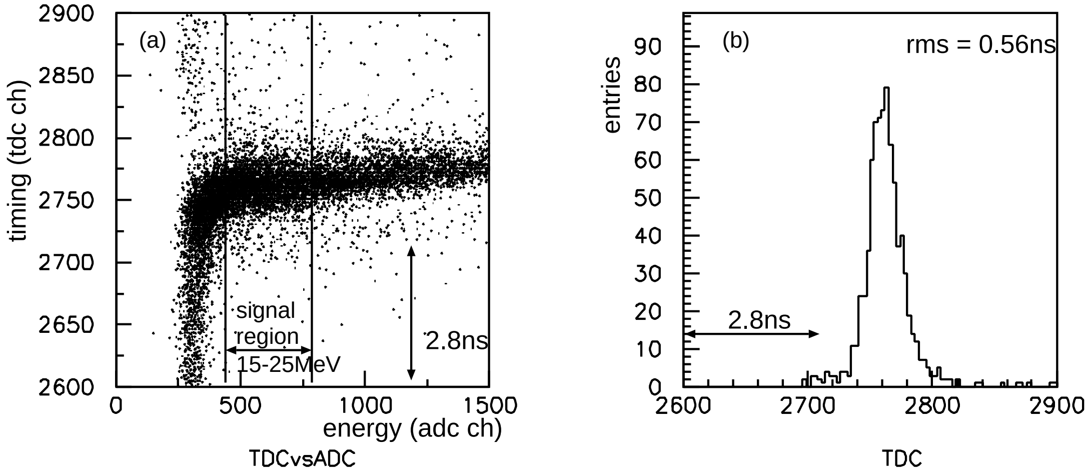

Figure 5.2: Estimation of the timing resolution. The energy and the timing were measured using the background events in the single bunch mode. (a) The correlation between the energy and detected timing. (b) The distribution of the detected timing for the events in the signal energy range.

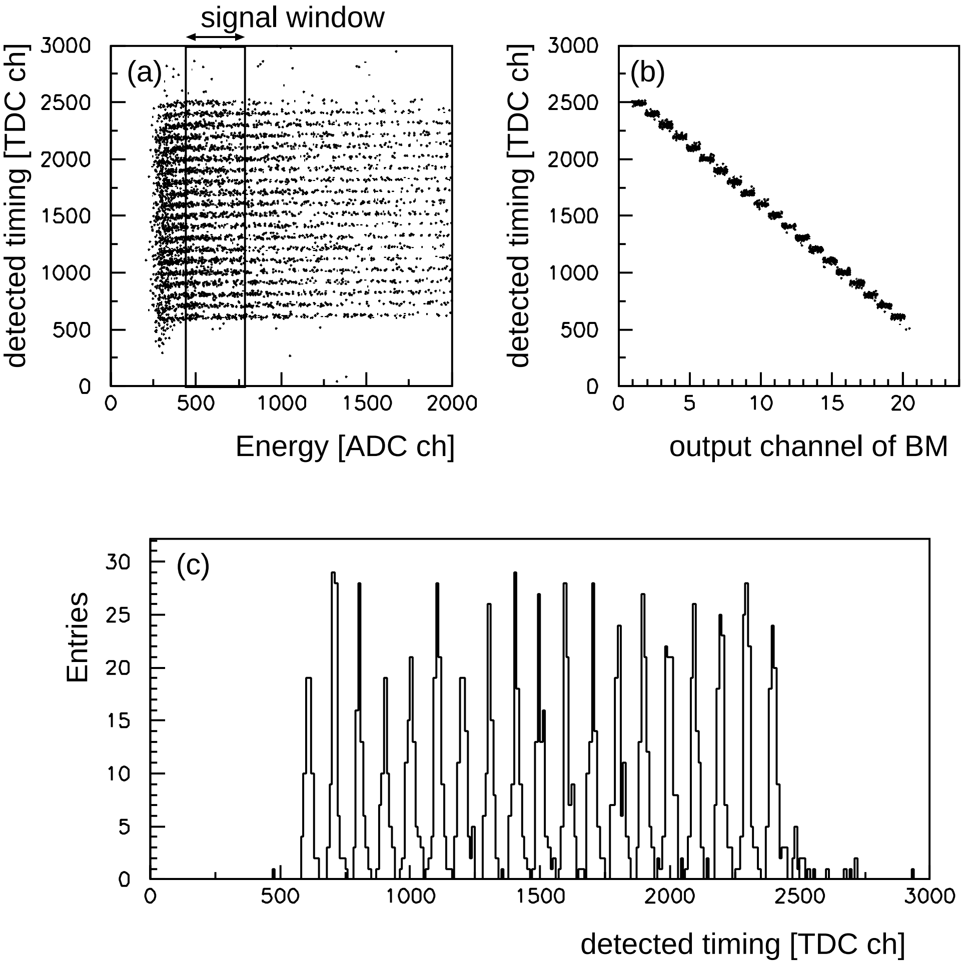

Figure 5.3: Performance of the modified circuits for the multi-bunch measurement. (a): Energy and timing correlation obtained by the background events in the multi-bunch mode. There can be seen 20 bands of events in the plot, corresponding to each bunch in the train. (b): The relation between the signal timing and the output channel of the Bunch Marker. (c): Timing spectrum of the events in the signal window (15-25 MeV).

5.2.2 Analysis procedure

We did two types of analysis for the data of the multi-bunch beam: a bunch-individual analysis and a bunch-combined analysis. In the bunch-individual analysis, data for each bunch in the train was treated separately. The data in each channel of the scalers were individually normalized to a counting rate per unit time and unit beam current (Hz/mA) and the laser "OFF" rate was subtracted from the laser "ON" rate. The resultant value, the signal count rate, was then plotted as a function of the laserwire position for each bunch of the beam. Hence, we obtain 24 beam profiles for single scan. The bunch-to-bunch differences can be discussed with such data.

In the bunch-combined analysis, events were counted together regardless of the bunch identification, just like a single bunch measurement. The count rate was normalized by the beam current (Hz/mA), and the background contribution was statistically subtracted. Then it was plotted as a function of the laserwire position. This is called as a projected beam profile of a multi-bunch beam, a beam profile averaged over the bunch intensity.

Figure 5.4 is an example of the beam profile obtained by the combined analysis. In the bunch-individual analysis, 24 of similar profiles but about 1/20 of peak height were obtained. The solid line is a Gaussian fit to the data points. From this fit, we extracted three quantities; the height (the maximum signal count rate), the width (the measured beam width σ_{meas}), and the central position (x_p, y_p). Among those, σ_{meas} is of our main interest, but the other two quantities are also useful to monitor the stability of the beam.

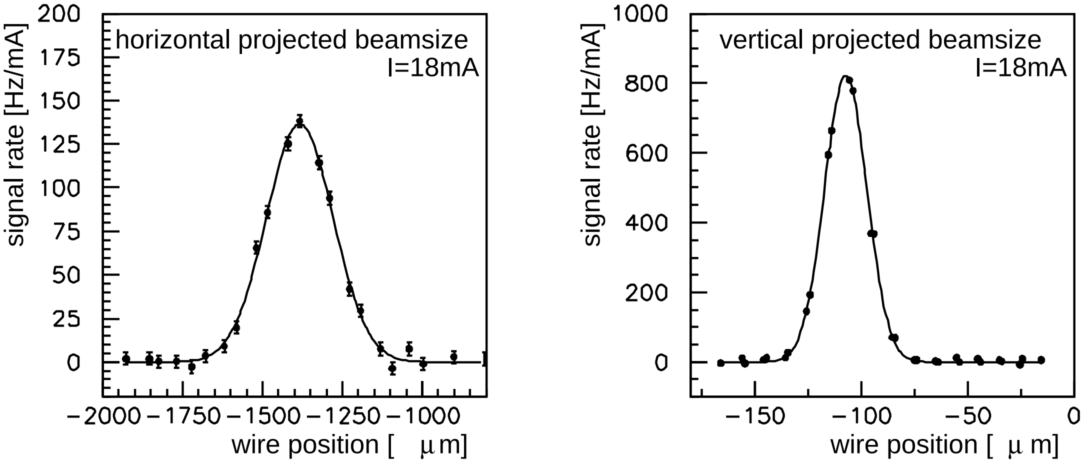

Figure 5.4: Example of the combined profile of the multi-bunch beam. The measured horizontal (left) and vertical (right) profiles are shown with the fit results.

5.3 First systematic emittance measurement (Run 1)

This experiment was performed in December 2002. The purpose of this experiment was to confirm the realization of small emittances in the multi-bunch mode similar to those in the single-bunch mode. A multi-bunch (20-bunches) beam was stored in the ring, and diagnosed by the laserwire monitor. The scans were made both horizontally and vertically,

Table 5.2: Summary of bunch-dependence of the beam width σ_{meas} measurements in the multi-bunch mode.

total current (mA)	direction	$< \sigma_{meas} >$ (μm)	$< \delta\sigma_{meas} >$ (μm)	χ^2/ν	$\Delta\sigma_{bunch}$ (μm)
1.88±0.22	horizontal	89.8	10.14	17.03/17	10.15
1.73±0.08	vertical	8.716	0.40	14.38/17	0.370
4.20±0.69	horizontal	94.4	9.62	13.36/17	8.53
4.82±0.50	vertical	9.16	0.36	22.08/17	0.409
8.54±1.56	horizontal	100.1	7.85	10.95/17	6.30
9.78±0.78	vertical	9.45	0.37	23.25/17	0.437
18.44±0.69	horizontal	104.5	8.16	26.83/17	10.25
18.77±1.47	vertical	9.95	0.30	18.21/17	0.310
18.75±0.79	vertical	9.94	0.20	53.55/17	0.350

changing the total beam current up to about 20mA. The measurements of the momentum dispersions at the laserwire position, and of the beta function were also performed.

5.3.1 Results

Bunch dependence

We first show the results of the bunch-individual analysis. Figure 5.5∼5.8 show examples of such results; they are all vertical measurements with different intensities. Figure 5.9∼5.12 are the corresponding results for the horizontal measurements. In each figure, (a) the peak height, (b) the peak position (x_p, y_p) and (c) the peak width ($\sigma_{meas}^{(x,y)}$) are shown as a function of the bunch number. The solid line in (c) is the width averaged over all bunches. As can be seen, there is no large bunch-to-bunch dependence either in the peak position or the width.

We checked all data, and concluded that there was no significant bunch dependence in the transverse direction [1] of the beam. In order to quantify the statement above, we calculated the average of σ_{meas} weighted by its error, and the error of the average itself. The results are listed in the 3rd and 4th columns in Table 5.2. The 5th and 6th columns are the chi-square per degree of freedom (χ^2/ν) and the rescaled error, *i.e.* $\Delta\sigma_{bunch} =< \delta\sigma_{meas} > \sqrt{\chi^2/\nu}$. We consider the bigger of $< \delta\sigma_{meas} >$ and $\Delta\sigma_{bunch}$ to be a measure of the bunch-to-bunch variation in σ_{meas}. As can be seen, the fractional variations are about 5% for the vertical, and about 10% for the horizontal.

---

[1] An oscillation in the longitudinal direction has been observed in multi-bunch operation, which strongly depends on the bunch number. [42]

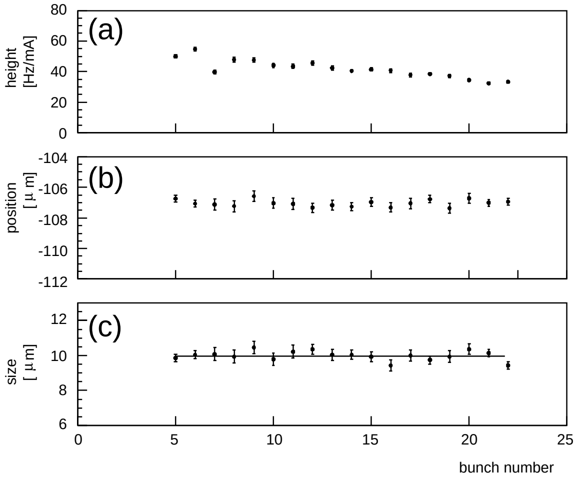

Figure 5.5: Bunch dependence of the 20-bunch beam (vertical, 18.8mA). (a) the peak height ; (b) the peak position y_p ; (c) the peak width $\sigma^{(y)}_{meas}$. The solid line is the width averaged over all bunches.

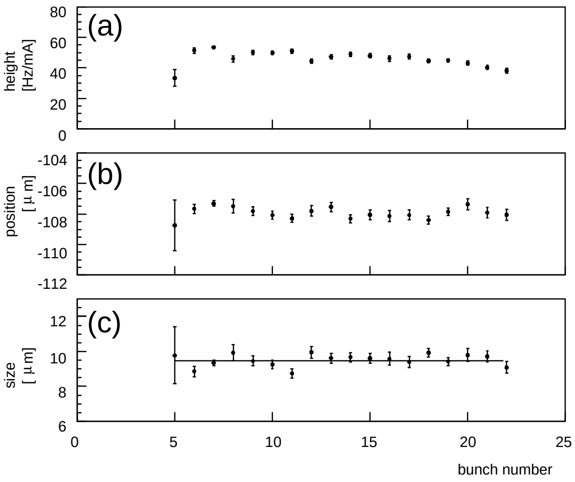

Figure 5.6: Bunch dependence of the 20-bunch beam (vertical, 9.8mA). (a) the peak height ; (b) the peak position y_p ; (c) the peak width $\sigma^{(y)}_{meas}$. The solid line is the width averaged over all bunches.

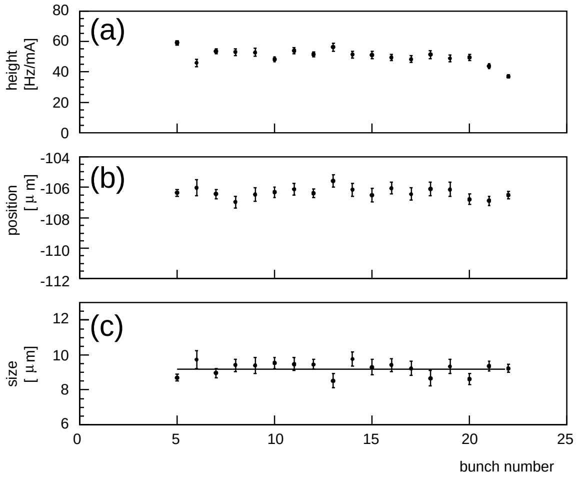

Figure 5.7: Bunch dependence of the 20-bunch beam (vertical, 4.8mA). (a) the peak height ; (b) the peak position y_p ; (c) the peak width $\sigma^{(y)}_{meas}$. The solid line is the width averaged over all bunches.

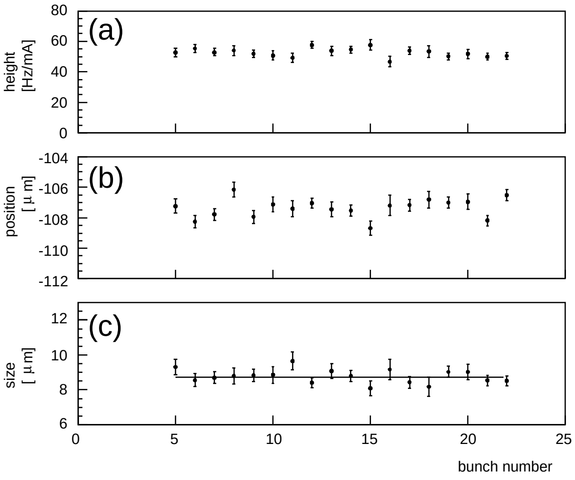

Figure 5.8: Bunch dependence of the 20-bunch beam (vertical, 1.7mA). (a) the peak height ; (b) the peak position y_p ; (c) the peak width $\sigma^{(y)}_{meas}$. The solid line is the width averaged over all bunches.

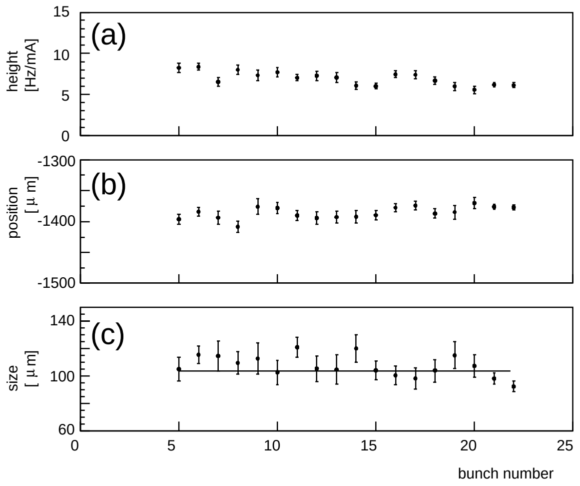

Figure 5.9: Bunch dependence of the 20-bunch beam (horizontal, 18.4mA). (a) the peak height ; (b) the peak position x_p ; (c) the peak width $\sigma^{(x)}_{meas}$. The solid line is the width averaged over all bunches.

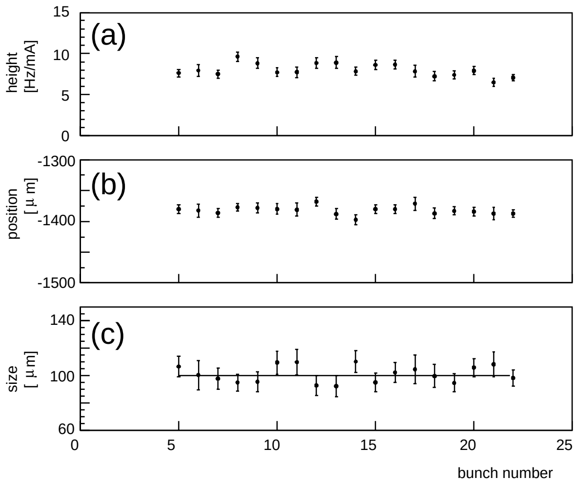

Figure 5.10: Bunch dependence of the 20-bunch beam (horizontal, 8.5mA). (a) the peak height ; (b) the peak position x_p ; (c) the peak width $\sigma^{(x)}_{meas}$. The solid line is the width averaged over all bunches.

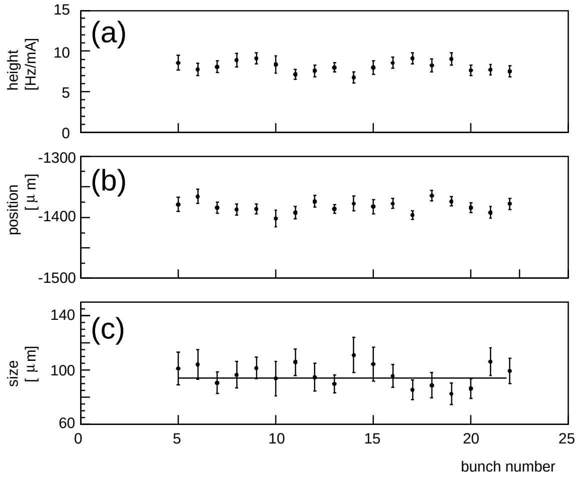

Figure 5.11: Bunch dependence of the 20-bunch beam (horizontal, 4.2mA). (a) the peak height ; (b) the peak position x_p ; (c) the peak width $\sigma^{(x)}_{meas}$. The solid line is the width averaged over all bunches.

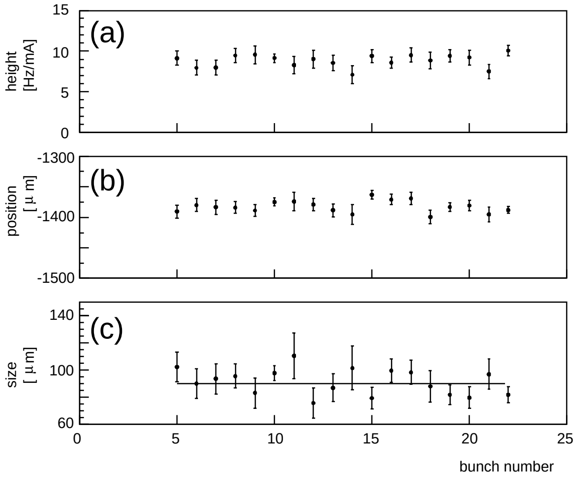

Figure 5.12: Bunch dependence of the 20-bunch beam (horizontal, 1.9mA). (a) the peak height ; (b)the peak position x_p ; (c) the peak width $\sigma^{(x)}_{meas}$. The solid line is the width averaged over all bunches.

Table 5.3: Results of the combined analysis (vertical)

intensity (mA) average±rms	total fill	peak size σ_{meas} (μm)	χ^2/ν	emittance ($\times 10^{-11}$ rad)
18.77±1.47	14	9.96 ± 0.06 (± 0.11)	77.83/27	1.56±0.51(±0.91)
9.78±0.78	2	9.50 ± 0.07 (± 0.08)	27.18/17	1.35±0.35(±0.75)
4.82±0.50	1	9.25 ± 0.07 (± 0.11)	101.4/20	1.24±0.47(±0.77)
1.73±0.08	1	8.80 ± 0.06	7.34/18	1.05±0.24(±0.58)
18.75±0.79	12	9.86 ± 0.07 (± 0.11)	52.92/21	1.51±0.50(±0.89)

Table 5.4: Results of the combined analysis (horizontal)

intensity (mA) average±rms	total fill	peak size σ_{meas} (μm)	χ^2/ν	emittance (nm rad)
18.44±0.69	22	105.2 ± 1.98	17.99/19	1.39±0.05(±0.23)
8.54±1.56	2	102.3 ± 2.04	23.17/19	1.31±0.05(±0.22)
4.20±0.69	1	96.39 ± 2.12	28.41/15	1.16±0.05(±0.19)
1.88±0.22	1	93.07 ± 2.30	23.80/17	1.16±0.05(±0.18)

Table 5.5: Results of the beta function and dispersion measurements.

collision point	direction	beta function (m)	dispersion (mm)
horizontal wire	x	9.81 ± 1.25	N/A
	y	4.32 ± 0.20	1.83 ± 0.31
vertical wire	x	7.83 ± 1.25	2.00 ± 0.66
	y	4.89 ± 0.20	N/A

Current dependence

Next, we consider the current dependence of these emittances. Since no bunch-to-bunch difference is found, we use the combined data of all bunches in this discussion. The measured projected beam size (σ_{meas}) is plotted as a function of the beam current in Figure 5.13 and 5.14 for the vertical and horizontal direction, respectively. They are also listed in Table 5.3 and Table 5.4. The beta function and the dispersion function were measured by the same method as those explained in Sec. 4.2.3 and 4.2.4 , and the obtained results are summarized in Table 5.5. The calculated emittance values are also shown in the right side ordinate in Figure 5.13 and 5.14.

The vertical (horizontal) emittance was found to be in the range of 10∼16 pm·rad (1∼1.5 nm·rad) in this beam intensity. The ratio of horizontal to vertical emittance was about 100:1.

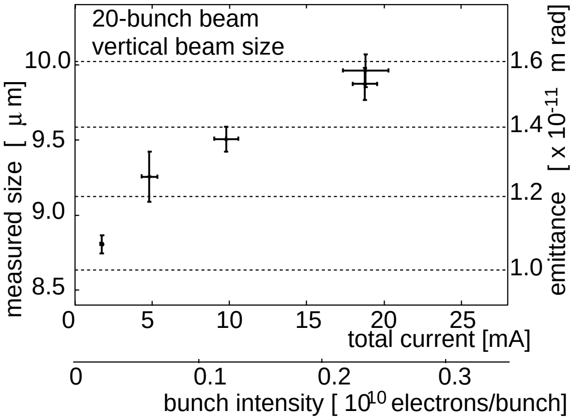

Figure 5.13: Vertical emittance of the 20-bunch beam vs the electron current.

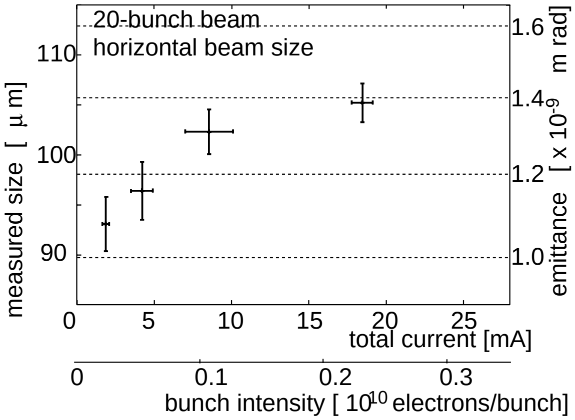

Figure 5.14: Horizontal emittance of the 20-bunch beam vs the electron current.

5.3.2 Discussions and Summary

First of all, the vertical emittance was found to be in the range of 10∼20 pm·rad: this value is somewhat larger than the target value of 11 pm·rad, but it certainly is an important milestone to our goal. The maximum bunch intensity achieved in this experiment was around 0.22×10^{10} [e/bunch], still smaller than that measured in the single bunch case. We observed about factor 1.5 enhancement of the vertical emittance at this intensity. The current dependence seems stronger than that measured in Chapter 4. A comment is appropriate here about the observed current dependence. An increase of vacuum pressure was observed at arc sections when the ring was filled with a high current beam. This was due to a huge synchrotron radiation from the multi-bunch beam whose total current was more than 10 times higher than that of the single bunch. This effect might have enhanced the current dependence. More studies and/or improvement of the vacuum pressure will be needed to understand this observation.

The measurement results show that there is no serious bunch-to-bunch dependence in the emittance. Because of the small dispersion, the contribution of the longitudinal oscillation to the transverse beam size is small at the collision point of the laserwire. We could measure transverse direction without contaminated by the longitudinal motion noted in footnote 1.

5.4 Comparison between the single and multi-bunch modes (Run 2 and 3)

After the run 1 ended, ATF succeeded in further reducing the vertical emittance in the single bunch mode as already explained in Chapter 4. It should be checked that the smallest emittance could also be realized in the multi-bunch mode. This experiment was performed in June 2003, a month after the achievement of the smallest emittance in the single bunch mode. In this experiment, we focused only on the vertical direction. After a careful tuning of the damping ring, we measured the vertical beam size in the multi-bunch

Table 5.6: Results of the combined multi-bunch beam size measurements (run 2).

beam current (mA)	measured width (μm)	χ^2/ndf	emittance (pm rad)
7.5±1.3	7.57±0.09(±0.22)	111.7/17	7.44±0.98(±1.33)
4.4±0.6	7.31±0.08(±0.10)	28.8/19	6.31±0.43(±0.90)
3.0±0.3	7.54±0.10(±0.10)	18.1/16	7.31±0.44(±1.00)
7.8±1.2	7.49±0.07(±0.11)	27.1/12	7.09±0.48(±1.00)
4.9±0.6	7.47±0.08(±0.08)	16.5/14	7.00±0.35(±0.93)
3.3±0.3	7.18±0.08(±0.10)	20.0/14	5.75±0.42(±0.84)
1.6±0.1	7.36±0.11(±0.11)	13.8/13	6.52±0.47(±0.94)

Table 5.7: Results of the single-bunch beam size measurements (run 3).

beam current (mA)	measured width (μm)	χ^2/ndf	emittance (pm rad)
0.50±0.06	7.16±0.21(±0.21)	7.5/15	5.67±0.88(±1.14)
0.31±0.02	7.21±0.22(±0.22)	14.6/15	5.88±0.93(±1.19)
0.80±0.12	7.14±0.18(±0.19)	15.2/14	5.59±0.80(±1.06)
0.51±0.05	7.39±0.23(±0.29)	24.8/15	6.65±1.26(±1.50)
0.35±0.03	6.98±0.27(±0.27)	12.2/13	4.93±1.11(±1.28)
0.13±0.01	6.95±0.32(±0.38)	17.1/12	4.80±1.55(±1.67)

mode (run 2). The total beam current was varied up to 8mA, the effective bunch number in the ring was about 15. Immediately after this run, we switched the operation to the single-bunch mode. The vertical beam size of a single bunch beam was measured in the same range of bunch intensity (run 3). The beta function was also measured at the same time.

5.4.1 Result

We extracted the combined beam size for all data. They are listed in Table 5.6 and 5.7 for the multi-bunch mode and single-bunch mode, respectively. The total current, the measured size (σ_{meas}), the reduced χ^2 (χ^2/ν) and the calculated emittance are listed. To include the effect of unknown systematic effects, we enlarged the errors of all data points uniformly so that χ^2/ν became unit. The errors on σ_{meas} and emittance after the treatment are listed in the parentheses.

Those results are plotted in Figure 5.15. For the multi-bunch case, the bunch intensity ([mA/bunch]) was calculated simply dividing the total current by 15 (the effective number of bunches). Unfortunately, the region of the beam current measured in this experiment was too narrow to discuss about the current dependence.

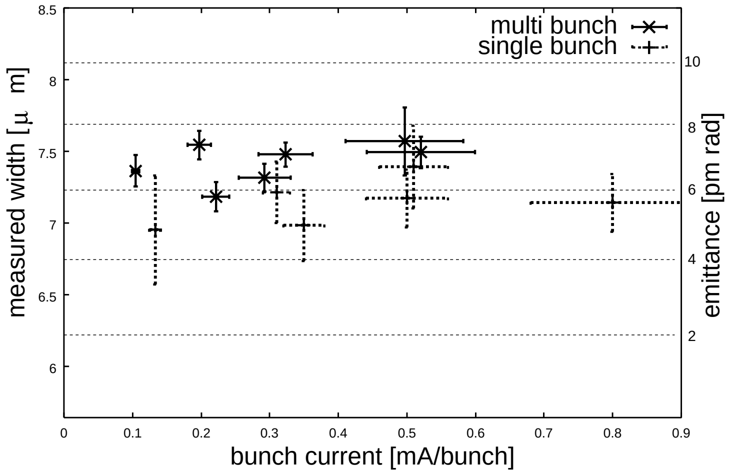

Figure 5.15: Vertical beam size of the multi-bunch and single-bunch mode. The measured vertical beam sizes (σ_{meas}) of two operational modes, the multi-bunch mode (solid) and the single-bunch mode (dashed) are compared as a function of bunch current (beam current per bunch). The corresponding emittance values are indicated on the right-side ordinate.

5.4.2 Discussions and Summary

It was confirmed that the vertical emittance in the multi-bunch mode could be reduced to the similar level as that in the single-bunch mode. In both modes, the measured vertical beam size was 7∼7.5 μm, which corresponds to about 6 pm·rad, and no large difference was seen when the two modes were switched consecutively.

Although the stored beam intensity was still about 20% of the target value, this observation is an important milestone toward our goal. The confirmation with a high-intensity multi-bunch beam in a near future is awaited.

5.5 Pressure dependence study (Run 4)

So far, no serious multi-bunch beam instabilities have been observed in the transverse motion. In principle, however, there are several mechanisms that may make the multi-bunch unstable. One of the most serious effects is a so-called fast-beam-ion instability. A simple explanation of this mechanism is as follows; some of the residual gas near the beam orbit are ionized by the beam. Since the ions have opposite electric charge to the electron beam, they are pulled to the center of the beam. Those ions kick electrons in the following bunch, resulting in the transverse oscillation of the beam. The beam orbit along the train is modulated by the motion of the ions. Since the number of the ions increases toward the end of the bunch train, the amplitude of the oscillation grows accordingly. The oscillation frequency of the ions is determined by its mass (gas species) and the restoring force (the beam size and the intensity). The growth rate of oscillation amplitude along the train depends also on the number of ions (vacuum pressure and beam intensity).

Although this effect has been observed in several facilities around the world, ([43],[44] and [45]), the quantitative understanding has yet to be established. In realizing the linear colliders, where the stability of high-intensity low-emittance multi-bunch beam is critical, this effect remains to be one of the unknown risk factor.

We have started the studies on the pressure dependent dynamics of the multi-bunch beam at ATF. In this section, we describe the observation of the bunch-to-bunch profile difference in the ATF damping ring.

5.5.1 Data taking

This measurement was performed on June 13, 2003. In order to examine the ion-induced instabilities, we increased on purpose the vacuum pressure of the damping ring. We took data under three different pressure conditions: normal, ion pumps turned off in one arc section (one arc), ion pumps turned off in both arc sections (both arc). When the pumps were turned off, the pressure in the section increased about one order of magnitude immediately.

A multi-bunch beam was stored in the damping ring, and scanned by the laserwire monitor in the vertical direction. The average pressure of the damping ring and the beam current were monitored during the measurement.

5.5.2 Result

Figure 5.16 and 5.17 show examples of the beam profiles for each bunch in the conditions of normal and increased pressure (one arc), respectively. In the cases of normal condition, no large bunch-to-bunch difference was seen. On the other hand in the case of the increased pressure, a clear bunch dependence was observed, indicating a blow-up toward the end of the train.

The obtained profiles of each bunch were fitted by a Gaussian function. The center position of the profile, the rms width, and the beam intensity (the area of the resultant function) were extracted from the fitting. Those results for various conditions (three pressure conditions and two beam currents) are shown in Figure 5.18 $\sim$ 5.23.

In the cases of normal condition, no bunch dependence was seen even with a high intensity beam (Figure 5.18 and 5.19). However, in the cases of ion pumps in one arc section turned off, the beam size clearly increased along the train, and the growth rate depended on the beam intensity. In the last cases, all ion pumps in both arc sections were turned off. A fast beam size blow-up was seen even in the current of 5.2 mA, and the growth rate seemed to have increased further.

5.5.3 Discussion and Summary

A pressure dependence of the multi-bunch beam profile was studied. Clear bunch number dependence was observed in the runs with an increased vacuum pressure.

Two qualitative natures were observed:

- The vertical beam size (or an oscillation amplitude) increased along the train (head to tail).

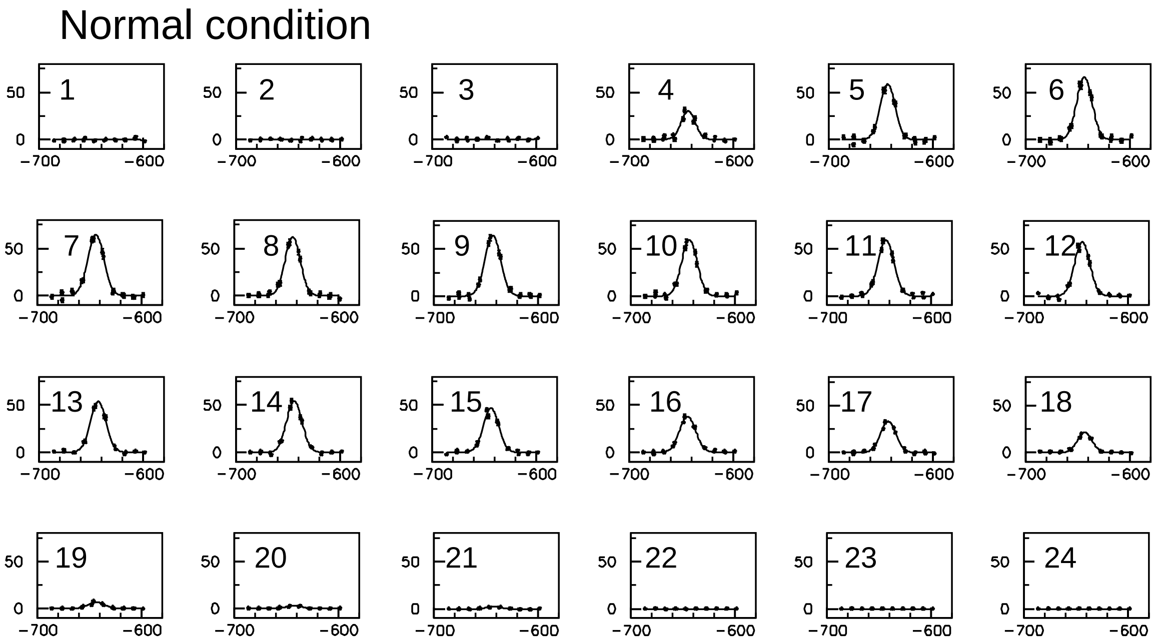

Figure 5.16: Beam profile for each bunch (normal pressure). The beam current was 7.7mA, and the average pressure was 6×10^{-7}Pa.

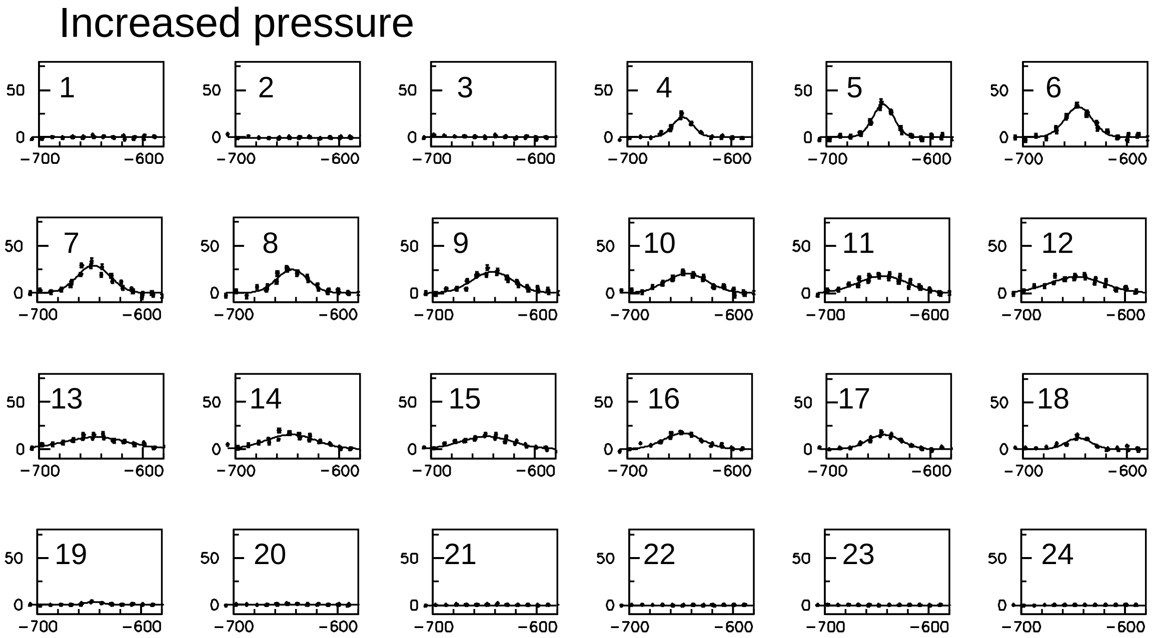

Figure 5.17: Beam profile for each bunch (increased pressure). The beam current was 6.4mA, and the average pressure was 3×10^{-6}Pa.

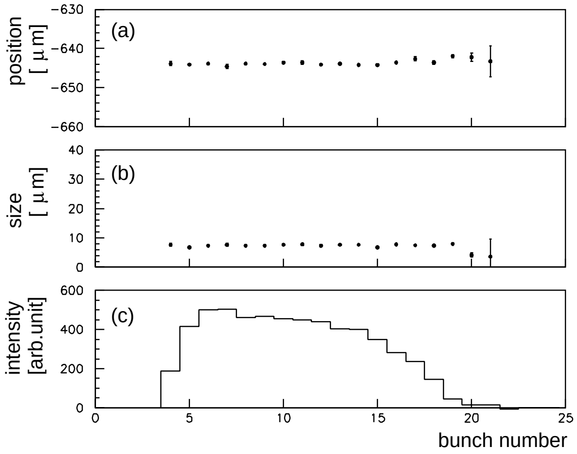

Figure 5.18: Bunch dependence (normal pressure, 9.1 mA)

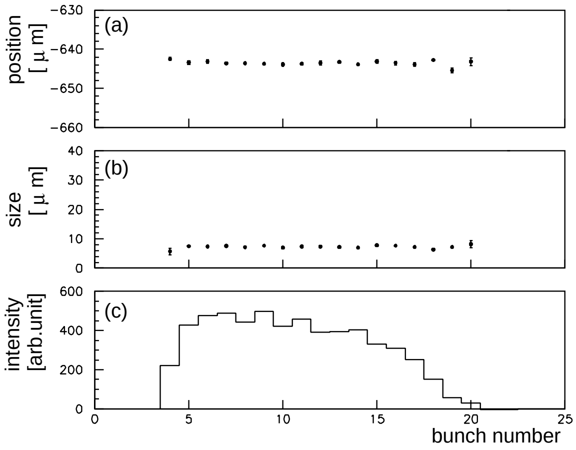

Figure 5.19: Bunch dependence (normal pressure, 6.5 mA)

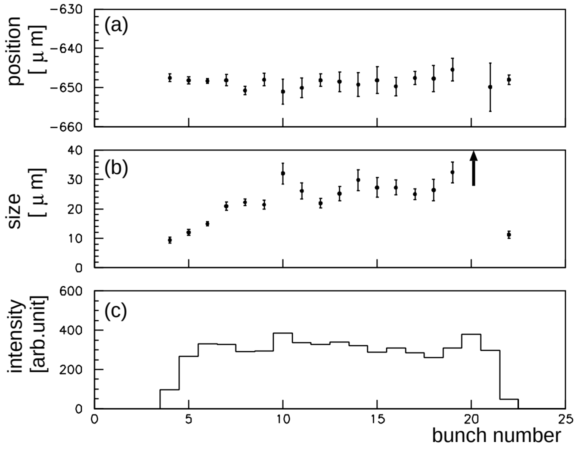

Figure 5.20: Bunch dependence (one arc, 10.1 mA, 5.0×10^{-6}Pa)

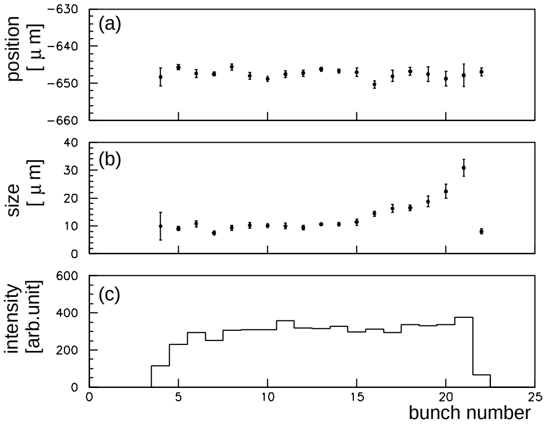

Figure 5.21: Bunch dependence (one arc, 6.7 mA, 4.0×10^{-6}Pa)

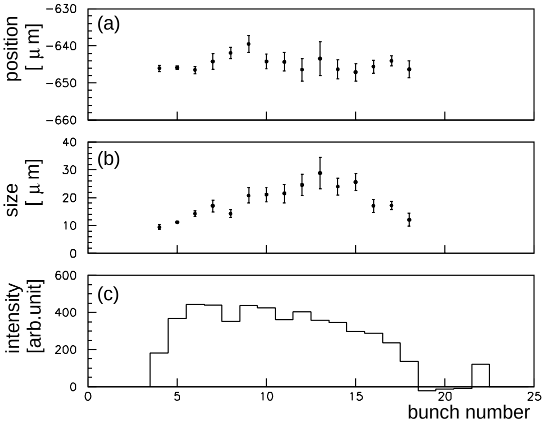

Figure 5.22: Bunch dependence (both arc, 7.9 mA, 6.0×10^{-6}Pa)

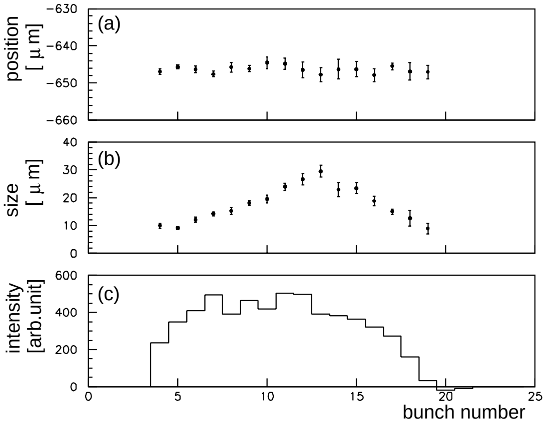

Figure 5.23: Bunch dependence (both arc, 5.2 mA, 5.6×10^{-6}Pa)

- The growth rate depends on the beam intensity and the vacuum pressure.

These results agree with the expectation of the fast-beam-ion instability, at least qualitatively.

Several improvements will be necessary to make the discussion quantitative. First of all, the intensity variation in a train should be reduced within a few %. In reality, the intensity distribution in the train varied in each fill. Stable and efficient injection of the multi-bunch beam into the damping ring is required. Second, a longitudinal motion of the bunch was observed by the streak camera. The amplitude of the longitudinal oscillation was also found to grow along the train. If there was a much larger momentum spread than those measured under the normal pressure, it would have affected the transverse motion.

As a final comment in this section, we like to point out the following fact. The laserwire measures an averaged beam of many revolutions. Thus, a transverse oscillation of the beam position can imitate an increase in the beam size. With the laserwire monitor alone, it can not be distinguished whether the measured beam size growth is a real beam size growth or an increase of a transverse oscillation. In order to measure the transverse oscillation, a beam position monitor with multi-bunch detection circuits or a spectrum analysis of a BPM pick-up signal will be useful.

Chapter 6

Conclusion

We described the studies of a low emittance electron beam in the ATF damping ring. ATF is a test accelerator built in KEK. Its goal is to experimentally prove the production of the low emittance beam required for future linear colliders.

To diagnose its ultra-low emittance beam realized in the damping ring, a unique instrument called a laserwire beam profile monitor was developed and upgraded. This monitor works as follows. A thin wire of photon (laserwire) is produced in a Fabry-Perot optical cavity which is externally excited by a CW laser. The optical cavity is precisely controlled to keep the resonance condition. By scanning the laserwire across an electron beam while measuring the flux of the Compton scattering signal rate, a transverse profile of the electron beam is obtained. The salient feature of this monitor is its reliability and non-invasiveness of the measurement. Two orthogonal laserwires measure the beam sizes of two transverse directions. In 2000, the laserwire monitor (horizontal only) was installed in the north straight section of the ATF damping ring, and made its first successful measurement of the vertical beam emittance. In 2002, we upgraded the system in several aspects. We improved its resolution by reducing the laserwire width, and shortened data acquisition time by increasing the effective intensity of the laserwire. We installed a vertical laserwire system in addition to the horizontal one. The signal detection scheme was also modified to separately measure the beam profiles of each bunch in a multi-bunch train.

Intending to prove the achievement of an ultra-low emittance in the ATF damping ring, and to understand the mechanism of intensity-dependent emittance growth, we performed a series of systematic studies. We began the measurement with the single bunch beam. Actually we measured the four dimensional beam properties, (the transverse emittances, bunch length, and momentum spread), and their intensity dependence under various ring conditions. Our main conclusion from the study are as follows. In the case of a well-tuned condition, the vertical emittance was found to reach as small as 4 pm·rad in the zero current limit, and grow by about factor 1.5 at the intensity of 10^{10}. The result proved that a low emittance beam required for the linear colliders has been produced at least in the single bunch mode. As to the intensity dependence, all observed quantities showed, more or less, such dependences. First of all, the momentum spread was found to show an intensity dependence, but its strength (the slope of the intensity dependence) became weaker as the vertical emittance was enlarged. Second, both horizontal and vertical emittances showed intensity dependences; their strength were similar in magnitude. The bunch length was also found to depend on the beam intensity, but the slope seemed to be independent of the bunch volume. The bunch lengthening can be understood naively by the effect of the wake field. On the other hand, the emittances and momentum spread are determined by the intra-beam scattering. In order to understand the mechanism of these intensity dependences, we developed a beam simulation code. Actually, the SAD code was modified to include the effect of longitudinal wake field in addition to the intra-beam scattering. The impedance of the beam line was estimated from the bunch lengthening. The overall nature of the emittance, bunch length and momentum spread under the various conditions of the ring tuning seems to have no serious disagreement with this model calculation.

In the multi-bunch operational mode, a train with 20-bunches spaced 2.8 nsec interval was filled in the damping ring. The transverse emittances of each bunch were diagnosed by the laserwire monitor. It proved that a similar small emittance as the single bunch mode was realized even in the multi-bunch mode. No large bunch-to-bunch differences were seen. Although the bunch intensity of the stored beam was still much lower than our target, the observation is a promising milestone toward the goal. To investigate the effect of instabilities caused by the ions in the beam, vacuum pressure dependence of the beam size was studied. A clear beam blow-up along the train was seen under the condition of an increased pressure, suggesting the fast-beam-ion instability. This effect may limit the performance of the vertical emittance of the multi-bunch mode in a high intensity region.

The attained transverse emittances are plotted in Figure 6.1 with our target. Although the horizontal emittance is determined from the ring design, the vertical emittance can be reduced by the precise alignment and/or the beam tuning. It shows that we succeeded in reducing the vertical emittance to a half of the initial target value and reached the requirement of GLC at the design bunch intensity. In the multi-bunch mode, the vertical emittance reached our initial design in run 1. And was further reduced later, in run 2 at a lower intensity. We hope we can satisfy the GLC requirement even in the multi-bunch mode with the design intensity.

Basically the main study goal in the ATF damping ring, the low-emittance beam production, has been achieved successfully. In the future, the first to be proved in ATF should be the production of a required emittance with a high current (design bunch intensity) in the multi-bunch mode. Stable and efficient injection to (and extraction from) the damping ring have to be realized. Energy compensation in the linac have to be tuned to stabilize the multi-bunch injection. The extraction kicker system needs some modifications to extract all bunches in the train in the same orbit. The emittance measurement should be performed in the extraction line. The multi-bunch instabilities in the ring have to be studied by the laserwire and other instruments. The future linear colliders require further reduction in the damping time to achieve a high repetition rate and thus a high luminosity. This can be achieved with wiggler magnets in the ring; the role of these magnets is to shorten the damping time by additional synchrotron radiation. In the experiments presented in this theses, the wiggler magnets were being installed but never used. The magnets may become a new x-y coupling source. Thus the emittance studies must be repeated. We plan to start soon the wiggler operation.

Concluding this thesis, the successful beam development in the ATF damping ring is an important milestone for realizing future linear colliders. And the laserwire monitor has played an crucial role in all the ATF emittance studies.

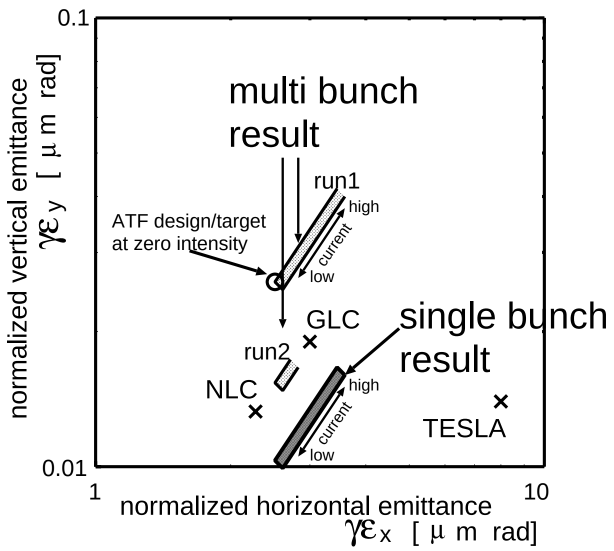

Figure 6.1: Normalized emittance of two transverse directions measured in our experiment. The measured normalized emittance are shown by the rectangular boxes for the single-bunch and multi-bunch modes. The design/target value of the ATF damping ring and the required values for several planned linear colliders are also shown. The vertical emittance smaller than the target was achieved in the single bunch mode. We reached our target value also in the multi-bunch mode.

Appendix A

Beam Dynamics

We give a brief description on the beam dynamics of the electron beam in a ring related to the studies discussed in this thesis.

A.1 Linear beam dynamics in a circular accelerator

Detailed explanations of this section is found in basic textbooks (for example [46],[47] and [48]).

A.1.1 Betatron motion

When a charged particle beam is stored in a storage ring, an individual particle in the beam has a finite transverse motion with respect to the central orbit. It is called a betatron motion, the oscillation determined by the potential of the magnetic field provided by accelerator components. Figure A.1 illustrates the betatron motion together with the coordinate system used in this appendix.

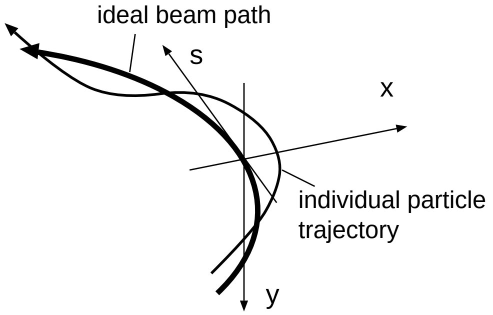

Figure A.1: Coordinate system. The individual particle oscillates around the ideal beam path.

The equation of motion along the beam trajectory (s) can be expressed as

$$\frac{d^2u}{ds^2} + K_u(s)u = \frac{1}{\rho} \cdot \frac{\Delta p}{p_0} \qquad (u = x, y) \tag{A.1}$$

$$K_x(s) = k(s) + \frac{1}{\rho(s)^2} \quad , \quad K_y(s) = -k(s) \quad , \tag{A.2}$$

where ρ represents the radius of curvature of the trajectory, p_0 the nominal momentum, and Δp the difference of the momentum from p_0. $K_u(s)$ is determined by the strength of magnets in the beam line, and is a periodic functions with period L.

First, we consider the case $\Delta p/p = 0$ (particle with ideal energy). The equation of motion now reads, for both x and y,

$$\frac{d^2u}{ds^2} + K_u(s)u \quad = \quad 0 \quad \text{with} \quad K_u(s+L) = K_u(s) \quad . \tag{A.3}$$

This differential equation is called *Hill's* equation. It can be understood as a harmonic-oscillator of which the restoring force periodically changes. The solution can be written in the forms of

$$u(s) \quad = \quad A\sqrt{\beta(s)}\cos\left(\psi(s)+\psi_0\right) \tag{A.4}$$

$$u'(s) \quad = \quad -\frac{A}{\sqrt{\beta(s)}}\left[\alpha(s)\cos\left(\psi(s)+\psi_0\right)+\sin\left(\psi(s)+\psi_0\right)\right] \quad , \tag{A.5}$$

where A and ψ_0 are constants, and subsidiary relations

$$\alpha(s) \quad \equiv \quad -\frac{\beta'(s)}{2} \tag{A.6}$$

$$2\beta\beta'' - \beta'^2 + 4\beta^2 K \quad = \quad 4 \tag{A.7}$$

$$\frac{d\psi(s)}{ds} \quad = \quad \frac{1}{\beta(s)} \quad , \tag{A.8}$$

hold for $\alpha(s)$, $\beta(s)$ and $\psi(s)$.

There is an invariant of the motion:

$$W \quad = \quad \gamma u^2 + 2\alpha u u' + \beta u'^2 \quad = A^2 \quad = \quad \text{const.} \quad , \tag{A.9}$$

where $\gamma \equiv \frac{1+\alpha^2}{\beta}$. It is called the *Courant-Snyder* invariant (or emittance of single particle), and represents the energy of the transverse oscillation. Figure A.2 shows a trajectory in a phase space expressing a particle's transverse motion at a fixed position of the ring. Since W is an invariant, the trajectory moves on an ellipse. The area surrounded by the ellipse represents the oscillation energy of the betatron motion.

Since the energy W of many particles in equilibrium obeys the *Boltzmann* law, its distribution is given by an inverse exponent of W. Then the particle's density in the phase space is expressed by a Gauss distribution, as shown in Figure A.3.

In case of $\Delta p/p \neq 0$, we divide $u(s)$ into two;

$$u(s) \quad = \quad u_\beta(s) + \eta(s)\frac{\Delta p}{p} \quad . \tag{A.10}$$

where $u_\beta(s)$ is the betatron motion in case of $\Delta p/p = 0$, and η is a momentum depending part, called a momentum dispersion function. Then, Eq. A.1 gives the differential equation

$$\frac{d\eta^2(s)}{ds^2} + K(s)\eta(s) \quad = \quad \frac{1}{\rho(s)} \quad \text{with} \quad \eta(s+L) = \eta(s) \quad . \tag{A.11}$$

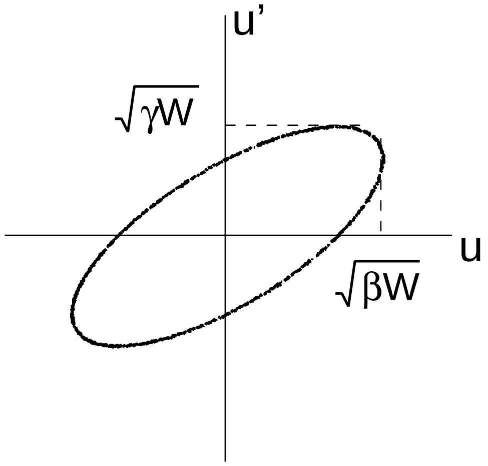

Figure A.2: Trace of a particle in the phase space.

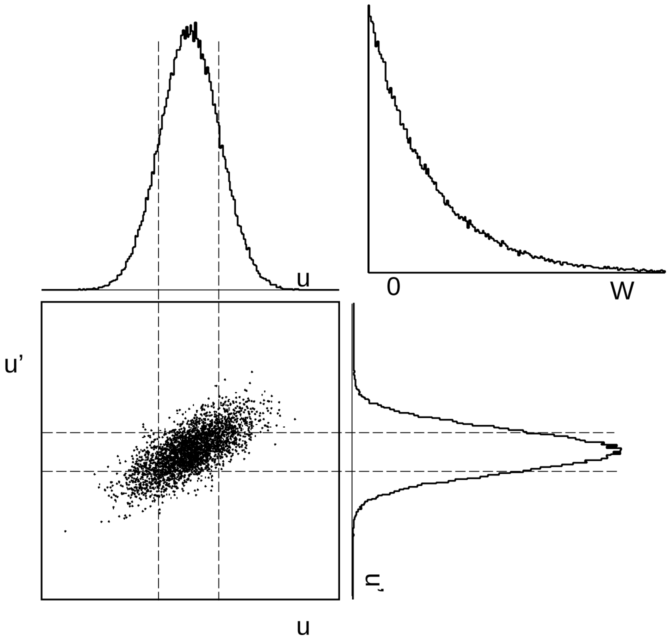

Figure A.3: Particle distribution in a phase space.

A.1.2 Radiation damping

Longitudinal motion

Figure A.4 shows an accelerating voltage (and hence the energy gain) in an RF cavity as a function of the arrival time of an electron. If the energy loss due to synchrotron radiation balances the gain in the cavity, the particle's longitudinal motion completely synchronizes to the RF frequency (synchronous particle). An electron with a higher energy generally travels along a longer path and therefore arrives late, and receives less energy (and vice versa). This works as a restoring force, and particles stably oscillate longitudinally around the synchronous condition. In addition, the energy loss due to the synchrotron radiation increases with the energy of the particle, and then it acts as a damping force. As a whole, the longitudinal motion (or energy oscillation) of particles obeys a damping oscillator equation

$$\frac{d^2\varepsilon}{dt^2} + 2\alpha_\varepsilon \frac{d\varepsilon}{dt} + \Omega^2\varepsilon = 0 \tag{A.12}$$

$$\alpha_\varepsilon = \frac{1}{2T_0}\frac{dU}{d\varepsilon} \tag{A.13}$$

$$\Omega^2 = \frac{e}{T_0}\dot{V}_0\frac{\alpha}{E_0} \quad , \tag{A.14}$$

where ε represents the particle's energy difference, T_0 the period of a revolution, U the energy loss due to the synchrotron radiation, and $\dot{V}_0$ the slope of the accelerating voltage.

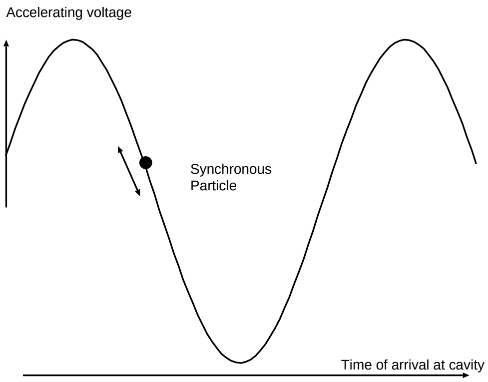

Figure A.4: Variation of accelerating voltage in an RF cavity as a function of electron arrival time.

Transverse motion

Synchrotron radiations are emitted mostly in the direction of the particle's individual motion. On the other hand, the acceleration in the RF cavity makes up their energy loss only in a certain direction, usually the longitudinal direction of the central orbit. This effectively means that the transverse component of the momentum is replaced by the longitudinal acceleration, and therefore the betatron motion damps. This mechanism is illustrated in Figure A.5.

In the vertical plane (dispersion less case), the damping rate of the betatron oscillation amplitude (A) is expressed by

$$\frac{1}{A}\frac{dA}{dt} = -\frac{U_0}{2E_0T_0} \quad . \tag{A.15}$$

In the horizontal plane, a finite dispersion changes the off-energy orbit. An energy change due to the emission of synchrotron radiations excites the betatron motion at the same time. It modifies the damping rate to,

$$\frac{1}{A}\frac{dA}{dt} = -\frac{U_0}{2E_0T_0}(1 - D) \quad , \tag{A.16}$$

where D is the dispersion function.

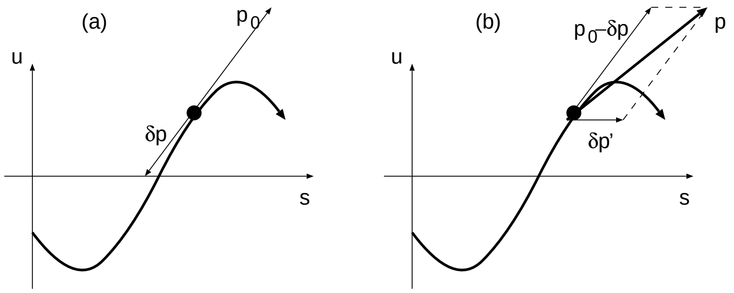

Figure A.5: Emission of an synchrotron radiation and the acceleration in the cavity.

A.1.3 Quantum excitation and equilibrium

Quantum excitation

Actual energy loss due to the synchrotron radiation occurs in a discrete energy unit of a photon. It introduces a kind of noise, resulting in a growth of the oscillation amplitude.

The growth rate of the energy spread is given

$$\Delta\left(\frac{\Delta p}{p}\right)^2 = \frac{2r_e}{3} C_q \gamma^5 \oint \frac{1}{|\rho^3|} ds \quad , \tag{A.17}$$

where $C_q = \frac{55}{32\sqrt{3}} \frac{\hbar}{mc}$. It is converted into the energy change of the transverse motion (ΔW) via the dispersion

$$\Delta W = (\gamma\eta^2 + 2\alpha\eta\eta' + \beta\eta'^2)\left(\frac{\Delta p}{p}\right)^2 \equiv H(s)\left(\frac{\Delta p}{p}\right)^2 \quad . \tag{A.18}$$

Equilibrium

The equilibrium of the energy spread and transverse emittances are determined by the balance of the radiation damping and the quantum excitation. They are;

$$\left(\frac{\sigma_p}{p}\right)^2 = C_q \frac{\gamma^2}{J_\varepsilon} \frac{\oint \frac{1}{|\rho^3|} ds}{\oint \frac{1}{\rho^2} ds} \quad \text{and} \quad \epsilon_x = C_q \frac{\gamma^2}{J_x} \frac{\oint \frac{H}{|\rho^3|} ds}{\oint \frac{1}{\rho^2} ds} \quad , \tag{A.19}$$

where J_ε and J_x are the damping partition numbers for longitudinal and horizontal direction, respectively. The bunch length is related to the energy spread by

$$\sigma_\tau = \frac{\alpha}{\Omega E_0} \sigma_\varepsilon \quad . \tag{A.20}$$

Vertical emittance

Since there is no bending in the vertical plane, the vertical emittance is not determined from the design of the beam-optics. In practice, it is governed mainly by:

- vertical dispersion errors, arising from vertical bending fields produced by positioning errors of the magnets.
- coupling of the horizontal and vertical betatron motion, arising from skew-quadrupole field errors. It is produced by angular positioning errors of the quadrupoles and also by vertical closed orbit errors in sextupole magnets.

The coupling is usually expressed by a constant κ which describes the sharing of the natural emittance ϵ_0 between two planes;

$$\epsilon_x = \frac{1}{1+\kappa}\epsilon_0 \quad , \quad \epsilon_y = \frac{\kappa}{1+\kappa}\epsilon_0 \quad . \tag{A.21}$$

A.2 Intra-beam Scattering

Particles in a bunch execute transverse betatron oscillations around the equilibrium orbit (Figure A.6(a)). In the moving frame associated with a bunch, all particle's motion become purely transverse, neglecting the slow synchrotron motion. Particles in a bunch can be scattered each other via Coulomb scattering, resulting in the momentum transfer from transverse to longitudinal (Figure A.6(b)). Such a change in the direction of the momentum can lead to a large energy change due to the relativistic effect. It causes particle losses and an increase of transverse emittance [50].

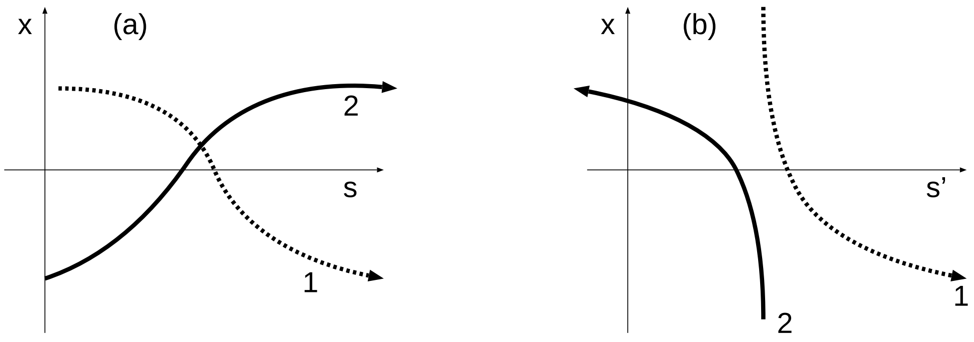

Figure A.6: Coulomb scattering of two particles inside a bunch. (a) Laboratory system, (b) Center of mass system.

A.2.1 Touschek effect

When a particle in a beam undergoes an intra-beam scattering and its longitudinal momentum exceeds the energy acceptance of the ring, then the particle is lost and the beam life time is shortened. This effect is called Touschek effect. This effect becomes strong at high particle density (high intensity and small bunch volume) because the particles have more chances to scatter. The total rate of collisions leading to losses can be written as

$$\frac{dN}{dt} = \int_V \frac{\sigma_T(\nu)}{\gamma^2} \nu n^2 dV \quad , \tag{A.22}$$

where N is the total number of particle in a bunch, V the bunch volume, ν the relative velocity of particles, σ_T the cross section of the scattering which leads the beam loss, and n is the particle density. The factor γ^2 takes account of the Lorentz transformation to the laboratory frame.

Although the loss rate depends on the particle distribution in the phase space and the beam-optics of entire ring, roughly speaking it is proportional to the density of the particle

$$\frac{1}{N}\frac{dN}{dt} = \frac{1}{\tau} \sim \frac{N}{\sigma_x \sigma_y \sigma_z} \quad . \tag{A.23}$$

The intensity depending beam lifetime has been clearly observed at ATF, and the vertical emittance could be estimated from the lifetime ([49]).

A.2.2 Intra-beam scattering

Even if the momentum transfer of the scattering in a bunch is not large enough to exceed the acceptance, it can excite the longitudinal and transverse motion. Multiple experience of the small angle scattering disturbs the particle motion as a noise source. Similar to the quantum excitation, it increases the energy spread and the transverse emittance through the finite dispersion function.

A.3 Fast Beam-Ion Instability

A transient ion instability of a multi-bunch electron beam have been studied experimentally at ALS [43] and PLS [44][45] and also theoretically [52],[53]. Charged particles ionize residual gasses and generate free ions along the orbit. Since the ions and the beam have opposite charges, the ions are strongly attracted and oscillate in transverse direction. It causes a transverse kick of the following beam (Figure A.7). It differs from the conventional ion trapping, which is caused by the ions slowly trapped in multiple beam passages.

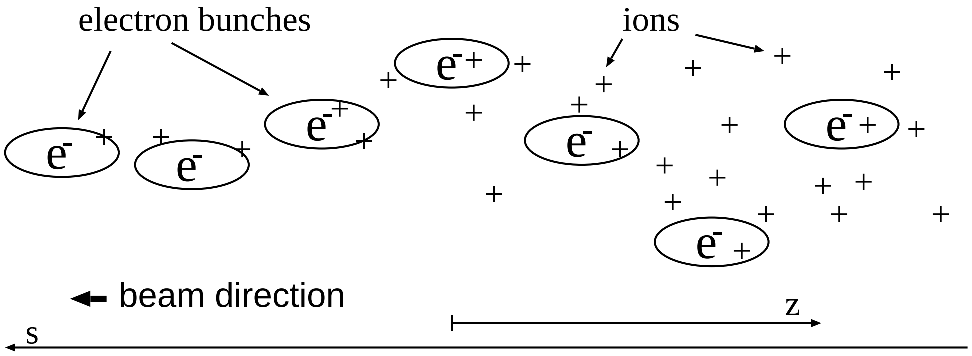

Figure A.7: Schematic diagram for the explanation of fast beam ion instability. The tail part of the beam train is kicked by the ions generated by the passage of head part of the train.

A.3.1 Equations of motion

The vertical motion of the beam and the ions is a mutually-driven oscillation. In a linear approximation, it is described by two equations of motions.

The first equation describes the motion of the beam position (y_b),

$$\left(\frac{d^2}{ds^2}+\omega_\beta^2\right) y_b(s,z) = K\Gamma(z)\left(y_i(s,s+z)-y_b(s,z)\right) \tag{A.24}$$

$$K \approx \frac{4\lambda_{\text{ion}}(p_{\text{gas}})r_e}{\gamma 3\sigma_y(\sigma_x+\sigma_y)} \tag{A.25}$$

$$\Gamma(z) = \int_{-\infty}^{z}\rho(z')dz' \quad . \tag{A.26}$$

The coordinate is shown in Figure A.7; s denotes the longitudinal position along the beam line, z the position along the multi-bunch train. σ_x and σ_y the beam size. λ_{ion} is the generation rate of the ion at given gas pressure. ρ is the charge density along the train. r_e is the classical radius of electron. The motion is a combination of a betatron oscillation, represented by a harmonic oscillator of frequency ω_β and a driving force that is proportional to the distance between the beam and the ion centroids and to the number of generated ions.

The second equation is for the vertical centroid ($\tilde{y}_i$) of transverse slice of the ions at fixed position s,

$$\left(\frac{d^2}{dt^2}+\omega_i^2\right)\tilde{y}_i(s,t) = \omega_i^2 y_b(s,z) \tag{A.27}$$

$$\omega_i \equiv \sqrt{\frac{4c^2N_b r_p}{3L_{\mathrm{sep}}\sigma_y(\sigma_x+\sigma_y)A}} \tag{A.28}$$

$$y_i(s,t) = \frac{\int_{-\infty}^{z} dz'\rho(z')\tilde{y}_i(s,t|s+z')}{\int_{-\infty}^{z} dz'\rho(z')} \quad . \tag{A.29}$$

The oscillation frequency of the ion (ω_i) is proportional to the square root of beam density, which is determined by the number of particles per bunch (N_b), the bunch spacing (L_{sep}), and the beam sizes (σ_x, σ_y), and inverse proportional to the square root of the ion mass (A designates the atomic number). r_p is the classical proton radius. The centroid of the ions is obtained by averaging $\tilde{y}_i(s,s+z')$ over all possible creation times (Eq.A.29).

The initial position of the ions must be the same as the beam that created them ($\tilde{y}_i(s,t'|t') = y_b(s,ct'-s)$), and the movement at the generation time is assumed to be zero ($d\tilde{y}_i(s,t'|t')/dt = 0$).

A.3.2 Solution

The equations of motions were analytically solved under some approximations. The development of the beam position along the beam line (s) and along the train (z) is,

$$y_b(s,z) \approx \hat{y}\frac{1}{4\sqrt{\pi}}\frac{1}{\eta^{1/4}}\exp(2\sqrt{\eta})\sin(\omega_i z-\omega_\beta s+\theta) \tag{A.30}$$

$$\eta(s,z) \equiv \frac{K\omega_i(z+z_0)^2 s}{\omega_\beta 16 z_0} \quad . \tag{A.31}$$

The basic properties of the amplitude growth of the oscillation are;

- The beam position is modulated along the train by the frequency of the ion oscillation ($\sim \sin(\omega_i z-\omega_\beta s)$).
- The amplitude of the oscillation grows exponentially along the train, and quasi-exponentially along the beam line ($\sim \exp(z\sqrt{s}$).
- The growth rate depends on various factors, for example, the gas pressure and species, beam charge, beam sizes etc..

Appendix B

Laserwire Monitor Utilizing a Higher Order Mode

As explained in Chapter 4, ATF succeeded in reducing the vertical emittance to the half of its original target value. Such a small beam size close to the resolution limit of the present laserwire monitor. For example, we measured an electron beam of 4 μm with a laserwire of 5.6 μm, and obtained a count rate profile of 6.9 μm as a convolution. The laserwire was thicker than the beam size. Apparently, it is not possible to measure much smaller beam size by the present setup.

In order to improve the resolution of the laserwire, it has been proposed to use a higher order mode of the Gaussian beam. In this chapter, we describe the method and the results of the first experiment done with this new technique.

B.1 An idea of utilizing the higher order mode

B.1.1 Diffraction limit

A laser beam has a parabolic shape along its longitudinal axis. The length of the central part is characterized by the Rayleigh length (z_0), and z_0 is determined by w_0 and λ (Eq.3.39). If we design a beam waist to be smaller, the Rayleigh length also becomes smaller.

In the case of ATF, the electron beam has a flat shape with an aspect ratio of about 10:1. We must be careful in choosing the Rayleigh length not too small compared to the horizontal size of the electron beam. In fact, if the beam waist (w_0) is reduced to less than 10 μm, the laser beam can not be treated as a simple solid wire which has a constant width. This situation is illustrated in Figure B.1.

To avoid this effect, the only way is to change the laser wave length. However, there are some technical problems in using shorter wave length. Fabrication of a low-loss and high-reflectance mirror suit for a high finesse cavity is quite difficult in the short wave length region. A high power and stable laser which meets our specification is also not available now. We conclude that the diffraction effect and some technical difficulties limit the resolution of the current laserwire monitor.

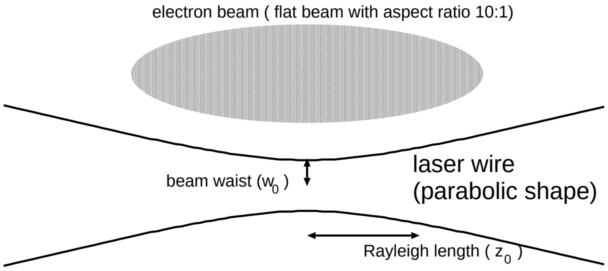

Figure B.1: Schematic diagram for the explanation of the diffraction effect. The shape of a laser beam is characterized by w_0 and z_0. The Rayleigh length (z_0) should be large enough compared to the horizontal size of an electron beam.

In order to improve the sensitivity for beam size less than the laser waist size, an idea has been proposed. This technique utilizes a TEM$_{01}$ mode, instead of TEM$_{00}$, in the optical cavity.

B.1.2 Higher order modes of an optical cavity

First of all, some basic properties of higher order modes should be summarized here. The transverse profiles of several modes are shown in Figure B.2. These modes are denoted as TEM$_{mn}$ and classified according to the order of the mode ($m + n$). Modes belonging to the same order experience the same Guoy phase factor (Φ in Eq.3.35), and have the same resonance condition. The projected intensity distribution along the y direction for TEM$_{00}$ and TEM$_{01}$ mode are shown in Figure B.3. The TEM$_{01}$ mode has two lobes and one node.

B.1.3 Principle of the beam size measurement with a TEM$_{01}$ laserwire

We consider below that the beam size measurement with TEM$_{01}$ laserwire. Let us suppose the electron beam intensity distribution is a Gaussian expressed by

$$P_e(y) \sim \exp\left(-\frac{y^2}{2\sigma_e^2}\right) \tag{B.1}$$

and the TEM$_{01}$ laserwire is given by

$$P_{lw}(y) \sim (y-\eta)^2 \cdot \exp\left(-\frac{(y-\eta)^2}{2\sigma_{lw}^2}\right) \tag{B.2}$$

where η represents the relative position of the laserwire to the beam. When we scan the beam, we would obtain a convoluted profile expressed by

$$L \sim \int \exp\left(-\frac{y^2}{2\sigma_e^2}\right) \cdot (y-\eta)^2 \exp\left(-\frac{(y-\eta)^2}{2\sigma_{lw}^2}\right) dy \tag{B.3}$$

$$\sim \left(\frac{\sigma_{lw}^2}{\sigma_e^2+\sigma_{lw}^2} \cdot \eta^2 + \sigma_e^2\right) \exp\left(-\frac{\eta^2}{2(\sigma_e^2+\sigma_{lw}^2)}\right) \tag{B.4}$$

Examples of such profiles are shown in Figure B.4 for three different electron beam sizes (σ_e = (0.2, 0.5, 0.8) $\times\sigma_{lw}$). The depth of the valley at the center indicates a good

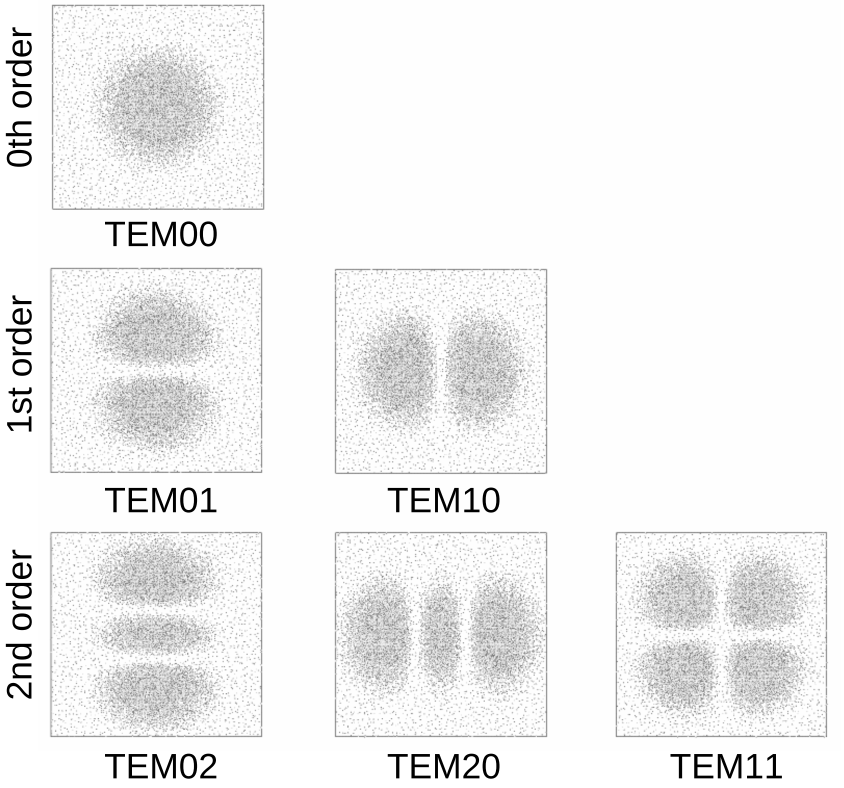

Figure B.2: Transverse profile of several modes. TEM_{00} is the fundamental mode, which has a simple Gaussian intensity distribution. The higher order modes have dip structures in its profiles. These TEM_{mn} modes are classified according to the order $(m+n)$.

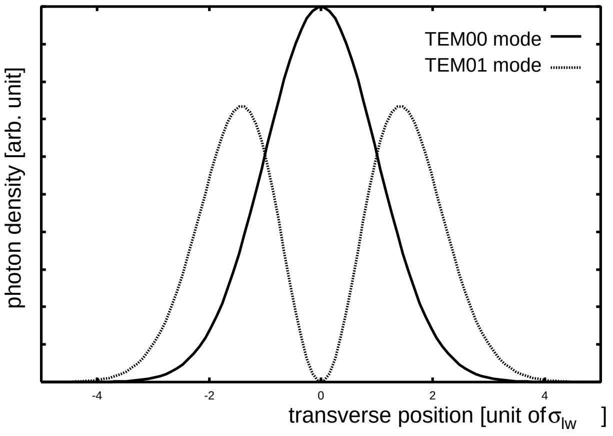

Figure B.3: Projected intensity distribution along the y direction of TEM_{00} and TEM_{01}. The TEM_{01} mode has the zero intensity at the center, and two peaks on both sides.

sensitivity to the size of an electron beam. The ratio of the minimum intensity at the center to the intensity at two side peaks can be a good measure for an electron beam size. The maximum-to-minimum ratio is shown in Figure B.5 as a function of the electron beam size. An electron beam smaller than a laser beam is measurable by this method. If we design the beam waist (w_0) of an optical cavity to be 20μm (σ_{lw} =10μm), it has a good sensitivity for an electron beam of 3μm $\sim$ 10μm range.

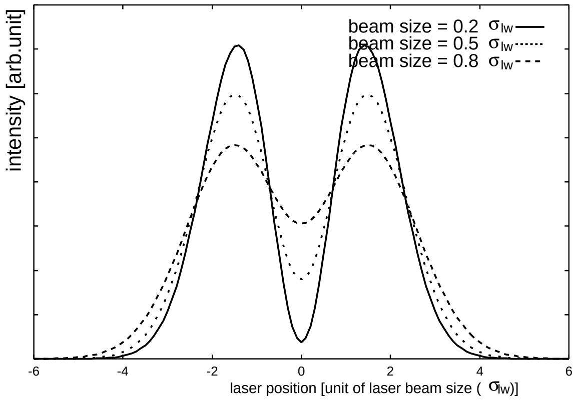

Figure B.4: Expected signal profiles scanned by the TEM_{01} mode laserwire. The results for three different sizes of the electron beam are shown.

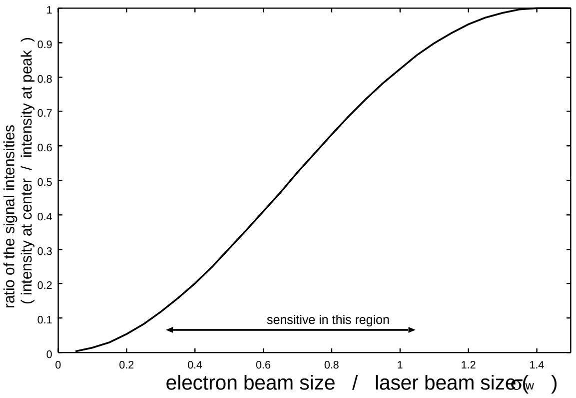

Figure B.5: Sensitivity of the TEM_{01} mode measurement. This plot shows the dependence of the maximum-to-minimum value (intensity at the center)/(intensity at the peaks) as a function of an electron beam size. It is sensitive to a beam size smaller than the laser beam waist.

B.2 Realization of the TEM_{01} mode resonance

B.2.1 Mode splitting of TEM_{01} and TEM_{10} mode

Since the resonance condition depends on the order of the mode, TEM_{01} can be separately excited from TEM_{00}, TEM_{02}, TEM_{11}, TEM_{20} and higher ones. TEM_{10}, however, belongs to the same order, and has the same resonance condition. If both TEM_{01} and TEM_{10} modes are excited at the same time, these two modes interfere each other and result in a tilted profile. We thus need some means to realize and select a pure TEM_{01} mode:

In order to lift the degeneracy between two 1st order modes, we introduced small distortion to the mirror shape. The cavity mirrors originally have spherical surfaces, and there is nothing to distinguish one direction from the other. The mirror holder was modified as shown in Figure B.6. An end plate, having a step of 15μm high along its diameter, was inserted underneath of the mirrors. The mirrors were pushed against the end plate, resulting in a small bending.

We checked the amount of distortion with a surface-shape monitor system based on the optical interferometry ([55]). This monitor provides a sample with a spherical light

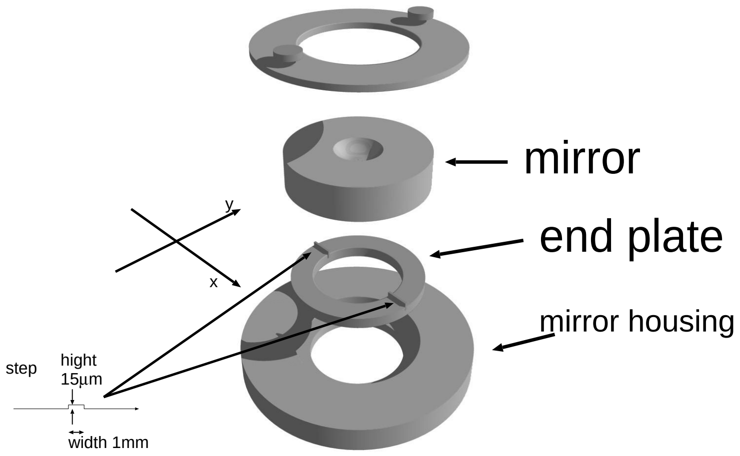

Figure B.6: Structure of the mirror holder. An end plate is inserted underneath of a mirror. The step along the diameter on the end plate distorts the surface of the mirror.

wave, and detects interference between a reflected light and a reference wave. It actually measures the amount of the surface distortion from a spherical shape. Figure B.7 shows a result with a dummy mirror (the same shape and same substrate but no coating) mounted in the modified mirror holder. An interference pattern suggesting a saddle-shaped distortion is clearly seen; the effective radius of curvature along y axis becomes bigger, and the one along x axis becomes smaller. The change of the curvature radius along two axises were extracted from the interference pattern. The distance between two dark fringes corresponds to the half wave length of the light (316 nm).

B.2.2 Excitation of higher order modes

Since the input laser is mostly composed of the TEM_{00} mode, it is necessary to convert it to TEM_{01}, which is the cavity mode we want to excite. We tried two ways to do it. The simplest way is to slightly displace the axis of the injected laser beam. At first step, the laser injection was carefully tuned to completely match the TEM_{00} mode of the cavity. The positions of the lenses and the axis of the injection beam were tuned while monitoring the excitation of the higher order modes (Figure B.8 (a)). Then, the injection axis was laterally shifted along y axis by shifting the transverse position of a steering mirror. We observed a decrease in the TEM_{00} component and an increase in TEM_{01} (Figure B.8 (b)). The peak height of the TEM_{01} mode reached about 40% of the initial TEM_{00} peak after adjusting the injection axis. This value agrees well with the theoretical expectation ([56]).

The other method is to convert the electric field of an injected laser beam into anti-symmetric. The principle of this method is explained in Figure B.9(left). A plastic film of about 100μm thickness is inserted halfway into the laser beam. The index of the film changes the relative phase of the laser light. The effective thickness of the film can be varied by the insertion angle. If the phase shift is tuned to be π, the laser beam contains only anti-symmetric transverse modes. Thus TEM_{00} component is converted into a sum of TEM_{01}, TEM_{03} and higher modes of odd orders. About 60% of the initial TEM_{00}

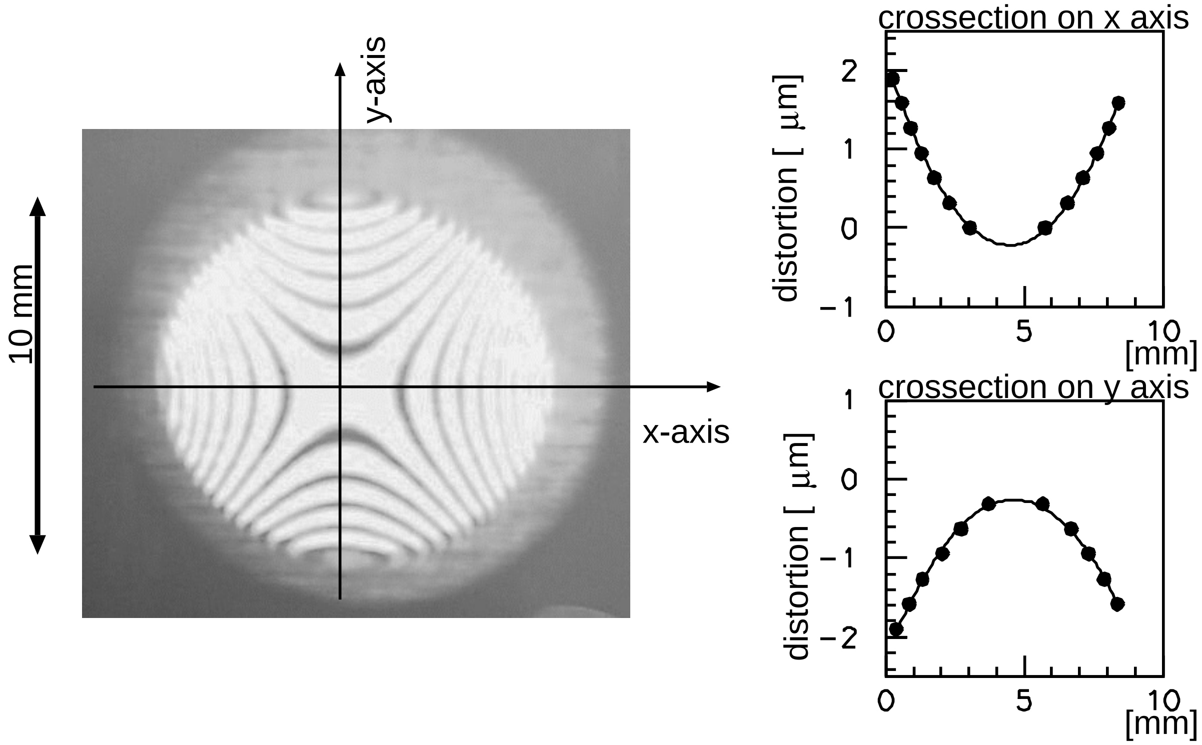

Figure B.7: Mirror distortion measurement. The distortion is measured by the interferometer (zygo). The distance between two dark fringes corresponds to 316 nm. A saddle-shaped distortion is observed.

mode can be converted into TEM$_{01}$ component. We call this film a mode converter. Figure B.9(right) shows the excitation of the TEM$_{01}$ mode with this method.

The cavity was feedback controlled to keep the resonance condition of the TEM$_{01}$ peak during beam size measurement. We finally note that the same cavity acts as the TEM$_{00}$ laserwire, if the mode converter is not inserted.

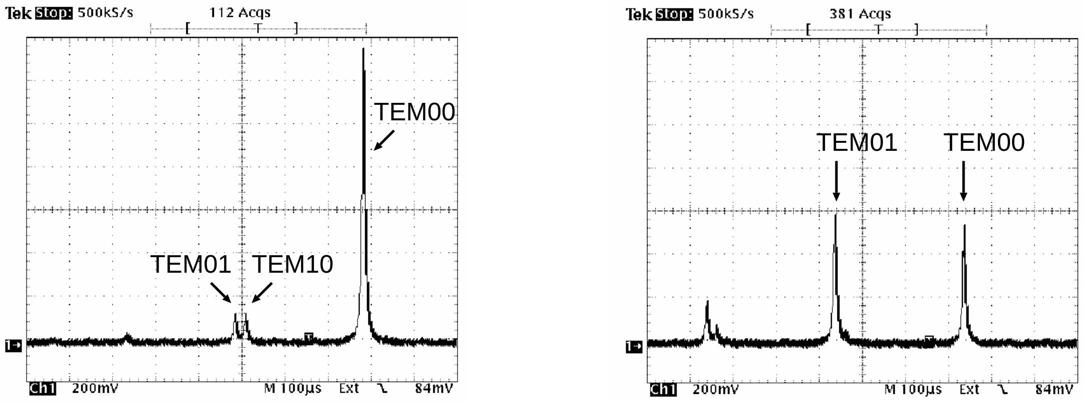

(a) matched injection

(b) mismatched injection
(lateral offset)

Figure B.8: Higher mode excitation by injection axis shift. (a):The mode excitation after injection was matched to the fundamental mode of the cavity. (b):The excitation of the higher order modes when injection axis was laterally displaced from (a). The vertical scales of these pictures are the same; it can be seen that the peak hight of TEM$_{01}$ component in (b) is about 40% of the TEM$_{00}$ component in (a).

B.3 Measurement of an electron beam size

We replaced the horizontal laserwire in the beam line with the new cavity. The purpose, at this stage, was to prove the principle of this method. The beam waist (w_0) of the new cavity was designed to be about 20μm (see Figure B.5); optimized for the expected beam size of 4∼10 μm. The new cavity has been in operation since October 2003. We present the measurement results obtained on February 20, 2004 as an example.

B.3.1 Data taking

In this series of measurements, 6 sets of data (runs) were taken as listed in Table B.1. As shown, run a and b use the different laserwire mode with the same beam condition. The aim of these runs were to compare two results and to test the performance of the new method. The other 4 runs, c∼f, were done with the TEM$_{01}$ laserwire changing the vertical beam sizes. As mentioned, switching of the laserwire modes, TEM$_{00}$ to TEM$_{01}$, was carried out by inserting the mode converter.

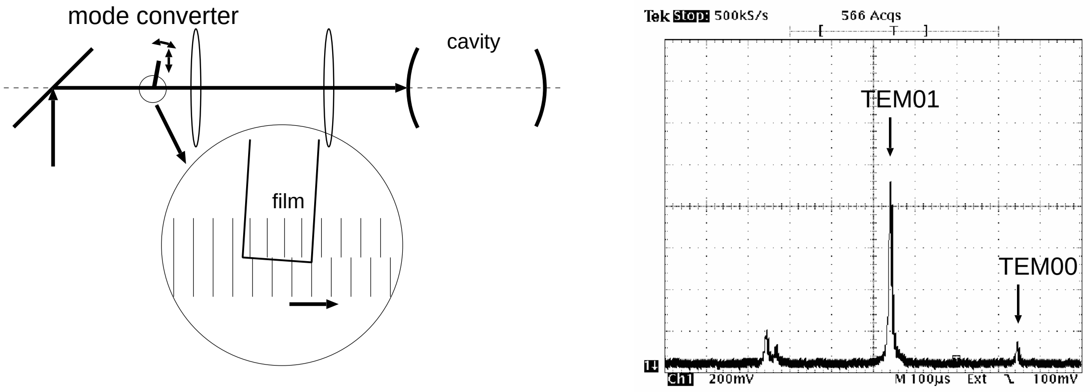

Figure B.9: Higher mode excitation by mode converter. (left):The principle of the mode converter. A plastic film flips the phase of the upper-half part of the laser beam. (right):The excitation of the higher order modes by this method. The scale of this picture is the same as the ones in Figure B.8. The peak hight of TEM_{01} component is about 60% of the TEM_{00} component of the initial case.

Table B.1: List of the beam and laser conditions.

run	laser mode	conditions of the electron beam
a	TEM_{00}	normal
b	TEM_{01}	normal
c	TEM_{01}	1/4 of skew correctors turned off
d	TEM_{01}	1/2 of skew correctors turned off
e	TEM_{01}	All skew correctors turned off
f	TEM_{01}	skew correctors half off, half reversed

Table B.2: Results of the measurements by the TEM$_{01}$ mode laserwire.

run	σ_{meas} (μm)	σ_{lw} (μm)	σ_e (μm)	χ^2/ndf
a	11.19±0.12(±0.16)	N/A	5.21±0.30(±0.38)	39.5/22
b	N/A	10.53±0.21(±0.21)	4.27±0.48(±0.50)	23.3/22

B.3.2 Analysis and Result

After the background rate was statistically subtracted, the current normalized count rate (Hz/mA) was plotted as a function of the laserwire position. They are shown in Figure B.10.

In the cases of the TEM$_{00}$ mode measurement, the data were fitted by a Gaussian function to obtain σ_{meas}. As for the TEM$_{01}$ mode measurement, we employed a fitting function

$$A\left(\frac{\sigma_{lw}^2}{\sigma_e^2+\sigma_{lw}^2}\cdot(y-y_0)^2+\sigma_e^2\right)\exp\left(-\frac{(y-y_0)^2}{2(\sigma_e^2+\sigma_{lw}^2)}\right) \quad , \tag{B.5}$$

where y is the vertical position of the laserwire. Four parameters were left free: square of the electron beam size (σ_e^2), square of the laser width (σ_{lw}^2), offset of the center position (y_0) and an overall scale factor (A).

The results of first two measurements (run a and b) are listed in Table B.2. In the Table B.2, the reduced chi-squares (χ^2/ndf) are also listed. If χ^2/ndf is greater than 1, then all statistical errors were uniformly enlarged so that χ^2/ndf became unit (χ^2/ndf=1). The final errors obtained in this way were presented in the parentheses. Since the measurement with the TEM$_{00}$ mode gave only the convoluted size (σ_{meas}), σ_{lw} had to be subtracted in extracting the bean size (σ_e). To this end, we made use of the 14 measurement results obtained since the installation of the new cavity. The 14 values for σ_{lw} and σ_e are plotted in Figure B.11. As seen, the values for σ_e differ significantly due to different beam tuning. In contrast, the values for σ_{lw} agree well each other. The final value is σ_{lw}=9.90±0.070(±0.087)μm which is an average of these 14 data sets. The measurement with the TEM$_{01}$ mode gave both σ_e and σ_{lw} at the same time. The results for σ_e of two measurements were confirmed to be consistent within the errors.

B.4 Summary

We have reported the resolution limit of the existing laserwire monitor. A new method to measure an electron beam size smaller than the laser waist size, is described. A stable excitation of TEM$_{01}$ in an optical cavity was realized with a modified mirror-holder and a new laser injection scheme.

We measured an electron beam with the TEM$_{01}$ mode laserwire, and compared the result with the measurement with the TEM$_{00}$ mode. The two consecutive scans of the

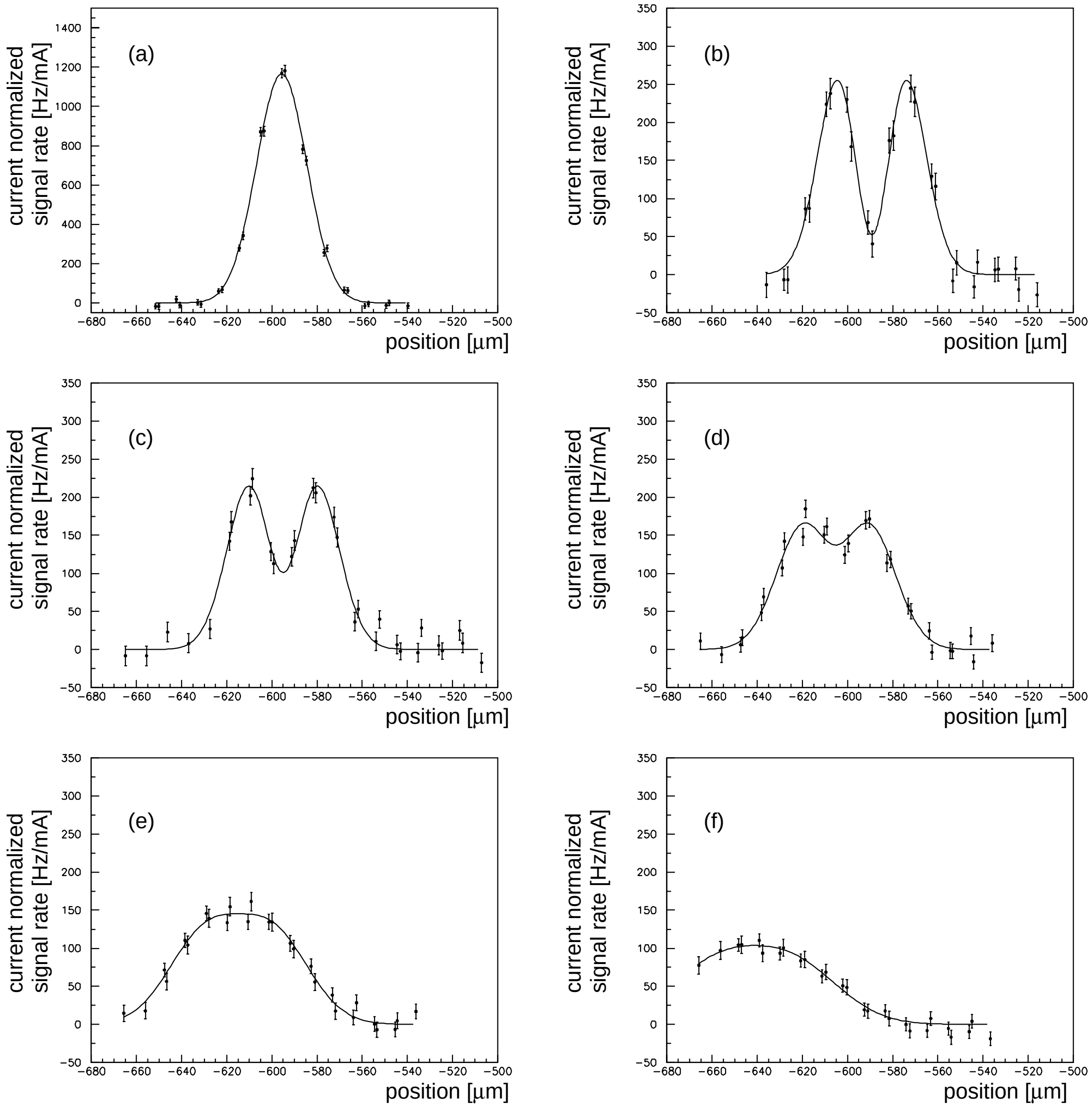

Figure B.10: Measured profiles by the TEM$_{01}$ mode laserwire. (a)∼(f) correspond to the measurements listed in Table B.1. The solid lines are the fit results.

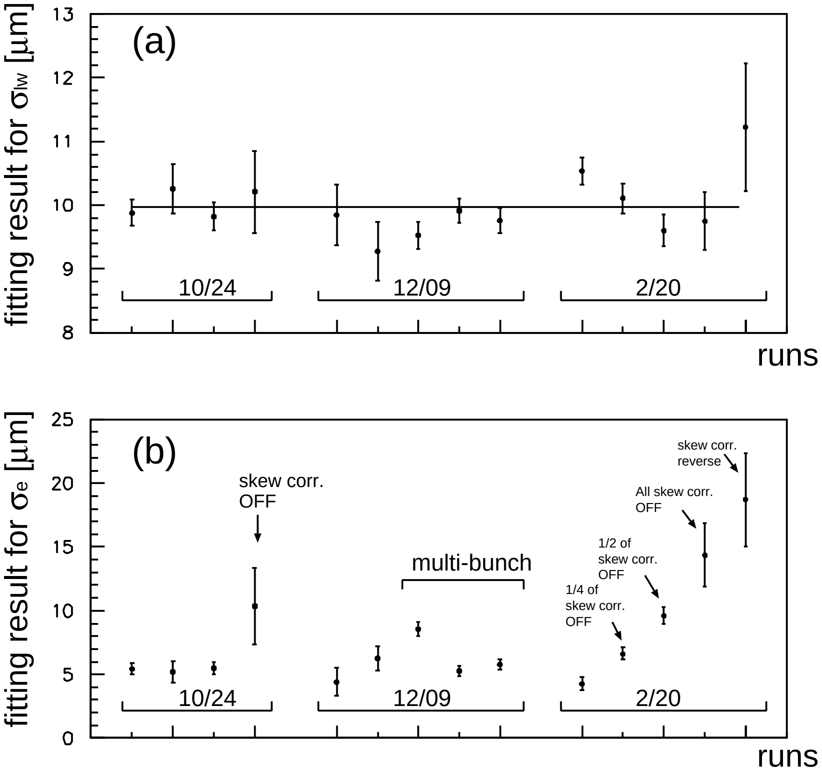

Figure B.11: Results of σ_{lw} and σ_e by the TEM$_{01}$ mode laserwire. All the measurements gave consistent results for σ_{lw}.

same electron beam by switching the mode of the laserwire gave a consistent result, which confirmed the principle of the measurement with this new technique. This technique improves the resolution of the beam size measurement by factor 2∼3, and can be used in the ultra-low emittance studies at the ATF damping ring.

Appendix C

Latest Results of the Multi-Bunch Measurement

The bunch intensity designed for a linear collider is 0.75×10^{10} e/bunch, which corresponds to the total current of 50 mA for 20-bunches beam in ATF damping ring. The experiments described in Sec. 5.3 and Sec. 5.4 were performed with a relatively low beam intensity. The highest beam current measured was 20mA, only 40% of the requirement.

Since 2004, ATF started to operate a high current multi-bunch beam. In this appendix, we report the progress in the spring runs of 2004.

C.1 Change in the laserwire setup

As explained in Appendix B, we replaced the horizontal-laserwire to a new cavity in 2003 summer. The parameters of new cavity was designed to maximize the sensitivity of TEM_{01} mode scan for typical ATF beam. To this end, the laser width (σ_{lw}) becomes twice much than it used to be. As already concluded in Appendix B, the laser width of the new cavity was σ_{lw}=9.90±0.070(±0.087) μm.

Although the TEM_{01} mode has an advantage in the measurement of small beam, its sensitive region is limited for large beam. Since there may be a strong beam blow-up in the case of high-current multi-bunch beam, we utilized the normal TEM_{00} mode in this study.

C.2 Data taking

The experiment was done on May 18, 2004. Prior to the multi-bunch measurement, we did the usual damping ring tuning procedures in single bunch mode. Then, we switched to multi-bunch mode and tuned the beam injection. Due to the strong beam loading effect of high intensity multi-bunch beam, a precise tuning of energy compensation system of linac was necessary to efficiently inject all bunches. After a careful tuning of the electron gun and the linac, we succeeded in storing 50mA with 20-bunch beam.

When high current beam was stored in the ring, the vacuum pressure was increased due to the huge amount of synchrotron radiation hit on the beam chamber. The growth

Table C.1: List of beam conditions.

run	train number	total current (mA)	average pressure ($\times 10^{-6}$pa)
A	1	31.1 ± 8.0	6.5
B	1	25.8 ± 2.6	6.0
C	1	11.3 ± 1.7	4.0
D	3	27.3 ± 2.9	6.0
E	3	76.3 ± 8.5	10.0

rate of multi-bunch beam instability can depend both on the bunch intensity and the vacuum pressure.

In order to change the vacuum pressure with the same bunch intensity, we took data in two types of multi-bunch mode. One was the usual multi-bunch mode, single train of 20-bunch beam was stored in the ring. The other was the three-train multi-bunch mode. In this operational mode, three sets of 20-bunch beam was stored in the ring at the same time. Since the vacuum pressure was basically determined by the total current, in enhanced the pressure effect for the same bunch intensity.

The vertical beam size was measured by the laserwire monitor. The beam conditions of these measurement are summarized in Table C.1. We measured three different current for single-train multi-bunch beam, and two for three-train. In the measurement of three-train mode, the laserwire measured the one train of the three which is injected in the same timing as the single-train mode.

C.3 Results and discussion

The vertical emittance [1] was calculated using the beta function measured in single-bunch mode after the runs.

The bunch-dependence results of vertical emittance in three different current of single-train mode are plotted in Figure C.1. Although the first part of the bunches have a small vertical emittance, a strong blow-up along the train was observed in high current. This result can be well explained by the simulation results based on the fast-beam-ion instability assuming some reasonable parameters [57]. The results of three-train mode are plotted in Figure C.2. It was found to become much worse than the single-train case.

Comparison between the results of run B and D, the ones in the same total current and pressure but about factor-three different bunch intensity, there is a clear difference. The growth rate depends on the bunch intensity.

On the other hand, if we compare the runs with same bunch intensity but with different number of train, run B and E (or run C and D), there also are clear differences seen. It suggests the dependence on the vacuum pressure.

---

[1] In this measurement, the emittance is defined to be the average particle distribution of many revolution with respect to the central orbit. The coherent transverse motion is included.

Considering over all nature of these observation, the cause of the blow-up is likely the first-beam-ion instability. Different from the experiment described in Sec. 5.5, all the condition of the pumps were left normal in this measurement. However, due to the pressure increase caused by the high current and/or increased ion generation rate by high bunch intensity, the vertical emittance blow-up occurred. The only way to suppress this effect is to improve the pressure. Improvement of the pump system or chamber aging with a high current beam will be needed to realize a small emittance multi-bunch beam with design beam intensity.

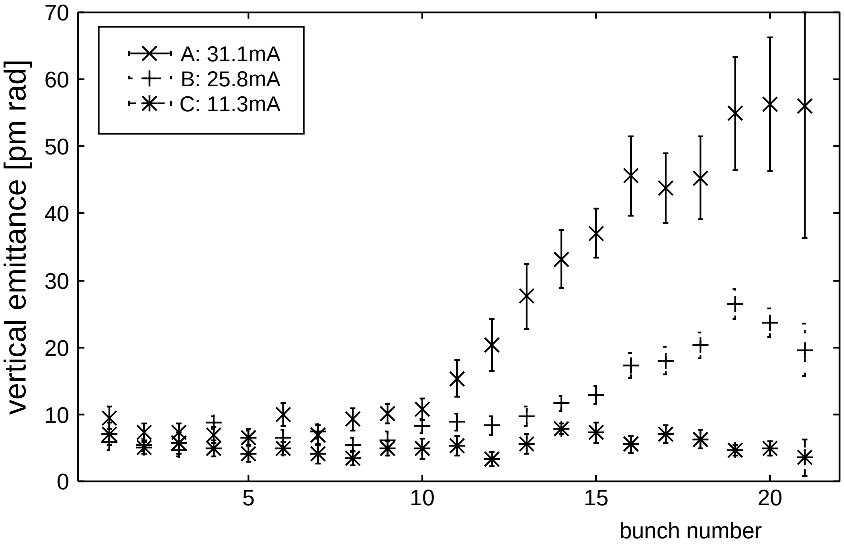

Figure C.1: Results of the single-train multi-bunch beam.

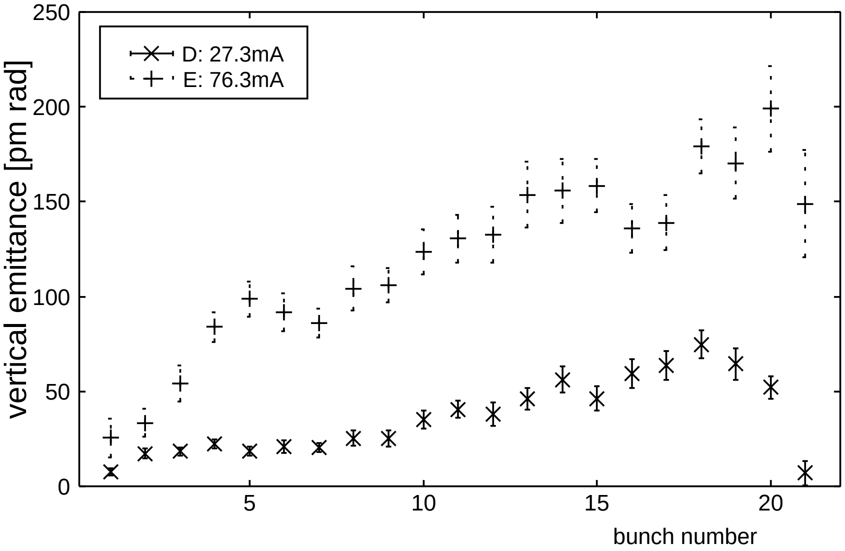

Figure C.2: Results of the three-train multi-bunch beam.

Bibliography

[1] R. Brinkmann,*et al.* (eds.),
"TESLA Technical Design Report";
DESY-2001-011, March 2001.

[2] T.O. Raubenheimer, ed. [NLC ZDR Design Group],
"Zeroth order design report for the Next Linear Collider";
SLAC-R-0474 (1996).

[3] "GLC Project"; KEK Report 2003-7.

[4] G. Guignard, ed. [The CLIC Study Team],
"A 3 TeV e+/e- Linear Collider Based on CLIC Technology";
Report CERN 2000-008 (July 2000).

[5] P. Raimondi and A. Seiri,
"Novel Final Focus Design for Future Linear Colliders";
Phys. Rev. Lett. **86** (2001) 3779.

[6] International Linear Collider Technical Review Committiee,
"ILC-TRC Second Report".

[7] R.Alley *et al.*,
"A laser-based beam profile monitor for the SLC/SLD interaction region";
Nucl. Instrum. Meth. A **379**(1996) 363.

[8] G.Blair,*et al.*,
in Proceedings of the European Particle Accelerator Conference,
Paris, 2002, pp.1912-1914.

[9] T.Shintake,
"Proposal of Nanometer beam size monitor for e^+e^- linear colliders";
Nucl. Instrum. Meth. A **311**(1992) 453.

[10] Edited by F. Hinode, S.Kawabata, H.Matsumoto, K.Oide, K.Takata, S.Takeda and Urakawa,
"ATF design and study report"; KEK Internal 95-4 (1995).

[11] U.Keller,
"Recent development in compact ultrafast lasers";
nature vol.424 (2003) 831.

[12] H.Hayano, private communication.

[13] C5680, Hamamatsu Photonics.

[14] H. Hayano,
"Wire scanners for small emittance beam measurement in ATF";
The Proceedings of 20th Linear accelerator conference (2000),
http://linac2000.slac.stanford.edu/

[15] T. Naito,*et al.*,
in Proceedings of the Particle Accelerator Conference,
New York, 1999, pp.2143-2145.

[16] K.Iida *et al.*,
"Measurement of an electron-beam size with a beam profile monitor using fresnel zone plates";
Nucl. Instr. Method A 506(2003) p41-49.

[17] T.Muto *et al.*.
"Observation of Incoherent Diffraction Radiation from a Single-Edge Target in the Visible-Light Region";
Phys. Rev. Lett. **90** (2003) 104801.

[18] Leica SMART 310, Noecross , Georgia 30071.

[19] M. Ross, J. Nelson, M. Woodley, A. Wolski,
SLAC-PUB-9239,Jun 2002. 4pp.

[20] K. Kubo ,
" Simulation stuey of low emittance tuning of the Accelerator Test Facility damping ring at KEK";
Phys. Rev. Special Topics - Accelerator and Beams, **6**, 092801 (2003).

[21] SAD is a computer program for accelerator design.
http://acc-physics.kek.jp/SAD/sad.html

[22] H.Sakai *et al.*,
"Performance studies of a laser wire beam profile monitor";
Jpn. J. Appl. Phys **41** (2002) 6398.

[23] H.Sakai, Doctor thesis submitted to Kyoto University (2002).

[24] Y.Honda *et al.*,
"Upgraded Laser Wire Beam Profile Monitor";
Nucl. Instr. Meth., accepted for publication.

[25] M.E.Peskin and D.V.Schroeder,
"An Introduction to Quantum Field Theofy"; Addison-Wesley (Massachusetts, 1995).

[26] A.Yariv ,
"Optical Electronics";
holts, Rinehart and Winston, (New York, 1991), 4th ed.

[27] N.Hodgson and H.Weber,
"Optical Resonators"; Springer (1997).

[28] Series 142 Diode-pumped single-frequency CW green laser, LightWave.

[29] Research Electro-Optics, Inc. (REO); Boulder, Colorado.

[30] Y.Honda,
Master thesis of Kyoto University, (2001: in japanese, unpublished).

[31] users manual of LC2440 and LB040 Series; Keyence.

[32] C7884 Linear Image Sensor; Hamamatsu Photonics.

[33] Y.Honda, K.Kubo *et al.*,
"Achievement of ultra-low emittance beam in the ATF damping ring";
Phys. Rev. Lett. **92**, 054802 (2004)

[34] "ATF Accelerator Test Facility Study Report JFY 1996-1999";
KEK internal Report No. 2000-6, edited by H. Hayano *et al.*, 2000, (unpublished).

[35] T. Okugi *et al.*
"Evaluation of extremely small horizontal emittance";
Phys. Rev. Special Topics- Accelerator and Beams **2**, 022801 (1999)

[36] J. Urakawa,
in Proceedings of the Seventh European Particle Accelerator Conference,
Vienna, 2000, pp.63-67.

[37] K.Kubo *et al.*,
"Extremely Low Vertical Emittance Beam in Accelerator Test Facility at KEK";
Phys. Rev. Lett. **88**, 19 (2002)

[38] K.L.F. Bane *et al.*,
" Intrabeam Scattering Analysis of measurement at KEK's ATF damping ring";
Phys. Rev. Special Topics - Accelerator and Beams, **5**, 084403 (2002)

[39] H.Sakai *et al.*,
"Measurement of a small vertical emittance with a laser wire beam profile monitor";
Phys. Rev. Special Topics - Accelerator and Beams, **5**, 122801 (2002)

[40] N.Terunuma *et al.*
"Impedance Measurement of ATF DR";
in Proceedings of the Sixth European Particle Accelerator Conference, Stockholm, 1998, 481.

[41] Y.Honda *et al.*,
”Measurement of electron beam emittance in the ATF damping ring operated in multi-bunch modes“;
Phys. Rev. Special Topics - Accelerator and Beams, **6**, 092802 (2003)

[42] T. Naito, private communication.

[43] J.Byrd *et al.*,
“First Observations of a “Fast Beam Ion Instability” ”;
Phys. Rev. Lett. **79**, 79 (1997).

[44] M.Kwon *et al.*,
“Experimental results on the fast beam-ion instability”;
Phys. Rev. E. **57**, 6016 (1998).

[45] J.Y.Huang *et al.*,
“Direct Observation of the Fast Beam-Ion Instability”;
Phys. Rev. Lett. **81**, 4388 (1998).

[46] “CAS Fifth General Accelerator Physics Course”; CERN 94-01 (1994).
“CAS Fifth Advanced Accelerator Physics Course”; CERN 95-06 (1995).

[47] H.Wiedemann,
“Particle Accelerator Physics”; Springer Verlag, New York, 2nd ed.

[48] M.Sands,
“The Physics of Electron Storage Rings”; SLAC-121 (1970).

[49] T.Okugi,
“Evaluation of vertical emittance in KEK-ATF by utilizing lifetime measurement”;
Nucl. Instr. Meth. A **455** (2000) 207-212,

[50] A.Piwinski,
in *Handbook of Accelerator Physics*; World Scientific (1999) p125.

[51] J.Bjorken and S.Mtingwa;
Part. Accel **13**, (1983) 115.

[52] T.O.Raubenheimer and F.Zimmermann,
“Fast beam-ion instability. I. Linear theory and simulations”;
Phys. Rev. E **52**, 5487-5498 (1995).

[53] G.V.Stupakov, T.O.Raubenheimer and F.Zimmermann,
“Fast beam-ion instability. II. Effect of ion decoherence”;
Phys. Rev. E **52**, 5499-5504 (1995).

[54] Y.Honda *et al.*, in preparation.

[55] ZYGO; Laurel Brook Road Middlefield, CT

[56] F. Bayer-Helms,
"Coupling coefficients of an incident wave and the modes of the spherical optical resonator in the case of mismatching and misalignment";
Applied. Optics, Vol.23, No.9 , 1368 (1984)

[57] T.O.Raubenheimer, private communication.

NOTES

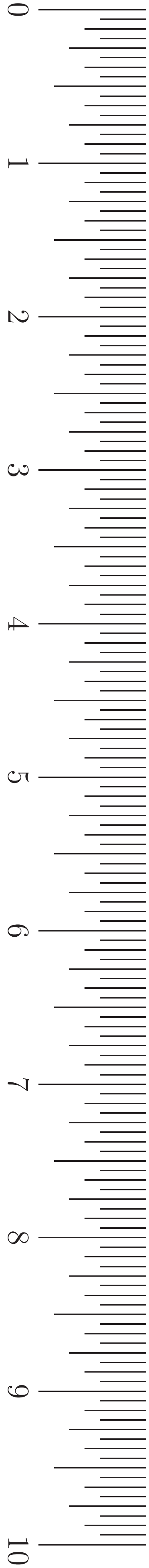

NOTES